

UNCONVENTIONAL RESERVOIR ENGINEERING PROJECT

PHASE I REPORT

Golden Colorado

November 13-14, 2014



Summary

This report presents the results of Phase 1 of the Unconventional Reservoir Engineering Project (UREP) Consortium, which was completed on Sept. 30, 2014. More information about UREP can be found on http://petroleum.mines.edu/research/urep/. Members can access this report, find additional details about the research projects, and download UREP publications under the "Members Only" tab of the UREP web page (if you do not have the password or need to receive a new password to access the Members Only section of the UREP web page, please contact us; eclayton@mines.edu, eclayton@mines.edu)

UREP Consortium was formed to focus on the unconventional aspects of unconventional reservoirs in October 2012. Its objective is to contribute to the long-term, sustainable production from unconventional reservoirs, including but not limited to nanoporous resource plays, such as shale-gas, tight-oil, liquids-rich formations, and tight carbonates.

Phase 1 of the consortium has been supported by 12 members: Baker Hughes, BHP Billiton, Cimarex Energy, ConocoPhillips, EOG Resources, Hess Corporation, Kappa Engineering, Noble Energy, Petrobras, Saudi Aramco, Shell, and Total. During Phase 1, we have enjoyed the sub-contractual support of our affiliates, Dr. R. Raghavan and NITEC, LLC (C. Ozgen, Dr. T. Firincioglu, B. Savage, C. Karacaer, and J. Hopkins). We have also started collaborating with Craft-Tech (Dr. A. Hosangadi, Dr. J. Busby, Dr. D. VanGilder, and Dr. J. L. Papp).

During Phase 1, two faculty members (Drs. E. Ozkan and X. Yin), one research associate (Dr. H. Sarak), one research administrator (Ms. E. Clayton), and 15 graduate students were involved in the project. One PhD and four MS students graduated from the UREP group over the past two years.

The funding for the first two years (Phase 1) of UREP was approximately \$1M. Of this budget, approximately 48% has been spent on sub-contracts, 23% on students, 13% on faculty and research associate, 1% on travel, and 5% on miscellaneous expenses. Indirect cost (overhead) paid to CSM is close to 10% of the total budget.

Phase 1 of the Consortium has already laid the foundation for nanoporous reservoir engineering and reached important milestones toward the development of new tools and practices. Phase 2 will continue, fundamentally, along the directions established during Phase 1. In addition to the theoretical and mathematical treatments started in Phase 1, emphasis will also be put on nanofluidics experiments in Phase 2.

Introduction

The focus of UREP is flow in tight unconventional oil and natural gas reservoirs. The general objective is to achieve a more complete reservoir engineering understanding and develop more appropriate reservoir engineering tools and practices for these reservoirs. This objective covers the entire spectrum of reservoir engineering research of nanoporous, nanodarcy-permeability, and microfractured unconventional-formations. Under scrutiny are the discerning physical characteristics, non-Darcy flow mechanisms, capillary- and surface-force effects in confinement, multi-phase flow in nanoporous media, and new fluid exchange mechanisms between fractures and the rock matrix. Development of reservoir models, analysis techniques, and prediction tools are also part of the research spectrum.

The research focus of UREP is divided into five project areas. Figures 1 and 2 show the project areas and the associated tasks and objectives. In this report, the results obtained in Phase 1 will be summarized and extensions into Phase 2 will be noted. Additional UREP reports, papers, presentations, and student theses and dissertations mentioned in this report can be found under the "Members Only" tab of the UREP web page: on http://petroleum.mines.edu/research/urep/.

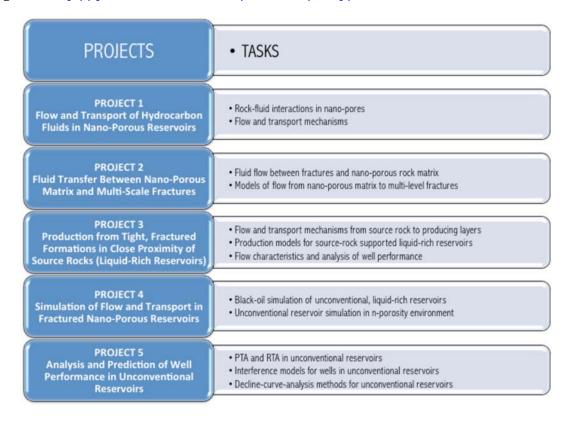


Figure 1 – UREP Projects and associated tasks

PROJECTS OBJECTIVES Develop a more comprehensive understanding and perception of **PROJECT 1** flow and transport in nano-porous reservoir rocks to form the basis Flow and Transport of Hydrocarbon of unconventional reservoir engineering tools and practices. Fluids in Nano-Porous Reservoirs Understand mechanisms associated with n-pore size environments Define the interface conditions and fluid transfer mechanisms **PROJECT 2** between nano-porous matrix and fractures to more realistically Fluid Transfer Between Nano-Porous Matrix and Multi-Scale Fractures account for the contribution of ultra-tight, unconventional rock **PROJECT 3** Define and model the support of source rocks on production from Production from Tight, Fractured Formations in Close Proximity of contiguous fractured formations for the analysis and prediction of production from liquids-rich reservoirs Source Rocks (Liquid-Rich Reservoirs) **PROJECT 4** · Progressively incorporate the results of the UREP research projects Simulation of Flow and Transport in Fractured Nano-Porous Reservoirs and new findings into a numerical unconventional-reservoir simulator developed by NITEC **PROJECT 5** · Develop and improve models and interpretation methods for **Analysis and Prediction of Well** pressure- and rate-transient data and long-term production Performance in Unconventional performance to help reservoir management Reservoirs

Figure 2 – Objectives of UREP projects

Technical Summaries

Technical summaries of the research undertaken during Phase 1 of UREP are provided below.

PROJECT 1: Flow and Transport of Hydrocarbons in Nano-Porous Reservoirs

Objectives: Develop a more comprehensive understanding and perception of flow and transport in nano-porous reservoir rocks to form the basis of unconventional reservoir engineering tools and practices. Understand mechanisms associated with n-pore size environments.

Tasks:

- Rock-fluid interactions in nano-pores (continuing into Phase 2)
- Flow and transport mechanisms (continuing into Phase 2)

Deliverables:

- Flow and transport mechanisms and constitutive relationships
 - Filtration through nanopore throats (Phase 1 results complete; more results in Phase 2)
 - Anomalous-diffusion models in tight, fractured, unconventional reservoirs (Phase 1 results complete; more results in Phase 2)
- Chemical equilibrium for black-oil hydrodynamic simulator
 - Bubble-point suppression due to pore proximity (Phase 1 results complete; experimental work continuing into Phase 2)
 - Condensation-point enhancement due to pore proximity (initial results being delivered; more theoretical and experimental results in Phase 2)
 - Phase behavior results from nanofluidics experiments (initial results being delivered; experimental work continuing into Phase 2)
- Principles of characterization and upscaling (partial results being delivered; work continuing into Phase 2)

Summary of Project 1 Results:

1.1. Bubble-point suppression due to pore proximity

The average pore size in unconventional, liquids-rich reservoirs is estimated to be less than 100 nm. At this nano-pore scale, capillary forces play an important role on phase behavior that is not considered in conventional PVT studies.

The difference between the gas and liquid pressure at equilibrium is given by

$$p_{gas} - p_{liquid} = p_c + \prod_s \tag{1}$$

where p_c is the capillary pressure and Π_s is the sum of the surface forces. Studies show that the magnitude of the bubble point suppression is more than the capillary pressure and may amount to hundreds of psi. In PVT cell experiments, capillary pressure and surface forces are negligible (because of the size of the cell, the curvature of the liquid-gas interface is large and the surface-fluid interactions are relatively negligible). As shown in Fig. 3, for negligible surface forces, if we consider the equality of chemical potentials at bubble point, the bubble-point pressure defined in a PVT cell is different from the bubble-point pressure in pore confinement by an amount defined by the capillary pressure and an excess suppression imposed by the size of the pore.

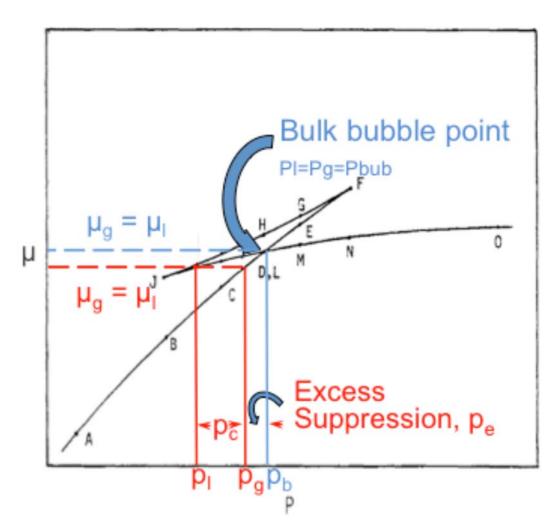


Figure 3 – Chemical potentials of liquid and gas as a function of pressure (Udell, 1982)

Effect of confinement on phase behavior of black-oil fluids manifests itself as bubble point pressure suppression (Fig. 4), extension of the undersaturated portion of the formation volume factor curve, and alteration of the equilibrium gas composition.

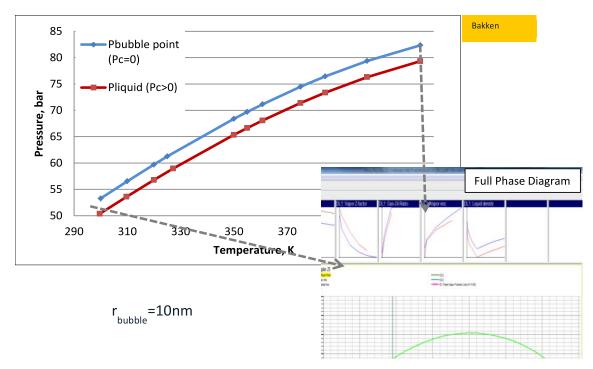


Figure 4 – Phase diagram shift due to pore confinement of a Bakken fluid sample

The bubble-point suppression phenomenon can be modeled through compositional solution of the phase behavior at differing gas- and oil-phase pressure values that are due to capillary pressure. However, the use of compositional simulators is not much desirable in unconventional reservoirs and black-oil simulators cannot perform the compositional phase behavior calculations to estimate the total bubble-point suppression due to confinement.

In this project, a correlation has been developed to expresses the bubble point pressure suppression as a function of the capillary pressure, p_c , and the solution gas oil ratio, R_s . As shown in Fig.3, the magnitude of the bubble-point suppression is equal to the sum of the capillary pressure for the given pore size and the excess suppression. The capillary pressure can be obtained from the pore size and surface tension information between the gas and liquid. In this study, the excess suppression amount has been correlated as a function of the solution gas-oil ratio as follows:

$$\frac{\text{Excess Suppression}}{\text{Total Suppression}} = -2.1 \times 10^{-7} R_s^2 + 9 \times 10^{-4} R_s - 1.022 \times 10^{-1}$$
(2)

Figure 5 shows the data used in the correlation and the quadratic function in Eq. 2 is the best fit to the data. Both p_c and R_s are the standard input parameters for black-oil simulators and are obtained through conventional PVT measurements.

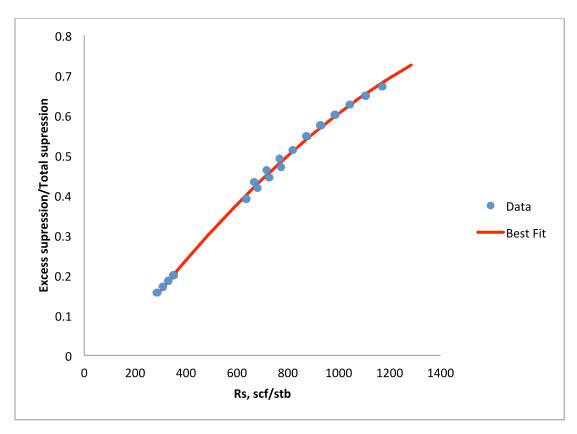


Figure 5 – Bubble-point suppression correlation

The correlation developed in this project enables us to incorporate bubble-point suppression effect into black-oil simulations of production from liquids-rich, tight formations. The correlation was developed based on the fluid samples from three liquids-rich, unconventional plays at different saturation pressures and compositions. To use the correlation, a modified black oil simulator, NITEC-COZSim-UREP, which can handle PVT data at different oil- and gas-phase pressures has also been developed. The source code of the black oil simulator used in this study was modified from the NITEC-COZSim-UREP simulator to include the total bubble-point suppression into the PVT calculations. The impact of the confined phase behavior on flow was quantified through simulation runs. Figure 6 shows example results of the NITEC-COZSim-UREP simulator indicating the effect of pore proximity on phase behavior.

The modified black-oil simulation results showed that;

The quality of the correlation was very good for the samples that the correlation
was based on. The normalization of the excess suppression using the total
suppression was necessary to handle the impact of capillary pressure difference
for each pore-radius due to different interfacial tension values at different
compositions and temperatures.

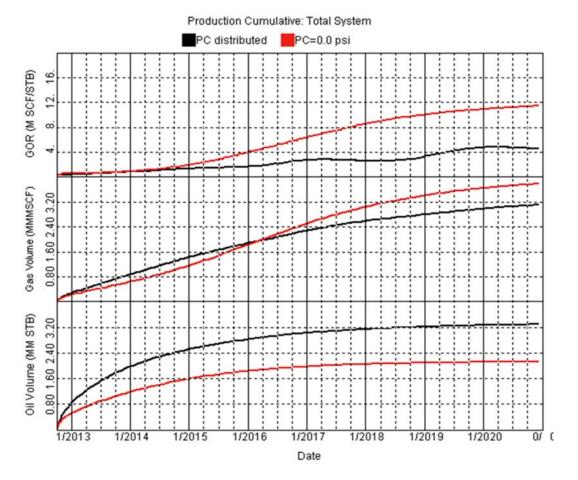


Figure 6 – Oil and gas production and GOR simulations from NITEC-COZSim-UREP simulator for negligible capillary pressure (P_C =0.0 psi) and an assumed capillary pressure distribution (P_C distributed)

- The gas saturation profiles in the reservoir and the GOR behavior of the wells differ from that of the conventional approach (no confinement impact on phase behavior) when confinement is included in the phase property calculations. The difference manifests itself as lower GOR values and later gas breakthrough for the wells and different gas saturation values for similar pressures in the reservoir.
- The confined fluid behavior has a positive impact on oil production for black-oil reservoirs. The improvement in oil production occurs due to later breakthrough of the gas and the extension of the undersaturated property range of the oil; both as a result of the bubble-point suppression.
- The impact on production can be more drastic when (normally) distributed gasoil capillary pressure values are assigned to represent the confinement in the reservoir. This impact manifests itself as gas saturation build up for some grid blocks with low gas-oil capillary pressure (lower bubble-point suppression) that are surrounded by zero gas saturation grid blocks (higher bubble-point

suppression). In some grid blocks, the gas comes out of the solution sooner than the surrounding grid blocks due to different suppression levels. Until the gas phase has a continuous path to the well location, it builds up in the grid block, yet cannot be produced. This behavior implies that it is not just the magnitude, but also the distribution of the bubble point suppression due to non-uniform capillary pressure (or pore size) distribution can influence the multi-phase flow.

The results of the research on bubble-point suppression in pore proximity have been presented in the following studies:

- Firincioglu, T., Ozkan, E., and Ozgen, C.: "Thermodynamics of Multiphase Flow in Unconventional Liquids-Rich Reservoirs," paper SPE 159869 to be presented at the SPE Annual Technical Conference and Exhibition held in San Antonio, Texas, USA, 8-10 October 2012.
- Firincioglu T., Ozgen C., Ozkan E.: "An Excess-Bubble-Point-Suppression Correlation for Black Oil Simulation of Nano-Porous Unconventional Oil Reservoirs ", paper SPE 166459 presented at the SPE Annual Technical Conference and Exhibition held in New Orleans, Louisiana, USA, 30 September-2 October 2013.
- Firincioglu T.: "Bubble Point Suppression in Unconventional Liquids Rich Reservoirs and Its Impact on Oil Production" PhD Dissertation, Petroleum Engineering Department, Colorado School of Mines, 2013.

1.2. Condensation-point enhancement in pore proximity

The objective of this project is to extend the research on bubble-point pressure suppression to condensation-point enhancement to complete the study of phase behavior in pore proximity. Because of our improved experimental capabilities, this research combines the experimental results with analytical simulations. The experimental studies are intended to improve EOS relations used in reservoir simulations by adding the effect of confinement. Analytical studies incorporate corrections to EOS relations by including the effects of capillary pressure and surface forces.

Experimental Study: Two sets of experiments are planned. The first set includes pressurizing and depressurizing propane gas inside a nano-fluidic chip at room temperature and recording the pressure as a function of volume. Comparison of the pressure change as a function of volume recorded during the experiments with different nano-fluidic chip sizes to that from bulk (PVT cell) data will provide information about the effect of pore proximity on pressure versus volume behavior. In the second set of experiments, effect of temperature is also taken into consideration; that is, the first set of experiments is repeated at different temperatures each time. Currently, experimental study is at the stage of testing and calibrating. The results will be reported during the second phase of the consortium research.

The nano-fluidic chips used in the experiments (Fig. 7) are made of silica plates bonded to glass in a series of fabrication steps.

- 1- Either parallel or random patterns of nano-channels are etched onto a mask with electron beam lithography.
- 2- Nano-channels on a mask are transferred onto a silicon wafer with a reactive ion etch.
- 3- The micro-channels are patterned into the silicon wafer and etched to contact the endpoints of nano-channel array and create large area to interface with the outside world.
- 4- Through-holes are made in the silicon wafer at the endpoints of micro-channels for inlet and outlet ports.
- 5- Finally the silicon wafer is oxidized and is bonded to a thin borosilicate glass wafer via anodic bonding.

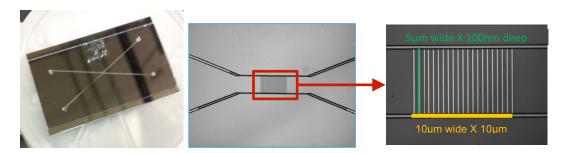


Figure 7 – Nano-fluidic chips used in the experiments

During the experiments, the nano-fluidic chip is connected to a hand pump via series of micro and macro tubes (Fig. 8). Hand pump is also connected to the propane tank (99.99% purity). A pressure gauge on the pump shows the pressure and the 500-nm filter removes the contaminants if any.

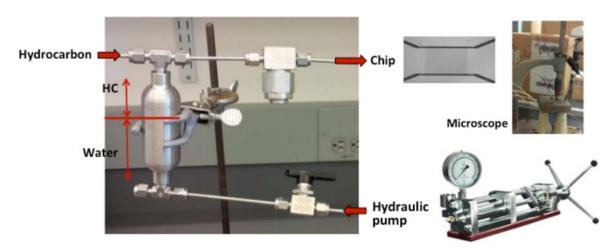


Figure 8 – Pump and nano-fluidic chip connections

The experimental setup has the ability to inject the gas through either one or two inlets of nano-chip. In order to make a closed system and pressurize the gas, the outlet ports should be closed. Turning the pump hands clockwise volume decreases and pressure rises. Counter clockwise turning of the pump hand results in pressure reduction and gas expansion.

After condensing the propane inside the chip all inlet/outlet ports open to atmosphere but because of high capillary pressure inside the chip the condensation does not vaporize and remains in the chip. This causes problems in the cleanup and reuse of the chips for the subsequent experiments. One option to remove the condensate is to heat the chip to high temperatures for extended periods. Another option is to blow out the condensate in the chip by injecting a high-pressure gas (such as air, CO2, N2, etc.); but this also takes a long time.

Analytical Study: For the analytical study of the effect of pore proximity on condensation pressure, flash calculations are performed by the Peng-Robinson (PR) EOS. The PR EOS is a cubic relation because the compressibility factor, Z, is a solution of the following cubic equation for a multicomponent mixture

$$Z^{3} - (1 - B)Z^{2} + (A - 2B - 3B^{2}) - (AB - B^{2} - B^{3}) = 0$$
(3)

where

$$Z = \frac{Vp}{RT} \tag{4}$$

$$A = \frac{ap}{R^2 T^2} \tag{5}$$

and

$$B = \frac{bp}{RT} \tag{6}$$

In Eqs. 4 through 6, V is the molar volume, R is the universal gas constant, and T is the temperature. The terms a and b In Eqs. 5 and 6 are given by

$$a = \sum_{i} \sum_{j} x_{i} \cdot x_{j} (1 - k_{ij}) \left(a_{i} a_{j} \right)^{0.5}$$
(7)

and

$$b = \sum_{i} x_i b_i \,. \tag{8}$$

where

$$a_{i} = 0.45724 \left(\frac{R^{2} T_{ri}^{2}}{p_{ri}} \right) \alpha_{i}$$
 (9)

and

$$b_i = 0.07780 \left(\frac{RT_{ri}}{p_{ri}} \right) \tag{10}$$

In Eqs. 9 and 10,

$$\alpha_{i} = \left[1 + m_{i}(1 - T_{r}^{0.5})\right]^{2} \tag{11}$$

$$m_{i} = \begin{cases} 0.37464 + 1.54226\omega_{i} - 0.26992\omega_{i}^{2} & \omega_{i} < 0.5215\\ 0.3796 + 1.48\omega_{i} - 0.1644\omega_{i}^{2} + 0.01666\omega_{i}^{3} & \text{Otherwise} \end{cases}$$
(12)

 ω_i is the acentric factor, and T_{ri} and p_{ri} are the reduced temperature and pressure, respectively.

In the above formulation, we use the mixing and combining rules. The vapor and liquid mole fractions, x_i and y_i , are related by

$$y_i = K_i x_i \tag{13}$$

where K_i is the equilibrium constant. At equilibrium, we can show that

$$\frac{\mu_i^o}{\mu_i^g} = K_i \frac{p_g}{p_o} \tag{14}$$

where μ_i^o and μ_i^g are the chemical potentials of the component i in the oil and vapor phases, respectively. Neglecting surface forces, the pressures of the gas and oil phases differ by an amount equal to the capillary pressure, p_c :

$$p_g - p_o = p_c \tag{15}$$

If capillary pressure is not negligible, then from Eqs. 14 and 15, we have

$$K_{i} = \frac{\mu_{i}^{o}}{\mu_{i}^{g}} \frac{p_{o}}{p_{o}} = \frac{\mu_{i}^{o}}{\mu_{i}^{g}} \left(\frac{p_{o}}{p_{o} + p_{c}} \right)$$
 (16)

To incorporate the effect of pore proximity into the PR EOS, we also need to account for the shift in the critical properties due to pore proximity by the following relations (Zarragoicoechea & Kuz, 2004):

$$\frac{T_{cb} - T_{cp}}{T_{cb}} = 0.9409 \frac{\gamma}{r_p} - 0.2415 \left(\frac{\gamma}{r_p}\right)^2 \tag{17}$$

and

$$\frac{P_{cb} - P_{cp}}{P_{cb}} = 0.9409 \frac{\gamma}{r_p} - 0.2415 \left(\frac{\gamma}{r_p}\right)^2$$
 (18)

where

$$\gamma = 0.244 \left(\frac{T_{cb}}{P_{cb}}\right)^{1/3} \tag{19}$$

 r_p is the pore radius, γ is the Lennard-Jones size parameter, and the subscripts, cb and cp stand for bulk and pore critical properties, respectively.

A flash calculation algorithm is being constructed and tested for the formulation of the PR EOS as described above. The results of this study will be available during Phase 2 of the consortium.

1.3 Experimental study of phase behavior in nanofluidics and modeling of the effect of pore size distribution

Petrophysical studies have confirmed that pore sizes of many shale and tight oil and gas reservoirs are in the range of nanometers. In these pores, the phase behavior of hydrocarbon mixture, affected by the capillary pressure and the surface forces, are different from that characterized in PVT cells. Many existing phase behavior models use a single pore size. This research investigates the effect of a pore size distribution on the vapor-liquid equilibrium of alkane mixtures by experiments and modeling. In this report, we elaborate on the experimental findings and the implications, as has been presented in SPE 169581. Modeling of depressurization of fluids confined in pores with discretized pore size distribution, presented in SPE 170894, is briefly captured by only mentioning the main conclusions.

In the experiments, we used a nanofluidic device to visualize phase transitions of pure alkane and an alkane mixture due to evaporation. As shown in Figure 7, the nanofluidic device consists of two parallel microchannels perpendicularly connected by twenty-one nanochannels. The dimensions of the micro- and nanochannels are 10 μm wide by 10 μm deep and 5 μm wide by 100 nm deep, respectively. The volume of the microchannels to that of the nanochannels is approximately 38:1, i.e. the volume fraction of the nanochannels in the entire pore volume is 2.56%.

The fluids tested include pure n-pentane and a ternary hydrocarbon mixture consisting of 4.5 mol% n-butane, 15.5 mol% iso-butane and 80.0 mol% n-octane. The composition of the ternary hydrocarbon mixture is chosen from the phase envelope in Figure 9, as denoted by the black circle below the two-phase region between the cross markers. At the atmospheric pressure (here, it is taken as 8.5×10^4 Pa or 12.4 psia due to the elevation of the city of Golden, Colorado) and below 298 °K (76.7 °F) it should be stable in the liquid form. But both liquids are very close to their respective boiling and bubble points; they are therefore highly volatile.

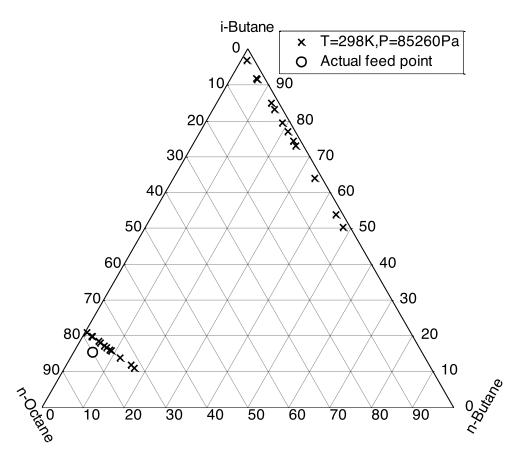


Figure 9 – Ternary diagram of hydrocarbon mixture in microchannels at 298 °K (76.7°F).

As the experimental temperature rises to 345 °K (161 °F), the liquid mixture in the microchannels should flash into two phases while that in the nanochannels should remain to be a liquid because of the shifted bubble and dew point lines due to the capillary pressure. The ternary diagram of the mixture at 345 °K and the feed point are shown in Figure 10, in which the region contained by the asterisk markers is the two-phase zone for the mixture in the nanochannels. The area between the triangular markers is the two-phase region for the ternary mixture confined by the microchannels, which is very close to the phase envelope of the mixture in a PVT cell. The method used to predict the effect of confinement on the phase envelopes, which follows that by Brusilovsky (1992) and Shapiro and Stenby (2001) and is identical to that in Firincioglu et al. (2012, 2013), is not presented here for brevity.

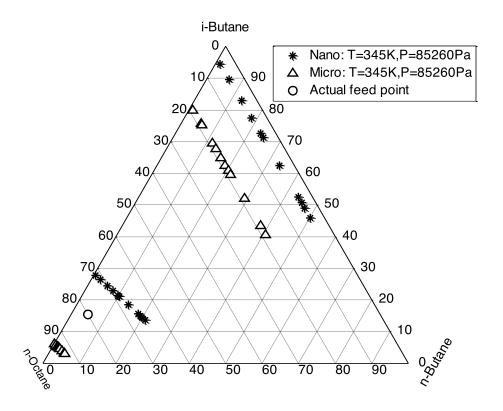


Figure 10 – Ternary diagram of hydrocarbon mixture in micro- and nanochannels at 345 °K (161°F).

A lighter was used as a container to prepare the ternary mixture with desired composition. Air was firstly displaced out of the lighter chamber by butane vapor that has a fixed mole ratio (0.29:1; n-butane vs. i-butane). Then, liquid octane was transferred into the lighter and the weight difference was measured. Finally, butane vapor was injected into the lighter chamber to achieve the target molar composition of the ternary mixture.

At the atmospheric pressure in Golden, Colorado, and controlled temperature of 298 °K (76.7 °F), hydrocarbon liquids were loaded into the interconnected networks from the ports attached to the ends of the microchannels. By gradually heating up the system using a light bulb, vapor-liquid interfaces moved as hydrocarbon evaporated and left the channels. The phenomena were directly observed through an optical microscope and captured by a digital camera connected to the microscope. A thermalcouple was attached to the surface of the nanofluidic device to record the temperature.

Figure 11 shows the consecutive images taken with a time-lapse interval of 0.05 second for the evaporation of pure n-pentane (boiling point is 309 °K) at the atmospheric pressure and 298 °K. Note that as this temperature is below the boiling point, vaporization was driven by the evaporation of the n-pentane through the open ports of the microchannels. Since the liquid n-pentane is a wetting fluid relative to its vapor with respect to the surface of the device, as expected from the Kelvin's equation, evaporation first took place in the microchannels. The interfaces did not progress into the nano-

channels until the evaporation in the micro-channels was complete. This shows that the nanoconfinement in the device compared to the dimension of the microchannels (100 nm vs. 10 μ m) generated a distinguishable contrast in capillarity that determined the sequence of evaporation. Additionally, the evaporation of n-pentane was very rapid, which indicates that the mass transfer resistance to evaporation was very small.

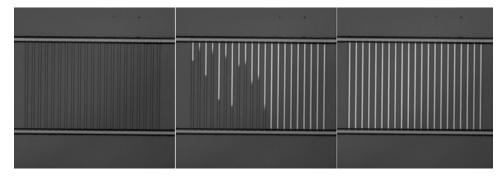


Figure 11 – Three consecutive images taken during the evaporation of pure n-pentane in the nanofluidic device. Left: n-pentane in two microchannels is evaporated, leaving the nanochannels filled with liquid; Middle: n-pentane in some of the nanochannels evaporated; Right: n-pentane in both micro- and nanochannels totally evaporated.

The vaporization of the ternary hydrocarbon mixture, as shown in Figure 12, is very different. Although the liquid started to vaporize in the microchannels first, as expected because the liquid therein crosses the bubble point line first with increasing temperature, the progression of the meniscus slowed down considerably with time and could not progress into the nanochannels at 345 °K (161°F), a temperature much higher than the bubble point temperature of the initial mixture. Instead, the meniscus stopped at a location shown in Figure 12. The reason is that the liberation of lighter components from the liquid phase to the gas phase in the microchannels increases the apparent molecular weight of the remaining liquid as well as its bubble point.



Figure 12 – Three images taken during the vaporization of the ternary mixture in the chip. Left: Micro- and nanochannels filled with air; Middle: Micro- and nanochannels filled with the ternary hydrocarbon mixture; Right: Vaporization of the ternary mixture stopped in one of the microchannels at 345 °K.

A Peng-Robinson equation of state (Peng and Robinson 1976) based flash calculation procedure that accommodates the capillary pressure was previously developed by Brusilovsky (1992) and Shapiro and Stenby (2001). It is implemented here to model the nanoconfinement effect on the hydrocarbon phase behavior. The pressures of the gas and the liquid phases are differentiated by the capillary pressure, which is calculated using the sizes of pores (micro- and nanochannels), an assumed contact angle θ = 30°, and an interfacial tension (IFT) σ that is estimated with the parachor correlation (Weinaug and Katz, 1943). The critical properties, acentric factors, and binary interaction parameters are presented in Table 1.

Table 1 – Critical properties, acentric factors and binary interaction parameters.

Paramete	ers	iso-butane	n-butane	n-octane
T _c (°K)		408	425	569
P _c (MPa)		3.65	3.80	2.49
ω_{i}		0.1770	0.2002	0.3996
iso-butane		0	0	0.026
δ_{ij}	n-butane	0	0	0.012
	n-octane	0.026	0.012	0

The classic flash calculation procedure, before taking into account the capillary pressure, was validated by calculating the PT phase envelope of a ternary mixture containing 40 mol% n-butane, 20 mol% n-petane and 40 mol% n-octane. Properties of the three components are listed in Table 2. Figure 13 is obtained with the Eclipse-PVTi module, and Figure 14 is the PT phase diagram calculated with the flash calculation procedure that we developed in the absence of the capillary pressure. It is clear that both the bubble point line and the dew pont line agree very well with Eclipse-PVTi in the entire temperature range, indicating satisfactory accuracy of our procedure. Additionally, note that the Eclipse-PVTi ran into severe fluctuations between 480 and 520 °K for the bubble point calculation, which is a common stability issue encountered in the vicinity of the critical point. On the contrary, our procedure achieved perfectly smooth transitions in this sensitive area, demonstrating excellent robustness and reliability.

Table 2 – Critical properties, acentric factors and binary interaction parameters.

Paramete	ers	n-butane	n-pentane	n-octane
T _c (°K)		425	470	569
P _c (MPa)		3.80	3.37	2.49
ω_{i}		0.2002	0.2515	0.3996
	iso-butane	0	0.017	0.012
δ_{ij} n-pentane		0.017	0	0
,	n-octane	0.012	0	0

As indicated by the ternary phase diagram in Figure 10, the liquid mixture in the microchannels should flash into two phases when the experimental temperature rises to 345 °K (161°F); however, the meniscus just stopped in front of the smaller microchannel and was not able to propagate into it with strong and sustained heating. Our hypothesis is that besides the larger nanoconfinement the smaller channel has on the hydrocarbon mixture, preferential vaporization of lighter components from the system increased the apparent molecular weight of the remaining fluid, consequently raising its bubble point temperature. To verify this hypothesis, the heating process of the ternary mixture is modeled as a constant-pressure, constant-composition expansion from the room temperature to the final experimental temperature of 345 °K (161°F), at the atmospheric pressure in Golden, Colorado. The data before and after the simulated expansion are listed in Table 3.

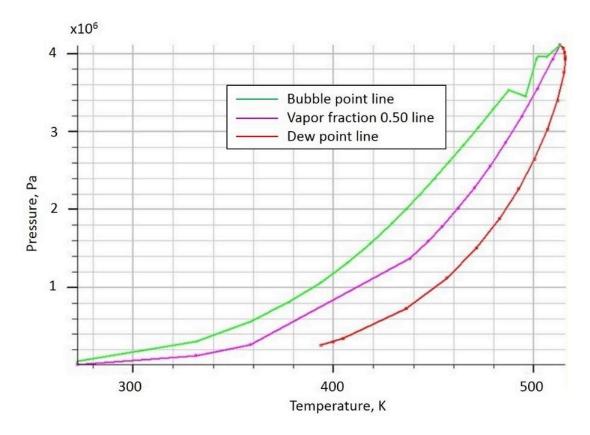


Figure 13 – Phase evelope of 40 mol% n-butane, 20 mol% n-petane and 40 mol% n-octane generated by Eclipse-PVTi.

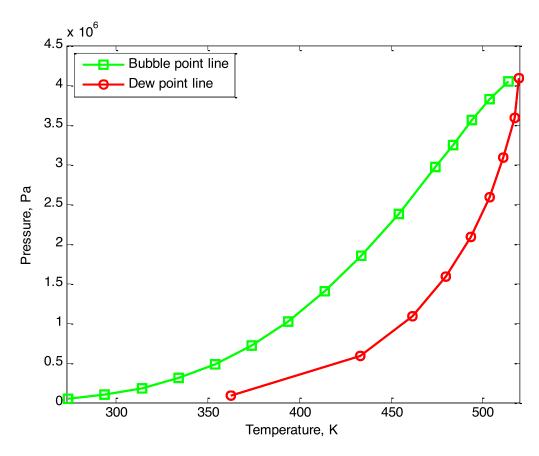


Figure 14 – Phase evelope of 40 mol% n-butane, 20 mol% n-petane and 40 mol% n-octane generated by our classic flash calculation procedure.

Table 3 – Simulation parameters before and after flash calculation at constant pressure.

Parameters	Before flash calculation		After flash calculation			
Temperature (°K)		298		345		
Pressure (Pa)		85260			85260	
Liquid (i C_4 -n C_4 - C_8 , mol%)	0.1547	0.0453	0.8000	0.0488	0.0187	0.9325
Vapor (iC ₄ -nC ₄ -C ₈ , mol%)	0	0	0	0.6435	0.1682	0.1883
Residual liquid (mol%)	100.00		82.20			
Residual liquid (vol%)	100.00		76.52			
IFT (mN/m)					16.24	
P _c in micro-channel (kPa)					3.38	
P _c in nano-channel (kPa)					286.91	
T _b in micro-channel (°K)		303.45			345.00	
T _b in nano-channel (°K)		363.28			404.00	

The vapor and liquid compositions after expansion demonstrates that the lighter components are preferentially released into the vapor phase, leaving a much heavier liquid phase with 93.2 mol% n-octane behind. Also for the feeding composition used in this experiment, the remaining liquid accounts for as high as 76.5 vol% after the flash calculation. Because the volume fraction of the nanochannels is only 2.56% of the total pore volume, the bulk of the micro- and nanochannels is still occupied by the liquid phase. This calculated volume fraction of remaining liquid is quantitatively consistent with the experimental observation that only one of four large microchannels was evaporated, leaving more than 75 vol% of the total volume of the micro- and nanochannel network saturated with liquid. Using the calculated IFT, the capillary pressure values are evaluated for the cases where a bubble is generated in the micro- or nanochannels. The capillary pressure that would act on a bubble generated in the nanochannel is nearly two orders of magnitude higher than that would act on a bubble generated in the micro-channel. This calculation explains the observations that for the ternary mixture, vapor bubble was also first formed in the microchannel.

These experiments were not conducted within an enclosed volume and with a fixed temperature; hence, strictly they cannot be directly compared with constant-composition phase equilibrium calculations. However, qualitative conclusions can still be drawn for phase change of hydrocarbon mixtures in porous media with pores of different sizes. On one hand, phase transition in porous media follows the sequence dictated by the pore sizes and the strength of capillarity. This is demonstrated by the sequence of vaporization of pure n-pentane in the nanofluidic chip. Another conclusion that is supported by modeling is that, for petroleum mixtures, preceding phase change alters the composition of the remaining fluids, and in turn, affects the point of the next phase transition. This is indicated by the slowing down of the propagation of the vaporliquid interface during the vaporization of the ternary mixture.

With these main conclusions, in SPE 170894, the modeling procedure was applied to a set of realistic pore size distribution data with assumed mixture compositions representing typical oil and condensate to predict the state of fluid phase and composition within the pore size distribution. The results showed that;

- For light oil, during depressurization, the foregoing vaporization increases the apparent molecular weight of the liquid residing in smaller pores and in turn suppresses the subsequent vaporization; in porous medium with a critical gas saturation, strong capillary pressure can delay the gas phase breakthrough.
- For retrograde gas, during depressurization, the foregoing condensation decreases the apparent molecular weight of the gas and in turn suppresses the subsequent condensation. Due to capillarity, condensation first forms in the smallest pores. However, due to the very small interfacial tension, whether capillary pressure is considered or not does not have a significant influence over phase transition and fluid properties.

As a result of the research on phase behavior results from nanofluidics experiments, the following studies are completed:

- Wang L., Gao Y. Neeves K. Ozkan E., Yin X.: "Experimental Study and Modeling of the Effect of Pore Size Distribution on Hydrocarbon Phase Behavior in Nanopores", paper SPE 170894 presented at the SPE Annual Technical Conference and Exhibition held in Amsterdam, The Netherlands, 27-29 October 2014.
- Wang L., Parsa E., Gao Y., Ok J.T., Neeves K., Yin X., Ozkan E.: "Experimental Study and Modeling of Nanoconfinement on Hydrocarbon Phase Behavior in Unconventional Reservoirs", paper SPE 169581 presented at the SPE Western North American and Rocky Mountain Joint Regional Meeting held in Denver, Colorado, USA, 16-18 April 2014.

1.4. Filtration in nanopore throats

In nanoporous media, Darcy flow is no longer the dominating flow mechanism and a combination of diffusive flows determines the flow characteristics. Concentration driven self-diffusion has been well known and included in the flow and transport models in porous media. However, when the sizes of the pores and pore-throats decrease down to the size of the hydrocarbon molecules, the porous medium acts like a semi-permeable membrane, and the size of the pore openings dictates the direction of transport between adjacent pores. Moreover, when multiple mechanisms contribute to flow, coupled fluxes need to be defined by the sum of all fluxes where the flux of type i is related to the gradient of type j through some phenomenological coefficients known as transport parameters.

The size comparison of the hydrocarbon molecules and the pore throats of shales shown in Fig. 15 indicates that light hydrocarbons, such as methane, may flow freely in shale while heavier hydrocarbons, such as some paraffins, ring structures, and asphaltenes, may likely be sieved out. This observation is consistent with the fact that most shale-gas plays produce higher than 95% methane and only light oil can be produced from ultra-tight, unconventional reservoirs. Thus, it can be inferred that the remaining composition of the fluids in the reservoir includes more of the heavier components than that produced at the surface. The fact that nanoporous media acts like a semipermeable (non-ideal) membrane and causes steric hindrance (filtration) to the flow of some (larger) hydrocarbon components has ramifications on future performance predictions and the planning of EOR applications in tight unconventional reservoirs. Therefore, understanding and quantifying the ability of the nanoporous media to act as a semipermeable (non-ideal) membrane and developing formulations to incorporate steric hindrance (or filtration) in flow models is essential.

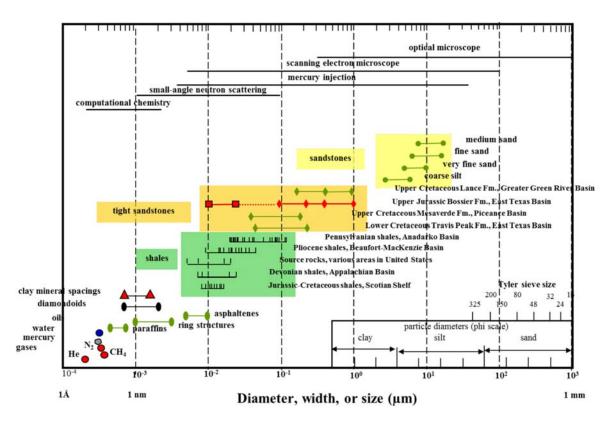


Figure 15 – Sizes of molecules and pore throats in siliciclastic rocks on a logarithmic scale covering seven orders of magnitude (Nelson, 2009)

The concept of steric hindrance (or filtration) is closely related to osmosis. Osmosis is a special type of diffusion where osmotic pressure is created by the chemical gradient of solutions across a semi-permeable membrane, which allows water molecules but not solution ions. Water molecules flow from low-salinity to high-salinity solutions, due to the difference in water activity, until it reaches equilibrium (Fig. 16a). At equilibrium, the increase in hydrostatic pressure equals the theoretical osmotic pressure (Fig. 16b).

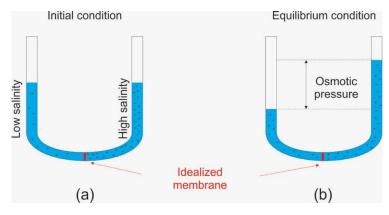


Figure 16 – Osmotic pressure in a U-tube initially containing low- and high-salinity water separated by an idealized, semi-permeable membrane.

The ability of a material to act as an osmotic membrane is quantitatively characterized by the osmotic or membrane efficiency, ω , which is called filtration efficiency in this research. Its value ranges between 0, for impermeable materials, and 1, for materials with perfect or ideal membrane behavior. Between the two extremes $(0 < \omega < 1)$, membranes are called nonideal. Both nonideal and ideal membranes are semi-permeable. The membrane efficiency of a soil depends on the effective size of the pores, and the size of the free-solution channels. Because of the variations of the pore sizes in soils, only a portion of the pores display membrane properties $(0 < \omega < 1)$, and, therefore, soils are usually nonideal or leaky membranes. In general, ω increases with the effective stress and decreases with the solute charge and/or solute concentration.

Shale is considered as a membrane according to two basic theories:

- Electrostatic exclusion for charged solutes (Fig. 17)
 - *i.* In an ideal membrane (i.e., $\omega = 1$), electric fields associated with the diffuse double layers (DDLs) of adjacent clay particles overlap within the pore space. Ions attempting to pass through the membrane are repelled across the entire width of the pore space.
 - *ii.* Conversely, pore spaces of a non-ideal membrane (i.e., $0 < \omega < 1$) are sufficiently large that the electric fields do not overlap and contain an area of neutral or "free" solution through which ions can pass.

- Steric hindrance

- i. Geometric restriction to flow occurs when the size of the solute exceeds the pore size.
- *ii.* Unlike electrostatic restriction, this is the exclusion of uncharged solutes (e.g., nonpolar organic solutes), particularly those with high molecular weight.

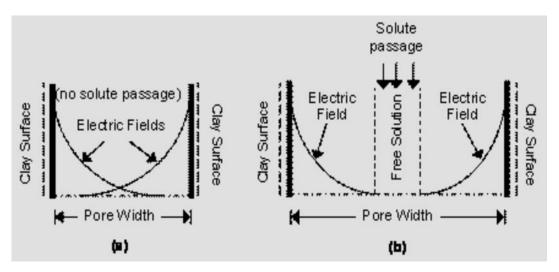


Figure 17 – Electrostatic exclusion of charged solutes: (a) "ideal" membrane: (b) "non-ideal" membrane. (Clay Membrane Barriers, 2013).

Because the hydrocarbons of interest in this study are uncharged, steric hindrance (geometric restriction) is the source of the membrane property, which leads to the filtration (sieving) of hydrocarbon molecules according to their sizes in nanoporous media. The magnitude of filtration is a function of the filtration pressure.

To define filtration and filtration pressure in unconventional, tight-oil reservoirs, we consider two systems, which are connected with a pore throat possessing membrane properties (Fig. 18). Because the pore throat selectivity permits the passage of fluid molecules by their sizes, given a filtration pressure difference between two systems, the concentration difference between the systems is determined by flash calculations. The results are expressed in the form of filtration efficiency, which is essential parameter to define coupled fluxes for porous media flow.

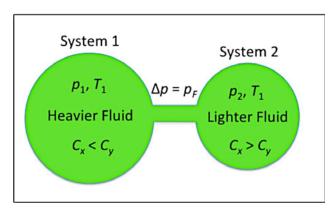


Figure 18 – Two-pore system used to model filtration by a nano-pore throat.

As shown in Fig. 18, we assign different molar fractions C_x and C_y to the light and heavy hydrocarbon components, respectively, in the two pores to create a heavier hydrocarbon mixture on one side (System 1) and a lighter mixture on the other side (System 2). First, performing flash calculations by Peng-Robinson Equation of State (PR EOS) at a pressure p_1 and a temperature T_1 , and ensuring that the system components stay in liquid phase for all times, we compute the fugacities of the components in System 1. Then, we assume a filtration pressure, $p_F = \Delta p = p_1 - p_2$, between the two systems, such that the pressure of System 2 is $p_2 = p_1 - p_F$. At thermodynamic equilibrium, the fugacity of the light component, C_x , should be the same in both systems; that is,

$$f_{C_x}^{L_1} = \Phi_{C_x}^L x_{C_x} P_1 = f_{C_x}^{L_2} = \Phi_{C_x}^L x_{C_x} P_2$$
 (20)

However, the filtration (steric hindrance) of the heavy hydrocarbon component, C_y , would create imbalance in the fugacity of the heavy component:

$$f_{C_y}^{L_1} \neq f_{C_y}^{L_2} \tag{21}$$

Knowing the fugacity of Component x, the molar compositions, C_x and C_y , in System 2 at pressure p_2 can be obtained from flash calculations and the composition difference between the two systems under a filtration pressure p_F can be predicted. (Conversely, this procedure could be applied by initializing the two systems at different compositions and then estimating the filtration pressure required to maintain this composition difference.)

After the fugacities of the components in Systems 1 and 2 are determined, the filtration efficiency of the nano-porous medium is determined from

$$\omega_f = 1 - (f_{C_v}^{L_2} / f_{C_v}^{L_1}) \tag{22}$$

The overall procedure used to compute the filtration (membrane) efficiency is summarized in the flow chart given in Fig. 19.

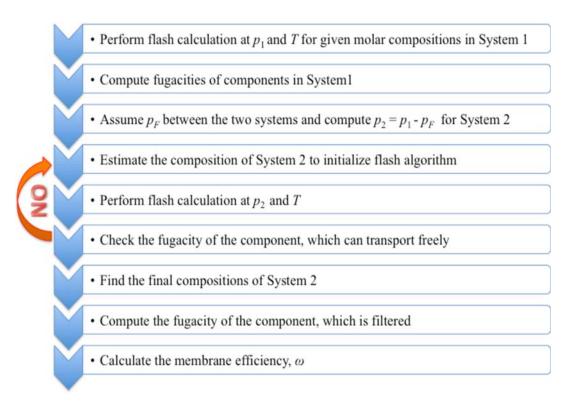


Figure 19 – Calculation of the membrane efficiency of a nanoporous medium

In the example cases studies in this research, C_1 , NC_4 , C_8 , C_{10} , C_{12} , C_{16} and C_{26+} have been used as the components of the fluids in Systems 1 and 2 in Fig. 18. In each case, the components were classified as hindered (filtered) and unhindered (unfiltered) and grouped accordingly. Calculations were performed for three different groupings of the components:

- Case 1.Two-component, sequential grouping: One unhindered (small) component and multiple hindered (large) components, each of which is grouped with the small component sequentially,
- Case 2.Multi-component grouping: Multiple unhindered (small) components grouped as one and paired with one hindered (large) component
- Case 3.Pseudo component grouping: Two pseudo component groups of unhindered, small and medium components and one pseudo component group of hindered large components.

For demonstration, only some results for two-component, sequential grouping (Case 1) will be summarized here. In this case, Systems 1 and 2 include only two component fluids. While C_1 is the unhindered (small) component, one of NC_4 , C_8 , C_{12} , C_{16} and C_{26+} , at a time, is selected as the hindered (large) component and the computations are performed sequentially. Physical properties of these components, which were used in flash algorithm, are given in Table 4.

Table 4 – Peng-Robinson characterization for the components

A. Critical Constants

СРТ	Pc (psi)	Tc (R)	Acentric Factor (ω)	MW (g/mole)	Zc
C_1	667.0029	343.00026	0.1100	16.043	0.287600000
NC_4	550.6018	765.20070	0.2000	58.124	0.272800000
C ₈	421.4019	1043.40078	0.3105	108.89	0.264117010
C_{10}	360.3018	1138.00086	0.3913	134.96	0.259671059
C_{12}	314.0006	1214.90100	0.4700	160.55	0.254505703
C_{16}	249.9011	1335.50100	0.6197	210.51	0.249740073
C ₂₆₊	140.8009	1631.40138	1.1619	412.23	0.227877773

B. Binary Interaction Parameters between C₁ and other components

	C_1	NC ₄	C ₈	C ₁₂	C ₁₆	C ₂₆₊
C_1	0	0.014749	0.033997	0.054287	0.071547	0.113281

C. Composition (Mole Fraction) of System 1

C ₁	NC ₄	C ₈	C ₁₂	C ₁₆	C ₂₆₊
0.3	0.7	0.7	0.7	0.7	0.7

The pressure and temperature of System 1 is 10,000 psi and 660° R (200° F), respectively. Filtration pressures of 500-, 2,000-, 4,000- and 5,000-psi are considered and the molar compositions at equilibrium conditions were calculated for System 2. The mole percentages of the hindered and unhindered components are 70% and 30%, respectively. Component C_1 was the small component (solvent) and NC₄, C_8 , C_{12} , C_{16} and C_{26+} , one by one, were chosen as the big component (solute). Consequently, molar compositions of components at equilibrium conditions were calculated for System 2.

Figures 20 and 21 show the results for the systems with $C_1\&NC_4$ and $C1\&C_{26+}$ respectively. They depict that for all filtration pressures, System 2 has more C_1 and less NC_4 or C_{26+} than System 1. Moreover, the higher the filtration pressure (that is, the smaller the pore-throat size), the more the concentration difference between Systems 1 and 2. Higher filtration pressure results in lower composition for the larger component, implying that larger component is hindered more when the pore throat size is smaller.

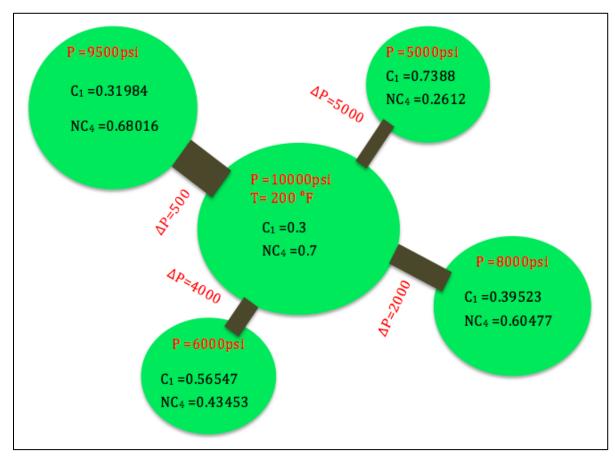


Figure 20 – Filtration of C_1 &NC₄ (molar compositions of 0.3&0.7) for different filtration pressures (Δp)

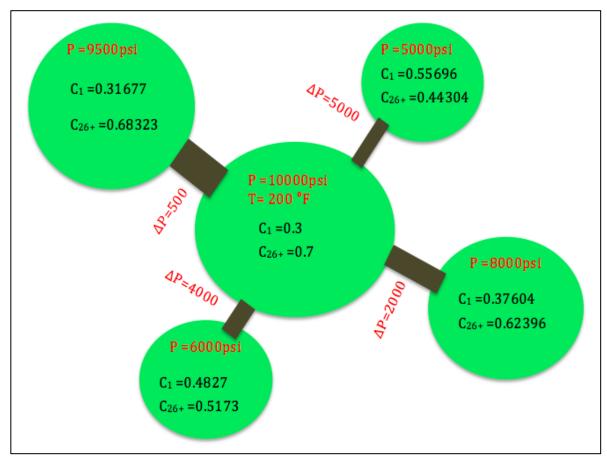


Figure 21 –Filtration of $C_1\&C_{26+}$ (molar compositions of 0.3&0.7) for different filtration pressures (Δp)

The same procedure has been applied for the other pairs of unhindered and hindered components ($C_1\&C_8$, $C_1\&C_{12}$, and $C_1\&C_{16}$) and the resulting compositions of System 2 as a function of filtration pressures are shown in Figure 22. If the results for $C_1\&NC_4$ and $C_1\&C_{26+}$ are compared, different filtration pressures will be required to attain the same concentration difference between $C_1\&NC_4$ and $C_1\&C_{26+}$. For example, the same molar concentrations of 0.5&0.5 in System 2 are attained at 3,400-psi and 4,300-psi filtration pressures, respectively, for $C_1\&NC_4$ and $C_1\&C_{26+}$ (i.e., larger components cause higher filtration pressures).

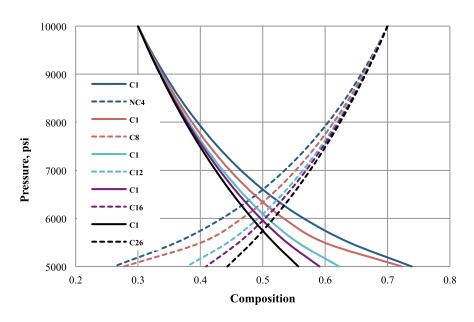


Figure 22 –Compositions of System 2 for $C_1\&NC_4$, $C_1\&C_8$, $C_1\&C_{12}$, $C_1\&C_{16}$ and $C_1\&C_{26+}$ for different filtration pressures (Δp)

After the concentration differences were obtained at different filtration pressures, the fugacity of the filtered component may be computed and the membrane efficiency, ω_f , can be calculated. Figure 23 shows the membrane efficiencies, ω_f , for NC₄, C₈, C₁₂, C₁₆ and C₂₆₊ for different filtration pressures, Δp . As expected, when the filtered component becomes larger, the membrane efficiency increases.

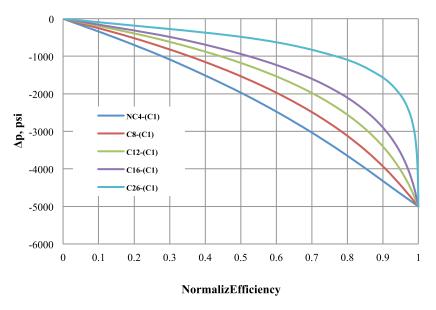


Figure 23 – Membrane efficiencies (ω_f) for C₁&NC₄, C₁&C₈, C₁&C₁₂, C₁&C₁₆ and C₁&C₂₆₊ for different filtration pressures (Δp)

When the filtration efficiency is known, coupled fluxes to be used in a macroscopic model of coupled-flow phenomena in shale may be constructed. The flux equations are the relations between the flows and the driving forces. Coupled fluxes under isothermal conditions are defined by a dissipation function, which is a sum of all fluxes where the flux of type i is related to the gradient of type j through some phenomenological coefficients known as transport parameters (Table 5). If only one type of flow is dominant, then the transport parameters may be determined fairly easily from experiments or a microscopic theory of transport, as in the estimation of permeability from Darcy's law. For coupled flows, the interdependency of transport parameters complicates or prohibits their estimation.

Table 5 – Co	upled and D	irect Flow F	'henomena (Young & Mit	tchell, 1993)

Flow J		Gradient X				
	Hydraulic	Electrical	Chemical	Thermal		
Fluid	Hydraulic conduction (Darcy's Law)	Electro-osmosis	Normal osmosis	Thermal osmosis		
Electric Current	Streaming potential	Electric conduction	Diffusion and membrane potentials	Seebeck effect		
Ion	Streaming current	Electrophoresis	Diffusion (Fick's Law)	Soret effect		
Heat	Isothermal heat transfer	Peltier effect	Dufour effect	Thermal conduction		

Coupled fluxes under isothermal conditions are defined by a dissipation function, Φ , given by

$$\Phi = \sum_{i=1}^{N} \vec{J}_i X_i \tag{23}$$

where

$$\vec{J}_{i} = \sum_{j=1}^{n} L_{ij} \vec{X}_{j} \tag{24}$$

In Eq. 24, L_{ij} are the phenomenological coefficients that relate the flux of type i to the gradient of type j. Assuming isothermal reservoir conditions and focusing only on flows that are caused by chemical gradient, the dissipation function, Φ , for coupled flows due to hydraulic, electrical, and chemical gradients is given by

$$\Phi = -q \frac{\partial p}{\partial x} - \sum_{i=1}^{M} J_i^d \frac{\partial \mu_i}{\partial x}$$
 (25)

where M is the number of solute species, p and μ_i are the liquid pressure and the chemical potential of solute i, respectively. In Eq. 25, the liquid (solution) flux, q, and the molar diffusive flux, J_i^d , of solute i are given, respectively, by

$$q = -L_{11} \frac{\partial p}{\partial x} - \sum_{i=1}^{M} L_{1,j+2} \frac{\partial \mu_i}{\partial x}$$
 (26)

$$I = -L_{21} \frac{\partial p}{\partial x} - \sum_{i=1}^{M} L_{2,j+2} \frac{\partial \mu_i}{\partial x}$$
 (27)

and

$$J_{i}^{d} = -L_{j+2,1} \frac{\partial p}{\partial x} - \sum_{i=1}^{M} L_{j+2,j+2} \frac{\partial \mu_{i}}{\partial x} \quad j = 1, 2, ..., M$$
 (28)

If the chemical solution is dilute such that ideal solution relationship is valid, we also have

$$\frac{\partial \mu_i}{\partial x} = \frac{RT}{C_i} \frac{\partial C_i}{\partial x} \tag{29}$$

The coupled fluxes concept may be applied for filtration in nanoporous media by considering a single-solute system (M = 1 and for dilute solutions $V_w \approx 1$). In this case, we have

$$q = -\frac{k}{\mu} \frac{\partial p}{\partial x} + \frac{\omega_f k}{\mu} RT \frac{\partial C_s}{\partial x}$$
 (30)

and

$$J_{s}^{d} = \frac{\omega_{f} C_{s} k}{\mu} \frac{\partial p}{\partial x} - \left(\frac{\phi D_{s}^{*}}{RT} + \frac{\omega_{f}^{2} C_{s} k}{\mu}\right) RT \frac{\partial C_{s}}{\partial x}$$
(31)

where the subscript s stands for the solute and, for our purposes, refers to the hydrocarbon component that is sterically hindered by the pore-throat size. In Eq. 31, D_s^* is the effective self-diffusion coefficient for sterically hindered hydrocarbon component, which accounts for the factors affecting self-diffusion in pore channels and is related to the self-diffusion coefficient, D_s , by

$$D_s^* = \tau_a D_s \tag{32}$$

In Eq. 32, τ_a is a dimensionless apparent tortuosity factor ($0 \le \tau_a \le 1$) that accounts for the tortuosity and connectivity of the pore channels as well as any other factor affecting self-diffusion.

In this interpretation, smaller molecular size hydrocarbons, which are permitted to pass through the pore throats, are treated as the solvent. Except for the membrane efficiency, $\omega_{\it f}$, of the nanoporous medium, all of the parameters involved in this formulation are conventionally determined. The membrane efficiency, $\omega_{\it f}$, of the nanoporous medium is obtained by the method developed in this research. It must also

be noted that, the results of the research not shown here have indicated that the membrane properties of nanoporous media also affect the fluid phase behavior.

In general, the results of the research summarized here indicated that

- For two component systems, the filtration effect increases much faster with the increasing molecular size than increasing concentration. In other words, the filtration effect increases as the molecular size increases and reaches a limit where most molecules are hindered by the pore size. At this limit, filtration effect becomes less sensitive to concentrations.
- There is practically no difference between the membrane efficiencies of the twocomponent and multicomponent systems. This result can be explained by the fact that the hindered component properties are the same for the compared cases; in other words, the membrane efficiency is mostly governed by the properties of the hindered component.
- Similar results are obtained for the pseudo component grouping systems.
- Difference in fluid compositions within different nanoporous systems can affect bubble point pressure and formation volume factor of oil.

As a result of the research on filtration in nanopore throats, the following studies have been completed:

- Geren F., Firincioglu T., Karacaer C., Ozkan E.: "Modeling Flow in Nanoporous, Membrane Reservoirs and Interpretation of Coupled Fluxes", paper SPE 170976 presented at the SPE Annual Technical Conference and Exhibition held in Amsterdam, The Netherlands, 27-29 October 2014.
- Geren F.: "Modeling Flow in Nanoporous, Membrane Reservoirs and Interpretation of Coupled Fluxes" MSc Thesis, Petroleum Engineering Department, Colorado School of Mines, 2014.

1.5 Anomalous-diffusion models in tight, fractured, unconventional reservoirs

In the last two decades, non-local, hereditary descriptions of flow and transport have gained notable popularity among scientists, engineers, and mathematicians focusing on applications in various forms of nano-porous systems. Until recently, these efforts have not attracted much attention in the oil-field applications due to the dominance of advective (Darcy) flow in conventional reservoirs. In unconventional shale-gas reservoirs, on the other hand, diffusive flow mechanisms have been recently incorporated into flow models due to their considerable contribution to flow in shale matrix.

In statistical physics, diffusion is the result of the random Brownian motion of individual particles. Classical (normal) diffusion is usually associated with homogeneous porous media. It is a special case where the random Brownian motion of the diffusing particles is governed by a Gaussian probability density whose variance is proportional to the first power of time; that is the mean square displacement of a

particle is a linear function of time ($\sigma_r^2 \sim t$). However, a convincing number of works have indicated anomalous diffusion in which the mean square variance grows faster (superdiffusion) or slower (subdiffusion) than that in a Gaussian diffusion process. Thus, a general relationship between the mean square variance and time is given by

$$\sigma_r^2 \sim t^{\alpha} \text{ where } \begin{cases} \alpha = 1 & \text{Normal diffusion} \\ \alpha \neq 1 & \text{Anomalous Diffusion} \\ \alpha > 1 & \text{Superdiffusion} \\ \alpha < 1 & \text{Subdiffusion} \end{cases}$$
(33)

Several mathematical assumptions can lead to anomalous diffusion formulation. These assumptions range from assuming that diffusion follows a power-law as a function of distance, fluid particles follow a continuous-time random walk (CTRW) behavior or that observation and correlation scales are different (Raghavan 2011). Due to the heterogeneous structure of porous media, diffusion can be faster or slower than normal diffusion. Thus, the application of anomalous diffusion becomes useful in replicating fluid flow in porous media, specifically at varying-porous scale. In addition, non-local anomalous diffusion arises in nano-pores since local gradients of the mean diffusion process are influenced by global pressure, which is governed by advective flow. Thus, the resulting non-local anomalous diffusion equation is scale and memory dependent (Ozkan 2013).

Several forms of the solution have been derived and provided for fluid flow in porous media with fractal properties. O'Shaughnessy and Procaccia (1985) used fractals approach and presented a modified normal diffusion equation. Scaling properties and normalizing probability arguments they obtained

$$\frac{\partial P(r,t)}{\partial t} = \frac{1}{r^{D-1}} \frac{\partial}{\partial r} \left[k(r) r^{D-1} \frac{\partial P(r,t)}{\partial r} \right]$$
(34)

In their solution, the conductivity, k(r), is defined as the total conductivity of a spherical shell of radius r and it involves product of spherically averaged values. Following their derivation and assuming a constant diffusion coefficient, , k(r) in Eq. 34 is defined as:

$$k(r) = Kr^{-\theta} \tag{35}$$

where $\theta = D + \alpha + 2$ is the anomalous diffusion coefficient, D is the fractal dimension, and α is the scaling power. The conductivity k(r) scales with the radial distance r using a power-law and the Laplacian operator is modified by including the coefficient D. Thus, Eq. 34 is isotropic in D dimensions. In addition, the solution assumes a steady-state conductivity that is assigned spatially. The asymptotic solution curve for anomalous diffusion probability-density function expresses a stretched shape. This formulation, however, neither provides the proper exponential function scaling nor meets the desired asymptotic behavior of the non-Gaussian probability function.

Hewett (1986) provided a correlation to distribute reservoir properties (permeability, porosity, etc.) using geostatistical parameters that correspond to a fractal system. His aim was to account for dispersion due to reservoir inhomogeneity and different scales of flow paths, which affect injected and recovered fluids. In modeling the reservoir, a Euclidean medium with statistical coefficients of fractional Brownian motion was assumed. In addition, well log data were incorporated to distribute the properties.

Chang and Yortsos (1990) presented a solution for NFRs based on the diffusion equation derived by O'Shaughnessy and Procaccia (1985). Their objective was to model natural fractures of different densities, conductivities and sizes. Also, they considered the natural fractures as a multi-fractal network defined by certain fractal parameters that is embedded in a Euclidean matrix. The equation governing fluid flow is given as:

$$\omega \frac{\partial P_{Df}}{\partial t_D} + (1 - \omega) r_D^{d-D} \frac{\partial P_{Dma}}{\partial t_D} = \frac{1}{r_D^{D-1}} \frac{\partial}{\partial r_D} \left(r_D^{\beta} \frac{\partial P_{Df}}{\partial t_D} \right)$$
 (36)

where the superscripts d and D are the Euclidean and mass fractal dimension, respectively. With θ being the spectral or conductivity exponent in their derivation, β was introduced as $\beta = D - \theta - 1$. In addition, the model accounted for pressure responses in two scenarios based on choosing the matrix to be interconnected or isolated from the well.

Beier (1994) also followed O'Shaughnessy and Procaccia (1985) and provided a solution for heterogeneous reservoirs. He utilized two domains to represent permeable and impermeable rocks with the permeable rock being a fractal network. Radial symmetry was assumed in obtaining the solution for a vertically fractured well with uniform flux and infinite-conductivity fracture as

$$\frac{\partial P}{\partial t} = \frac{0.000264\eta_r L_r^{\theta}}{r^d f^{-1}} \frac{\partial}{\partial r} \left(r^d f^{\left(-2d_f/d_s + 2\right)} \frac{\partial P}{\partial r} \right) \tag{37}$$

where d_s is the spectral coefficient and d_f is the mass fractal coefficient. Also, $\theta = 2 + d_w$ and $d_f = d_s(2 + \theta)/2$. Using uniform flux and infinite conductivity, Beier was able to apply the solution to field data. Also, he concluded that pressure expresses a power-law behavior during linear and radial flows.

Acuna and Yortsos (1995) used the solution by Chang and Yortsos (1990) and provided a numerical model for a synthetic fractal network combining the methods of fragmentation and iterated function system. They simulated the pressure transient response and concluded that well pressure is correlated with time by a power-law function. In addition, they were able to determine the spatial coefficient from the data.

Flamenco-Lopez and Camacho-Velázquez (2003) used the derivation from Chang and Yortsos (1990) and provided two solutions employing transient and pseudo-steady

state matrix-to-fracture transfer function; one with the matrix contributing to the flow and one without the matrix contribution. Incorporating the pressure transient response from transient and pseudo-steady state flow periods, they were able to determine the parameters describing the fractal geometry. Fuentes-Cruz et al. (2010) proposed a composite radial model with a fractal intermediate or transitional zone to analyze build-up and fall-off tests. Their goal was to represent the viscous fingering developed during fluid injection as an intermediate fractal region between the invaded and non-invaded reservoir regions. In their formulation, the permeability and porosity of the fractal region change with distance by

$$k(r) = k_1 \left(\frac{r}{r_1}\right)^{d_f - 2 - \theta} \tag{38}$$

and

$$\phi(r) = \phi_1 \left(\frac{r}{r_1}\right)^{d_f - 2}.\tag{39}$$

The terms ϕ_1 and k_1 are porosity and permeability of the invaded region and r is in the fractal region bounded by the invaded and non-invaded areas $(r_1 < r < r_2)$.

Cossio et al. (2012) derived a semi-analytical solution for an infinite single-porosity reservoir fully penetrated by a vertical fracture. Their solution is in a simplified form where porosity and permeability are spatially distributed with dimensionless distance raised to the exponents (df – θ – 2) for permeability and (df – 2) for porosity, similar to Fuentes-Cruz et al (2010). Their derivation for the Cartesian system can be transformed into radial flow by selecting proper scaling exponents and the authors stated that "a radial flow with constant hydraulic properties is equivalent to a linear flow with linearly increasing hydraulic properties" and the solution can be used to link linear and radial flows.

Several attempts have been made to derive a proper anomalous diffusion equation as well as applying some of these solutions to reservoir engineering problems. Schneider and Wyss (1989) provided a solution in the form of fractional integral equation as:

$$u(x,t) = f_0(x) + \frac{1}{\Gamma(\alpha)} \int_0^t d\tau (t - \tau)^{\alpha - 1} \Delta u(x, \tau)$$
(40)

where u(x,t) is the probability density, $f_0(x)$ is the initial distribution, $\alpha = dw/2$, and dw is the anomalous diffusion exponent. However, this solution fails to provide the distribution function asymptotic shape since only one free parameter, α , is provided (Metzler et al. 1994).

Giona and Roman (1992) tackled the spatial and temporal derivatives and obtained the following solution:

$$\frac{\partial^{\gamma} P(r,t)}{\partial t^{\gamma}} = -Gr^{-\theta'} \left[\frac{\partial P(r,t)}{\partial r} + \frac{k}{r} P(r,t) \right]$$
(41)

In this derivation, $\gamma = \frac{1+\theta'}{d_w}$ and $\theta' \geq 0$. They utilized an explicit reference to account for diffusion temporally and applied a linear relationship between the radial current and the average probability density function. Their solution meets the asymptotic behavior of the non-Gaussian probability density function. Yet, the derived expression has some limitations and it does not reduce to the isotropic Gaussian diffusion when the parameters are set for such diffusion.

Metzler et al. (1994) provided a fractional diffusion equation in the form

$$\frac{\partial^{2/d_{\mathbf{w}}}}{\partial t^{2/d_{\mathbf{w}}}} P(\mathbf{r}, t) = \frac{1}{r^{d_{\mathbf{s}}-1}} \frac{\partial}{\partial r} \left(r^{d_{\mathbf{s}}-1} \frac{\partial}{\partial r} P(\mathbf{r}, t) \right)$$
(42)

The parameters d_w and d_s are the diffusion exponent and spectral dimension, respectively. The derived equation is as follows

$$\langle \mathbf{r}^2 \rangle \sim \mathsf{t}^{2/\mathsf{d}_W} \tag{43}$$

for the anomalous diffusion and satisfy the asymptotic behavior of the non-Gaussian probability function. The temporal derivative carries the fraction $(2/d_w)$ and the spatial derivative carries $(d_s - 1)$. This solution incorporates variations of spatial properties and includes the time-dependent flux.

Camacho-Velázquez et al. (2008) provided a fractal fluid flow equation for NFRs using the diffusion equation form derived by Metzler et al. (1994). The solution was derived for a fractal reservoir including and excluding the matrix contribution during transient and boundary-dominated flow periods. Pressure responses were used to estimate fractal parameters, characterize the NFR and compare results with O'Shaughnessy and Procaccia (1985) model.

Raghavan (2011) used a CTRW model to derive a fractional equation for anomalous diffusion. The solution accounted for fractional temporal and spatial derivatives. Two models were provided, a radial flow model with symmetrical radial distribution of properties and a 2D Cartesian anisotropic model. Both solutions are applicable for production under constant rate or constant pressure. The equation for radial flow is given as:

$$\frac{1}{r^{n-1}} \frac{\partial}{\partial r} \left[r^{n-1} \lambda(r) \frac{\partial p(r,t)}{\partial r} \right] = \phi c \frac{\partial^{\gamma}}{\partial t^{\gamma}} p(r,t)$$
(44)

where n is the dimension and would be replaced by the fractal coefficient d_f .

Fomin et al. (2011) showed that an anomalous diffusion equation can be derived by either relating a variable mass flux to spatial coordinates or assuming a scaled diffusion coefficient. The diffusion equation is given as

$$\frac{\partial^{\gamma} C}{\partial t^{\gamma}} = \frac{\partial}{\partial x} \left(D_{f} \frac{\partial^{\beta} c}{\partial x^{\beta}} \right) \tag{45}$$

and the mass flux law is

$$J_{c} = D_{f} \, \partial_{t}^{1-\gamma} \left(\frac{\partial^{\beta} c}{\partial x^{\beta}} \right) \tag{46}$$

Raghavan and Chen (2013) revisited the solution in Raghavan (2011) and included the pseudo-skin function in the structure of the solution. They emphasized that the pseudo-skin function in their solution is time dependent and it would be independent of time if it were included in Chang and Yortsos (1990) or Beier (1994) formulations.

As suggested by Raghavan and Chen (2013a & b), the following constitutive relation (flux law) is used in this project to describe flow in naturally fractured nano-porous media:

$$\mathbf{v}_{\mathrm{I}} = -\lambda_{\alpha} \frac{\partial^{1-\alpha}}{\partial t^{1-\alpha}} \left(\frac{\partial \Delta \mathbf{p}_{\mathrm{I}}}{\partial \mathbf{x}} \right), \tag{47}$$

where $0 \le \alpha \le 1$ and λ_{α} is a phenomenological coefficient. It is assumed that the anomalous diffusion is related to the petrophysical heterogeneity of the medium and expresses the phenomenological coefficient in the following form:

$$\lambda_{\alpha} = \frac{k_{\alpha}}{\mu}. \tag{48}$$

The temporal fractional derivative in Eq. 47 is defined in the Caputo (1967) sense:

$$\frac{\partial^{\beta}}{\partial t^{\beta}} f(t) = \frac{1}{\Gamma(1-\beta)} \int_{0}^{t} \frac{\partial}{\partial t'} f(t') \frac{dt'}{(t-t')^{\beta}}.$$
 (49)

The convolution integral in Eq. 49 signifies the hereditary nature of anomalous diffusion on a heterogeneous velocity field. In addition, k_{α} in Eq. 48 is a dynamic property and different from the conventional Darcy permeability (it has the units of $L^2T^{1-\alpha}$). Physical interpretation of k_{α} is not straightforward and, based on Eqs. 47 through 49, static measurements are not suitable to determine k_{α} . Currently, the only viable technique to determine k_{α} is to match the dynamic (transient pressure or flow rate) data with an appropriate model.

Using the flux law (Eq. 47) with the mass conservation equation yields the following 2D, temporal-fractional (anomalous) diffusion equation:

$$\frac{\partial^2 \Delta p}{\partial x^2} + \frac{\partial^2 \Delta p}{\partial y^2} = \frac{1}{\eta_\alpha} \frac{\partial^\alpha}{\partial t^\alpha} \Delta p , \qquad (50)$$

where

$$\eta_{\alpha} = \frac{\lambda_{\alpha}}{(\phi c_{t})_{\alpha}}.$$
 (51)

Based on the premises of anomalous diffusion models in fractal porous media, an alternative to dual-porosity based formulations of flow in fractured unconventional reservoirs has been developed in this research. Specifically, the temporal-fractional diffusion equation given by Eq. 50 has been solved, subject to appropriate boundary conditions, and implemented in the trilinear flow idealization (Fig. 24) for a fractured horizontal well in a tight formation. The original trilinear flow model represents the stimulated reservoir volume (SRV) between hydraulic fractures by the dual porosity formulation (TDP). In the new model, the SRV is represented by the anomalous diffusion formulation (TAD). Ozcan (2014) provides the details of the derivation.

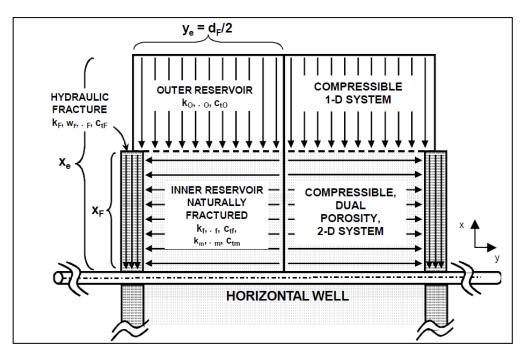


Figure 24 - Schematic of the trilinear flow model (Brown, 2009, Brown et al., 2011, Ozkan et al., 2011)

The results of the new TAD model have been compared with those of the original TDP model and the differences and similarities have been delineated. The data given in Tables 6 and 7 have been used in the test cases.

Table 6 – Well, Reservoir, and Fluid Data (Intrinsic Properties)

Formation thickness, <i>h</i> , ft	250
Wellbore radius, r_w , ft	0.25
Horizontal well length, L_h , ft	3000
Number of hydraulic fractures, n_F	15
Distance between hydraulic fractures, d_F , ft	200
Distance to boundary parallel to well (1/2 well spacing), x_e , ft	250
Inner reservoir size, y_e , ft	100
Viscosity, <i>μ</i> , cp	0.3
Hydraulic fracture porosity, $\phi_{\it F}$, fraction	0.38
Hydraulic fracture permeability, k_F , md	5.0E+04
Hydraulic fracture total compressibility, c_{tF} , psi $^{-1}$	1.0E-04
Hydraulic fracture half-length, x_F , ft	250
Hydraulic fracture width, w_F , ft	0.01
Outer reservoir permeability, k_0 , md	1.0E-04
Outer reservoir porosity, $\phi_{\it 0}$	0.05
Outer reservoir compressibility, c_{t0} , psi ⁻¹	1.0E-05
Constant flow rate, q, stb/day	150

Table 7 – Inner Reservoir Data

TDP (Intrinsic Properties)		TAD	
Matrix permeability, k_m , md	1.0E-4	Phenomenological coefficient, k_{α} , md-day ^{1-$lpha$}	1.2
Matrix porosity, ϕ_m	0.05	Porosity compressibility product, $(\phi c_t)_{\alpha}$, psi ⁻¹	4.62E-4
Matrix total compressibility, c_{tm} , psi ⁻¹	1.0E-5		
Natural fracture permeability, k_f , md	1.0E+3		
Natural fracture porosity, ϕ_f , fraction	0.7		
Natural fracture total compressibility, c_{tf} , psi ⁻¹	5.5E-1		
Natural fracture width, h_f , ft	3.0E-3		

To verify the TAD model, the asymptotic case of $\alpha=1$ has been used. This case corresponds to normal diffusion in a homogeneous reservoir, which can be obtained from the TDP solution for a homogeneous reservoir [f(s)=1] when k_f and $(\varphi c_t)_f$ are chosen equal to k_α and $(\varphi c_t)_\alpha$. The results in Fig. 25 show excellent agreement between the TAD and TDP solutions.

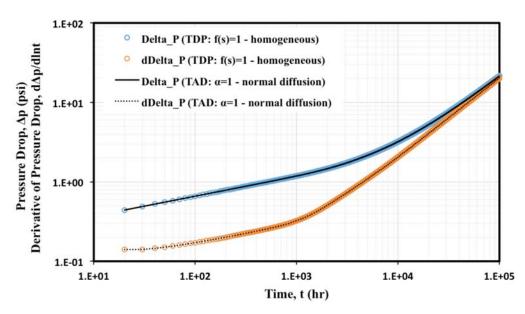


Figure 25: Verification of the TAD solution for normal diffusion (α =1) in a homogeneous reservoir.

As another verification, the results obtained from the TDP model for $k_f=10^6$ md and $k_m=10^{-4}$ md are matched with the TAD model. As shown by Fig. 26, the TAD model for $\alpha=0.8$ and $k_\alpha=1200$ provides a reasonable match with the TDP model. This example has been provided to show that the TAD model captures the naturally fractured reservoir behavior idealized by the TDP models. It does not, however, imply a general correspondence between the TAD and TDP models.

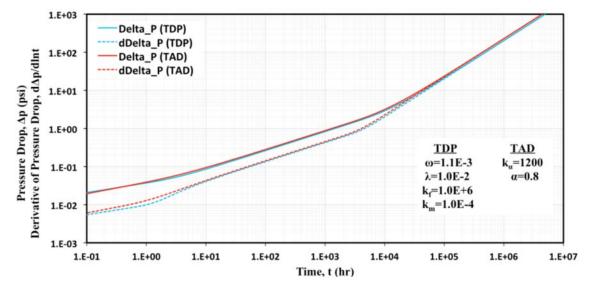


Figure 26: Matching TDP model results with the TAD solution.

Figure 27 shows the pressure and derivative responses of the TAD model for $0.1 \le \alpha \le 1$ and a fixed value of $k_\alpha = 1.2$. All pressure and derivative responses in Fig. 27 display straight-line trends at early, intermediate, and late times. As the straight-line trend is the diagnostic feature of a specific flow regime, existence of multiple straight lines for different values of α indicates the versatility of the TAD model to cover a large variety of flow regimes for fractured horizontal wells.

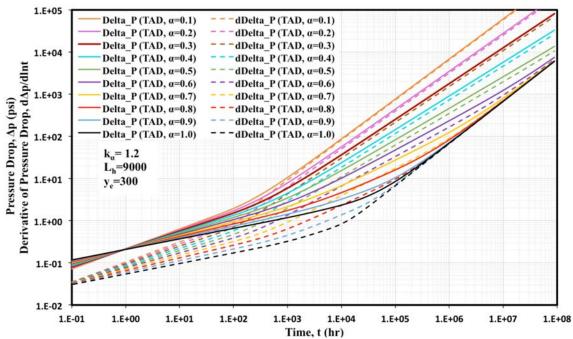


Figure 27 – Pressure and derivative responses obtained from the TAD solution for various α .

In Fig. 28, we consider the combined effects of the phenomenological coefficient, k_{α} , and the anomalous diffusion exponent, α , on pressure and derivative characteristics. The results in Fig. 28 indicate that an increase in k_{α} for constant α decreases both the pressure drop and the derivative values. Variations of α for constant k_{α} , on the other hand, cause a change in both the magnitude of the pressure drop and the flow regime characteristics (indicated by the changing slopes of the derivative responses). It should be also noted that the variation of k_{α} for constant α causes a parallel shift in the pressure and derivative responses for all practical times for $\alpha \leq 0.5$ and at early and intermediate times for $\alpha > 0.5$. The pressure and derivative responses become independent of α at late times for $\alpha > 0.5$.

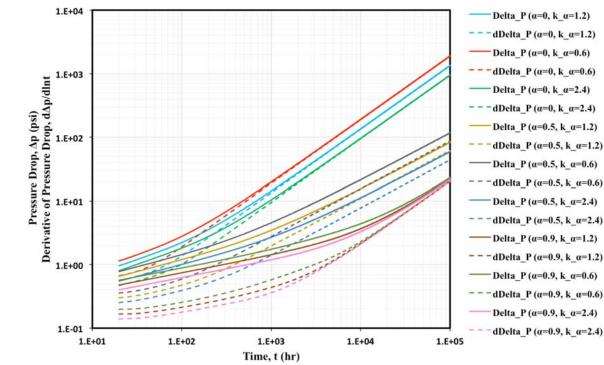


Figure 28 – Combined effect of k and α on pressure and derivative characteristics of TDP model

For completeness, we also present the rate decline characteristics of the TAD model as a function of α in Fig. 29. The physical interpretations presented for the pressure and derivative responses in Figs. 5 and 6 are also applicable to the rate-transient responses shown in Fig. 9. The early-time rate responses after the intersection time display straight lines with slopes between 1/4 for $\alpha=1$ and 1/2 for $\alpha=0$. The early-time straight lines for $\alpha=1$ and 0 are followed by sharp exponential-decline periods, which are the terminal flow regimes for these cases. For $\alpha=0$ exponential decline corresponds to the depletion of a system consisting mostly of a tight-matrix. On the other hand, for $\alpha=1$, the system is dominated by natural-fractures and their depletion causes the exponential decline behavior.

For $0 < \alpha < 1$, the flow rates in Fig. 29 display straight lines with slopes less than or equal to 1 ($\alpha = 0.1$) and greater than or equal to 1/2 ($\alpha = 0.9$) at intermediate (for $\alpha > 0.5$) and late times (for $\alpha \le 0.5$). For $\alpha \le 0.5$, the delay of flow by the tight matrix causes a sharper drop in the flow rates at intermediate times before the display of the late-time straight lines. For $\alpha > 0.5$, the higher decline rates follow the intermediate-time straight lines.

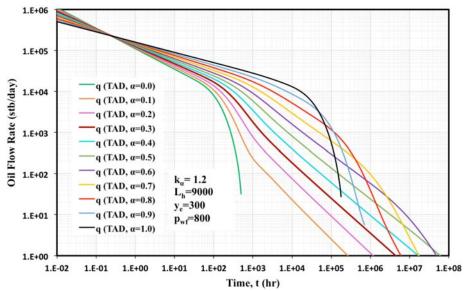


Figure 29 – Rate declines obtained from the TAD solution for various α .

To demonstrate the application of the TAD model to field data, we also considered the Barnett field data analyzed by Brown et al. (2011) by using the TDP model. The details of the data are given in Brown et al. (2011). Fig. 30 shows the matching of the data by the TAD model. For comparison, the match obtained by Brown et al. (2011) is also shown in Fig. 30. Both the TAD and TDP models yield a reasonable match and it is not possible to choose one over the other. However, because the TAD model does not require explicit references to the intrinsic properties of the matrix and natural fractures, the TAD model requires fewer regression parameters than the TDP model.

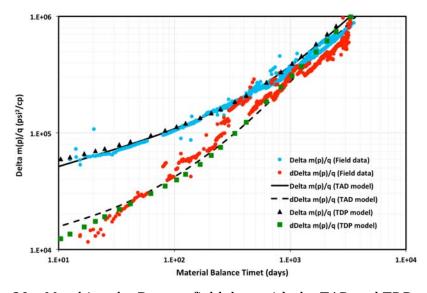


Figure 30 – Matching the Barnett field data with the TAD and TDP models.

The results summarized above have led to the following conclusions:

- Anomalous diffusion formulation is a viable alternative to dual-porosity idealization of tight, fractured unconventional reservoirs.
- The anomalous diffusion formulation does not require explicit references to the intrinsic properties of the matrix and fracture media and thus relaxes the stringent requirements used in dual-porosity idealizations to couple matrix and fracture flows.
- The interpretations of the pressure and flow rate behaviors predicted by the anomalous diffusion model are consistent with the physical expectations and the results of the dual porosity models.

As a result of the research on anomalous diffusion in tight, fractured, unconventional reservoirs, the following studies are completed:

- Ozcan O., Sarak H., Ozkan E., Raghavan R.: "A Trilinear Flow Model for a Fractured Horizontal Well in a Fractal Unconventional Reservoir", paper SPE 170971 presented at the SPE Annual Technical Conference and Exhibition held in Amsterdam, The Netherlands, 27-29 October 2014.
- Ozcan O.: "Fractional Diffusion in Naturally Fractured Unconventional Reservoirs" MSc Thesis, Petroleum Engineering Department, Colorado School of Mines, 2014.
- Albinali A.: "Analytical Modeling of Fractured Nano-porous Reservoirs" A Dissertation Proposal for Doctor of Philosophy in Petroleum Engineering, Petroleum Engineering Department, Colorado School of Mines, 2014.

PROJECT 2: Fluid Transfer Between Nano-Porous Matrix and Multi-Scale Fractures

Objectives: Define the interface conditions and fluid transfer mechanisms between nano-porous matrix and fractures to more realistically account for the contribution of ultra-tight, unconventional rock matrix.

Tasks:

- Fluid flow between fractures and nano-porous rock matrix (to be considered in Phase 2)
- Models of flow from nano-porous matrix to multi-level fractures (partial work done; continuing into Phase 2)

Deliverables:

- Conditions of pressure- and flux continuity at the interface (to be considered in Phase 2)
- Thermodynamics and blockage mechanisms at the interface (to be considered in Phase 2)
- Flow models for nano-porous matrix with multi-level fractures (initial results available; more work in Phase 2)

Summary of Project 2 Results:

2.1. Analytical Dual-Porosity Models with Anomalous Diffusion

The most commonly used models to describe fluid flow in naturally fractured reservoirs (NFR) are the dual-porosity/single-permeability models, often referred to as dual-porosity (DP) models (Barenblatt et al., 1960, Warren and Root, 1963, and Kazemi, 1969). Due to their computational convenience and reduced data requirements, DP models are also preferred to represent flow in naturally fractured unconventional reservoirs. DP models rely on the premise that matrix provides storage and fractures provide conductive paths.

The original need and justification of the DP models rest, primarily, on the fractured carbonate reservoirs of the Middle East. The distinguishing features of these reservoirs are the decent matrix permeability (in the tens to hundreds of md) and extremely high fracture permeability (super-K fractures). Under these conditions, the fracture network is the preferred flow medium, but it is depleted quickly. Because the matrix has reasonable permeability, when the fracture network is depleted, the matrix starts supporting the flow in the fracture system. The permeabilities of the matrix and fracture network are such that the fluid velocities are high in both media to permit

modeling in terms of average properties and pressures and the representation of the matrix and fracture media as overlapping continua.

In unconventional reservoirs, both the matrix and fracture permeabilities are significantly downscaled and the matrix permeability reaches nano-Darcy scale where contribution of Darcy flow is negligible. In general, nano-porous unconventional reservoirs possess multiple flow mechanisms at different scales. Advection is the fastest of all; however, its contribution to total flow is the minimum because of the small proportion of the pores in which Darcy flow occurs. In nano-pores, much slower diffusive processes occur. The local diffusion is, on the other hand, a function of the global pressure distribution; i.e., the advective flow. This problem lends itself to a non-local flow and transport formulation. In unconventional reservoirs, it is important to consider non-local diffusion in matrix nano-pores under the global influence of the pressure field dominated by the advective flow in fractures. An approach for non-local modeling of flow in nano-porous unconventional reservoirs with long-range interactions is to use a fractional diffusion equation. The fractional Laplacian operator acts by a global integration, instead of a point-wise differentiation, which represent the nonlocal character of the process.

As discussed in Project 1, Ozcan et al. (2014) incorporated anomalous diffusion into the tri-linear model of fractured horizontal wells in tight unconventional reservoirs. In this model, time-fractional flux was assumed to govern diffusion in the naturally fractured inner reservoir between hydraulic fractures. In general, this model assumed that the flow in an effective medium with the properties natural fractures would be intercepted and slowed down by a heterogeneously distributed and discrete low-permeability matrix system.

In the current research, two sets of natural fractures are considered in unconventional reservoirs. The first set consists of globally distributed, continuum-forming macro-scale fractures of high conductivity (usually developed as a result of tectonic activities) and the second set includes the micro-scale, discontinuous, low-conductivity natural fractures embedded in the matrix (these are assumed to have developed as a result of kerogen maturation). Three combinations of anomalous and normal diffusion are possible to model flow in naturally fractured media:

- i) Case 1: Anomalous diffusion can be used to introduce the effect of heterogeneity caused by the matrix and fractures into a single-porosity (SP) medium.
- ii) Case 2: Flow in the fracture network can be represented by normal diffusion while flow in the matrix is modeled by anomalous diffusion. The matrix and the fracture media flows can then be coupled by using the DP idealization.

iii) Case 3: Flows in both matrix and fracture media are governed by anomalous diffusion and coupled by DP idealization.

Case 1 has been considered in Project 1 (Ozcan et al. 2014). The second and the third options are being investigated in the current research.

As of Nov. 2015, Case 2, which considers time-fractional diffusion in the matrix and normal diffusion (Darcy flow) in the fractures, has been formulated and numerically implemented. In this case, the size, connectivity, and conductivity of macro-fractures warrant the continuum assumption and Darcy flow. Matrix flow, on the other hand, takes place on a heterogeneous velocity field formed by a complex distribution and connection of inorganic matrix, organic material, and small, discontinuous fractures and can be represented by anomalous diffusion formulation. Following the classical DP approach, the matrix was modeled as the distributed source term for the fracture system and the fluid transfer from matrix to fractures was assumed to take place under transient anomalous diffusion.

For convenience, the DP solution for Case 2 was first developed for a vertical well in a cylindrical reservoir (Fig. 31). The matrix blocks were represented as spheres (other matrix shapes can also be considered) and a general solution was obtained for 1D, spherical, time-fractional diffusion equation. Pressure and flux continuity at the matrix-fracture interface served as the boundary condition for the matrix with the assumption that the flux from the matrix is instantaneously and uniformly distributed in the encircling fracture volume. The matrix solution was then coupled with the fracture solution, which was obtained from the radial diffusion equation for an infinite reservoir with a vertical well producing at a constant flow rate. The outcome of this solution was the definition of a new DP transfer function, f(s), accounting for anomalous diffusion in the matrix. Then the DP transfer function was used to modify the inner reservoir (between hydraulic fractures) solution in the tri-linear model of fractured horizontal wells proposed by Ozkan et al. (2009).

The details of the new DP model solution will be provided in the PhD dissertation of Albinali (2015). Here we briefly mention the key features of the solution. Raghavan and Chen (2013) presented a 1D, time-fractional, flux equation that is based on a Continuous Time Random Walk (CTRW) process in the form:

$$v(\mathbf{r}, \mathbf{t}) = -\lambda_{\alpha} \frac{\partial^{1-\alpha}}{\partial \mathbf{t}^{1-\alpha}} \left(\frac{\partial \mathbf{p}}{\partial \mathbf{r}} \right), \tag{52}$$

where the fractional time derivative, $\partial^{1-\alpha}/\partial t^{1-\alpha}$, is defined in the Caputo (1967) sense by

$$\frac{\partial^{\alpha}}{\partial t^{\alpha}}f(t) = \frac{1}{\Gamma(1-\alpha)} \int_{0}^{t} dt' (t-t')^{-\alpha} \frac{\partial}{\partial t'} f(t'). \tag{53}$$

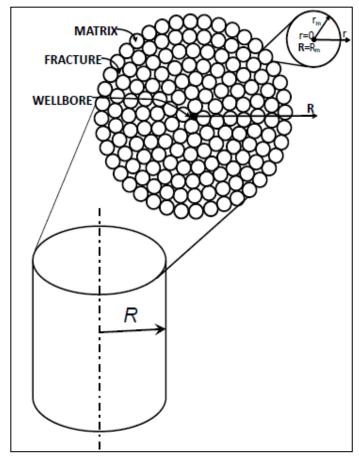


Figure 31 - Illustration of Cylindrical Dual-porosity System (Ozkan 2011)

The exponent α in Eq. 52 is related to the anomalous diffusion index θ by:

$$\alpha = \frac{2}{2+\theta}.\tag{54}$$

The normal-diffusion equation for the fracture system is given in radial coordinates as follows:

$$\frac{1}{R}\frac{\partial}{\partial R}\left(R\frac{k_f}{\mu}\frac{\partial p_f}{\partial R}\right) + \hat{q}_m = (\phi c_t)_f \frac{\partial p_f}{\partial t}.$$
 (55)

The matrix source term, \hat{q}_m , in Eq. 55 is obtained from Eq. 52. Carrying out the derivations (Albinali, 2015), we obtain the following DP solution in Laplace domain where the fracture experiences normal diffusion while the flow in the matrix is under anomalous diffusion conditions:

$$\frac{1}{R_{D}} \frac{\partial}{\partial R_{D}} \left(R_{D} \frac{\partial \overline{p}_{fD}}{\partial R_{D}} \right) - s \left\{ 1 + \frac{2k_{m}r_{w}}{h_{f}k_{f}} \left(\frac{\eta_{f}}{r_{w}^{2}} \right)^{1-\alpha} \frac{r_{mD}\sqrt{\beta_{m}}}{Tanh(\sqrt{\beta_{m}}r_{mD})} s^{-\alpha} \right\} \overline{p}_{fD} = 0.$$
 (56)

Note here that the expression bounded by the curly brackets in Eq. 56,

$$f(s) = 1 + \frac{2k_{\rm m}r_{\rm w}}{h_{\rm f}k_{\rm f}} \left(\frac{\eta_{\rm f}}{r_{\rm w}^2}\right)^{1-\alpha} \frac{r_{\rm mD}\sqrt{\beta_{\rm m}}}{{\rm Tanh}(\sqrt{\beta_{\rm m}}r_{\rm mD})} s^{-\alpha}$$

$$(57)$$

is the dual-porosity transfer function, which is particular to the setup of the model. Although formulation of Eq. 56 is for a vertical well in an infinite-acting radial-flow system, the f(s) function in Eq. 57 is independent of the flow geometry and well type. Therefore, substituting the new f(s) function in Eq. 57 for the f(s) function in the original tri-linear model (Fig. 24), we obtain the new tri-linear model, which considers anomalous diffusion in the matrix system of the SRV. Additional details of the solution will be documented in the PhD dissertation of Albinali (2015). Some preliminary results of Case 2 are available and noted below.

The solution was first verified by comparison with the tri-linear, normal diffusion model. In Fig. 32, TLM denotes the tri-linear, normal diffusion model and TAD is the new solution with anomalous diffusion in the matrix system. Setting the exponent $\alpha=1$ in TAD model reverts the matrix flow into normal diffusion. The data used in Fig. 32 are given in Table 8. The same matrix and fractures properties were entered for both models [the matrix properties k_m and $(\phi c_t)_m$ in the TLM model are equivalent to k_α and $(\phi c_t)_\alpha$ in the TAD model]. The two solutions are in excellent agreement.

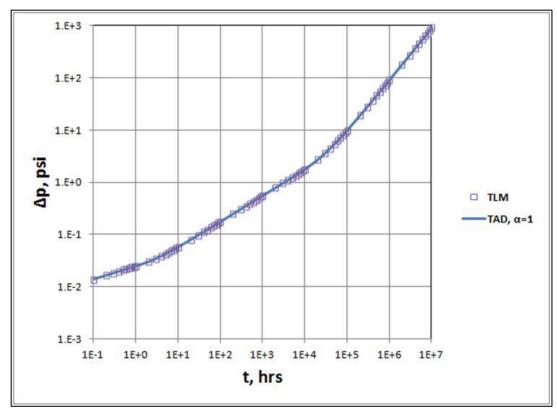


Figure 32 – Comparison of the trilinear anomalous-diffusion model for $\alpha=1$ with the trilinear normal-diffusion model

Table 8 – Data used for the model verification in Fig. 32

WELL, RESERVOIR, AND FLUID DATA		
Formation thickness, h, ft	250	
Wellbore radius, r_w , ft	0.25	
Horizontal well length, L_h , ft	2800	
Number of hydraulic fractures, n_F	15	
Distance between hydraulic fractures, d_F , ft	200	
Distance to boundary parallel to well (1/2 well spacing), x_e , ft	250	
Inner reservoir size, <i>y_e</i> , ft	100	
Viscosity, <i>μ</i> , cp	0.3	
Hydraulic fracture porosity, ϕ_F , fraction	0.38	
Hydraulic fracture permeability, k_F , md	5.0E+4	
Hydraulic fracture total compressibility, c_{tF} , psi $^{-1}$	1.0E-4	
Hydraulic fracture half-length, x_F , ft	250	
Hydraulic fracture width, w_F , ft	0.01	
Matrix permeability, k_m , md	1.0E-4	
Matrix porosity, ϕ_m	0.05	
Matrix compressibility, c_{tm} , psi ⁻¹	1.0E-5	
Constant flow rate, q, stb/day	1.5E+2	

Sensitivity Runs-A1 and A2 shown in Figs. 33 and 34, respectively, were conducted to determine the effects of the exponent α with different natural fractures densities ρ_f . In Runs-A1 (Fig. 33), four values of $\alpha=\{1,0.7,0.3,0.1\}$ were considered for two values $\rho_f=\{0.9,0.3\}$ and, in Runs-A2 (Fig. 34), four values of $\rho_f=\{0.9,0.6,0.3,0.03\}$ were considered for two values of $\alpha=\{1,0.1\}$. Theoretically, when α deviates from one, fluid flow in the matrix deviates from normal diffusion, and the larger values of ρ_f correspond to denser and better-connected natural fractures. As expected, Figs. 33 and 34 show that the pressure drop becomes larger as the flow in the matrix deviates further from normal diffusion. This is a result of the "retardation" of flow in the matrix system. Similarly, the pressure drop is larger when there are fewer natural fractures because of faster depletion of the smaller volume of fluid stored in conductive fractures. Overall, these preliminary results verify the solution and indicate the potential of the new model to account for the heterogeneities in the matrix system.

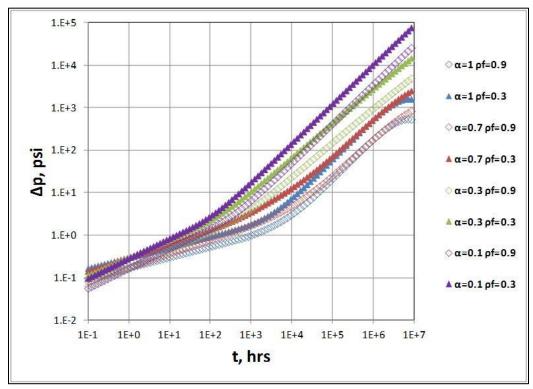


Figure 33: Sensitivity Runs-A1

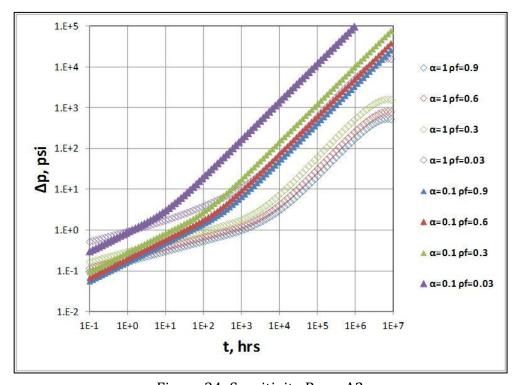


Figure 34: Sensitivity Runs-A2

2.2. Numerical Modeling of Anomalous Diffusion in Unconventional Reservoirs

2.2.1 Background

The focus of this research is to derive and implement a numerical model to better describe and capture the flow of hydrocarbons in ultra tight unconventional reservoirs based on the concept of anomalous diffusion. The classic diffusion equation used in describing flow in conventional reservoirs is based on the well-known Darcy's Law which itself is derived from the fact that particle displacement follows Brownian motion which is only valid in homogeneous media. The current approach to treating naturally fractured reservoirs is by using dual-porosity models in which average properties are used to describe the matrix on one hand and the continuous fracture network on the other. While this approach is suited for conventional naturally fractured reservoirs in which heterogeneity is mainly observed at one scale, unconventional (e.g. shale) reservoirs are dominated by multi-scale and discontinuous fractures coupled with a complex nano-porous matrix. Such a system can no longer simply be described by the dual-porosity (or multi-porosity) approach, as it would require a large amount of measurements at all scales as well as a very detailed computational model. By introducing the concept of anomalous diffusion in highly heterogeneous media through the use of fractional calculus, it should be possible to more accurately model the fluid flow as well as properly capture the complexity of the modeled system across all scales without over-discretizing the numerical model.

2.2.2. Anomalous Diffusion Equation in Petroleum Engineering Applications

The anomalous diffusion equation used is derived from a modified flux law coupled with the classic mass conservation equation. The modified flux law incorporating space and time non-locality for single-phase flow is given by:

$$\vec{u} = -\frac{\bar{k}_{\alpha,\beta}}{\mu_o} \frac{\partial^{1-\alpha}}{\partial t^{1-\alpha}} \nabla^{\beta} P_o \tag{58}$$

where $0<\alpha<1$ and $0<\beta<1$ are the fractional derivative exponents in time and space respectively, $\bar{k}_{\alpha,\beta}$ is the anomalous permeability tensor with field units $mD.d^{1-\alpha}ft^{\beta-1}$, and ∇^{β} is the fractional gradient defined in the three dimensional Cartesian coordinate system as:

$$\nabla^{\beta} = \left[\frac{\partial^{\beta}}{\partial x^{\beta}}, \frac{\partial^{\beta}}{\partial y^{\beta}}, \frac{\partial^{\beta}}{\partial z^{\beta}} \right]^{T} \tag{59}$$

It should be noted that space and time fractional derivatives are taken in the Caputo sense, which will be elaborated in the next sections.

The classic mass conservation equation including source/sink term \hat{q}_o is defined as:

$$-\nabla \cdot \left(\frac{\vec{u}}{B_o}\right) + \frac{\hat{q}_o}{B_o} = \frac{\phi c_t}{B_o} \frac{\partial P_o}{\partial t} \tag{60}$$

Combining Eqs. 58, 59, and 60 we obtain the general anomalous diffusion equation for single phase, slightly compressible flow:

$$\nabla \cdot \left(\frac{1}{B_o} \frac{\bar{k}_{\alpha,\beta}}{\mu_o} \frac{\partial^{1-\alpha}}{\partial t^{1-\alpha}} \nabla^{\beta} P_o \right) + \frac{\hat{q}_o}{B_o} = \frac{\phi c_t}{B_o} \frac{\partial P_o}{\partial t}$$
(61)

In Phase I of the research the model has been restricted to one-dimensional single phase, slightly compressible flow with uniform 'anomalous permeability' coefficient. Based on these assumptions the diffusion Eq. 61 is simplified and rearranged to the following form:

$$\frac{k_{\alpha,\beta_{\chi}}}{B_{o}\mu_{o}} \left(\frac{\partial^{1+\beta}P_{o}}{\partial x^{1+\beta}} \right) + \frac{1}{B_{o}} \frac{\partial^{-(1-\alpha)}}{\partial t^{-(1-\alpha)}} (\hat{q}_{o}) = \frac{\phi c_{t}}{B_{o}} \frac{\partial^{\alpha}P_{o}}{\partial t^{\alpha}}$$

$$(62)$$

This anomalous diffusion equation contains fractional derivatives in space and time, as well as a fractional integral in time. In the following section an implicit finite difference scheme is derived to solve an initial boundary value problem (IBVP) with uniform initial pressure distribution and no-flux boundaries.

2.2.3. Finite Difference Discretization

The IBVP to be solved is as follows:

$$\frac{k_{\alpha,\beta_{x}}}{B_{0}\mu_{0}} \left(\frac{\partial^{1+\beta}P_{0}}{\partial x^{1+\beta}} \right) + \frac{1}{B_{0}} \frac{\partial^{-(1-\alpha)}}{\partial t^{-(1-\alpha)}} (\hat{q}_{0}) = \frac{\phi c_{t}}{B_{0}} \frac{\partial^{\alpha}P_{0}}{\partial t^{\alpha}} \quad \text{for } \alpha < x < b, \ t > 0$$
 (63)

$$P_o(x,0) = P_{o,initial} \qquad \qquad for \ a \le x \le b \tag{64}$$

$$\frac{\partial P_o(a,t)}{\partial x} = \frac{\partial P_o(b,t)}{\partial x} = 0 \qquad \qquad for \ t \ge 0$$

The spatial domain [a,b] is discretized into a uniform block-centered grid of Imax grid blocks and block length $\Delta x = (b-a)/Imax$. The grid block centers are labeled with the index x_i , i=1,...,Imax. Similarly, the time domain [0,T] is discretized into N time steps of uniform length $\Delta t = T/N$ and the time steps are labeled with the index $t_n, n=1,...,N+1$. The numerical approximations of the functions $P_o(x_i,t_n)$ and $\hat{q}_o(x_i,t_n)$ are denoted by $P_{o_i}^n$ and $\hat{q}_{o_i}^n$ respectively.

Time Fractional Derivative: The time fractional derivative is defined in the Caputo sense, allowing for the use of integer order initial conditions:

$$\frac{\partial^{\alpha} P_o(x_i, t_n)}{\partial t^{\alpha}} = {}^C D_{t+}^{\alpha} = \frac{1}{\Gamma(1-\alpha)} \int_{t_{1=0}}^{t_n} \frac{\partial P_o(x_i, \tau)}{\partial t} (t - \tau)^{-\alpha} d\tau \tag{66}$$

For the implicit scheme, the derivative term in the integral is approximated by the first order forward difference and the integral can be rewritten as summation of integrals over time Δt as shown in Murio (2008):

$$\frac{\partial^{\alpha} P_o(x_i, t_n)}{\partial t^{\alpha}} = \frac{1}{\Gamma(1-\alpha)} \sum_{l=1}^{n} \frac{P_o_i^{l+1} - P_o_i^{l}}{\Delta t} \int_{(l-1)\Delta t}^{l\Delta t} (t_n - \tau)^{-\alpha} d\tau \tag{67}$$

Integration of the integral term leads to:

$$\frac{\partial^{\alpha} P_{o}(x_{i}, t_{n})}{\partial t^{\alpha}} = \frac{1}{\Gamma(1 - \alpha)} \sum_{l=1}^{n} \frac{P_{o_{i}}^{l+1} - P_{o_{i}}^{l}}{\Delta t} \left[-\frac{(t_{n} - \tau)^{1 - \alpha}}{1 - \alpha} \right]_{(l-1)\Delta t}^{l\Delta t}$$

$$= \frac{1}{\Gamma(2 - \alpha)} \sum_{l=1}^{n} \frac{P_{o_{i}}^{l+1} - P_{o_{i}}^{l}}{\Delta t} \left[-(t_{n} - \tau)^{1 - \alpha} \right]_{(l-1)\Delta t}^{l\Delta t}$$

$$= \frac{1}{\Gamma(2 - \alpha)} \sum_{l=1}^{n} \frac{P_{o_{i}}^{l+1} - P_{o_{i}}^{l}}{\Delta t} \left[(n\Delta t - (l-1)\Delta t)^{1 - \alpha} - (n\Delta t - l\Delta t)^{1 - \alpha} \right]$$

$$= \frac{1}{\Gamma(2 - \alpha)} \sum_{l=1}^{n} \frac{P_{o_{i}}^{l+1} - P_{o_{i}}^{l}}{\Delta t} \left[(n-l+1)^{1 - \alpha} - (n-l)^{1 - \alpha} \right] \Delta t^{1 - \alpha}$$

$$= \frac{1}{\Gamma(2 - \alpha)} \frac{1}{\Delta t^{\alpha}} \sum_{l=1}^{n} (P_{o_{i}}^{l+1} - P_{o_{i}}^{l}) \left[(n-l+1)^{1 - \alpha} - (n-l)^{1 - \alpha} \right]$$

Or after shifting indices, the implicit Caputo approximation becomes:

$$\frac{\partial^{\alpha} P_o(x_i, t_n)}{\partial t^{\alpha}} = \sigma_{\alpha, \Delta t} \sum_{l=1}^{n} \omega_l^{(\alpha)} \left(P_o_i^{n+2-l} - P_o_i^{n+1-l} \right)$$
(69)

where

$$\sigma_{\alpha,\Delta t} = \frac{1}{\Gamma(2-\alpha)} \frac{1}{\Lambda t^{\alpha}} \tag{70}$$

and

$$\omega_l^{(\alpha)} = l^{1-\alpha} - (l-1)^{1-\alpha} \tag{71}$$

Two important observations can be made from the fractional time derivative approximation (Eq. 69). First, the evaluation of the pressure at t_{n+1} requires the pressures at all previous time steps from $P_{oi}^{\ 1} = P_{o,initial}$ to $P_{oi}^{\ n}$. Second, for $\alpha \to 0$

 $1,\omega_1^{(\alpha)}=1,\omega_l^{(\alpha)}\to 0, l=2,...,n$ and the approximation reverts back to the classic forward difference approximation.

Time Fractional Integral: The time fractional integral of the source/sink term is evaluated using the Riemann-Liouville integral up to time step t_{n+1} for the implicit scheme.

$$\frac{\partial^{-(1-\alpha)}}{\partial t^{-(1-\alpha)}} \hat{q}_o(x_i, t_{n+1}) = I_{t+}^{1-\alpha} = \frac{1}{\Gamma(1-\alpha)} \int_{t_1=0}^{t_{n+1}} \hat{q}_o(x_i, \tau) (t_{n+1} - \tau)^{-\alpha} d\tau$$
 (72)

Integrating by parts once:

$$\frac{\partial^{-(1-\alpha)}}{\partial t^{-(1-\alpha)}} \hat{q}_{o}(x_{i}, t_{n+1}) = \frac{1}{\Gamma(1-\alpha)} \left[\hat{q}_{o}(x_{i}, \tau) \frac{-(t_{n+1}-\tau)^{1-\alpha}}{(1-\alpha)} \right]_{0}^{t_{n+1}} \\
- \frac{1}{\Gamma(1-\alpha)} \int_{0}^{t_{n+1}} \frac{\partial \hat{q}_{o}(x_{i}, \tau)}{\partial t} \frac{-(t_{n+1}-\tau)^{1-\alpha}}{(1-\alpha)} d\tau \\
= \hat{q}_{o}(x_{i}, 0) \frac{t_{n+1}^{1-\alpha}}{\Gamma(2-\alpha)} + \frac{1}{\Gamma(2-\alpha)} \int_{0}^{t_{n+1}} \frac{\partial \hat{q}_{o}(x_{i}, \tau)}{\partial t} (t_{n+1} - \tau)^{1-\alpha} d\tau$$
(73)

The second term in the last equality of Eq. 73 can be discretized following the same procedure as for the time fractional derivative, leading to the following finite difference approximation:

$$\frac{\partial^{-(1-\alpha)}}{\partial t^{-(1-\alpha)}} \hat{q}_{o}(x_{i}, t_{n+1}) = \hat{q}_{o} \frac{1}{i} \frac{(n\Delta t)^{1-\alpha}}{\Gamma(2-\alpha)} + \frac{1}{\Gamma(3-\alpha)} \frac{1}{\Delta t^{\alpha-1}}
\times \sum_{l=1}^{n} \left(\hat{q}_{o} \frac{n+2-l}{i,j} - \hat{q}_{o} \frac{n+1-l}{i-l,j} \right) [l^{2-\alpha} - (l-1)^{2-\alpha}]$$
(74)

In case of a constant rate the second term in the approximation given by Eq. 74 vanishes and we obtain:

$$\frac{\partial^{-(1-\alpha)}}{\partial t^{-(1-\alpha)}} \hat{q}_o(x_i, t_{n+1}) = \hat{q}_{oi} \frac{(n\Delta t)^{1-\alpha}}{\Gamma(2-\alpha)}$$

$$\tag{75}$$

Finally for $\alpha \to 1$ Eq. 74 reverts back to $\hat{q}_{o_i}^{n+1}$ and Eq. 75 becomes simply \hat{q}_{o_i} as in the classic diffusion equation.

Space Fractional Derivative: In order to allow for flow contributions in the positive and negative x-direction, the two-sided Caputo derivative is used which is a weighted combination of left and right side derivatives.

$$\frac{\partial^{1+\beta}}{\partial x^{1+\beta}} P_o(x_i, t_{n+1}) = \vartheta^C D_{x+}^{1+\beta} + (1-\vartheta)^C D_{x-}^{1+\beta}$$
(76)

Here $0 < \vartheta < 1$ is the weighting factor allowing for adjustment of flow contributions from either side of the point of interest.

The left-sided Caputo derivative (from the left boundary to point x_i) is defined as:

$${}^{C}D_{x+}^{1+\beta} = \frac{1}{\Gamma(2-(1+\beta))} \int_{a}^{x_{i}} \frac{\partial^{2}P_{o}(\xi,t)}{\partial x^{2}} (x_{i} - \xi)^{1-(1+\beta)} d\xi \tag{77}$$

The right-sided Caputo derivative (from point x_i to the right boundary) is defined as:

$${}^{C}D_{x-}^{1+\beta} = \frac{1}{\Gamma(2-(1+\beta))} \int_{x_{i}}^{b} \frac{\partial^{2}P_{o}(\xi, t_{n+1})}{\partial x^{2}} (\xi - x_{i})^{1-(1+\beta)} d\xi$$
 (78)

Both derivatives can be discretized using a similar approach as for the time derivative (Liu et al. 2003). The following shows the discretization of the left sided derivative. Since a block-centered grid is used and the boundary is defined as no-flow boundary the integral range is shifted to $[x_1, x_i]$:

$${}^{C}D_{x+}^{1+\beta} = \frac{1}{\Gamma(2-(1+\beta))} \int_{x_{1}}^{x_{i}} \frac{\partial^{2}P_{o}(\xi, t_{n+1})}{\partial x^{2}} (x_{i} - \xi)^{1-(1+\beta)} d\xi$$
 (79)

The second derivative in the integral is approximated by the second order central difference and the integral can be rewritten as summation of integrals over uniform space intervals Δx :

$$CD_{x+}^{1+\beta} \cong \frac{1}{\Gamma(2-(1+\beta))} \sum_{l=1}^{i} \frac{(P_{l+1}^{n+1} - 2P_{l}^{n+1} + P_{l-1}^{n+1})}{\Delta x^{2}} \int_{(l-1)\Delta x}^{l\Delta x} (x_{i} - \xi)^{1-(1+\beta)} d\xi$$

$$= \frac{1}{\Gamma(2-(1+\beta))} \sum_{l=1}^{i} \frac{(P_{l+1}^{n+1} - 2P_{l}^{n+1} + P_{l-1}^{n+1})}{\Delta x^{2}} \left[\frac{-(x_{i} - \xi)^{2-(1+\beta)}}{2-(1+\beta)} \right]_{(l-1)\Delta x}^{l\Delta x}$$

$$= \frac{1}{\Gamma(3-(1+\beta))} \sum_{l=1}^{i} \frac{(P_{l+1}^{n+1} - 2P_{l}^{n+1} + P_{l-1}^{n+1})}{\Delta x^{2}} \left[-(x_{i} - \xi)^{2-(1+\beta)} \right]_{(l-1)\Delta x}^{l\Delta x}$$

$$= \frac{1}{\Gamma(3-(1+\beta))} \sum_{l=1}^{i} \frac{(P_{l+1}^{n+1} - 2P_{l}^{n+1} + P_{l-1}^{n+1})}{\Delta x^{2}}$$

$$\times \left[(i\Delta x - (l-1)\Delta x)^{2-(1+\beta)} - (i\Delta x - l\Delta x)^{2-(1+\beta)} \right]$$

$$= \frac{1}{\Gamma(3-(1+\beta))} \sum_{l=1}^{i} \frac{(P_{l+1}^{n+1} - 2P_{l}^{n+1} + P_{l-1}^{n+1})}{\Delta x^{2}} \left[(i-l+1)^{2-(1+\beta)} - (i-l)^{2-(1+\beta)} \right] \Delta x^{2-(1+\beta)}$$

$$= \frac{1}{\Gamma(3-(1+\beta))} \frac{1}{\Delta x^{1+\beta}} \sum_{l=1}^{i} (P_{l+1}^{n+1} - 2P_{l}^{n+1} + P_{l-1}^{n+1}) \left[(i-l+1)^{2-(1+\beta)} - (i-l)^{2-(1+\beta)} \right]$$

Or after shifting indices, the left sided Caputo approximation in space becomes:

$${}^{C}D_{x+}^{1+\beta} = \sigma_{\beta,\Delta x} \sum_{l=1}^{i} \omega_{l}^{(1+\beta)} (P_{i+2-l}^{n+1} - 2P_{i+1-l}^{n+1} + P_{i-l}^{n+1})$$
(81)

where

$$\sigma_{\beta,\Delta x} = \frac{1}{\Gamma(3 - (1 + \beta))} \frac{1}{\Delta x^{1 + \beta}} \tag{82}$$

and

$$\omega_l^{(\beta)} = l^{2-(1+\beta)} - (l-1)^{2-(1+\beta)} \tag{83}$$

In order to accommodate the no-flow boundary, when l = i:

$$(P_{i+2-l}^{n+1} - 2P_{i+1-l}^{n+1} + P_{i-l}^{n+1}) = P_2^{n+1} - P_1^{n+1}$$
(84)

Following the same logic the finite difference approximation for the right-sided Caputo derivative in space can be shown to be:

$${}^{C}D_{x-}^{1+\beta} = \sigma_{\beta,\Delta x} \sum_{l=1}^{I_{max}-i+1} \omega_{l}^{(1+\beta)} \left(P_{i-2+l,j}^{n+1} - 2P_{i-1+l,j}^{n+1} + P_{i+l,j}^{n+1} \right)$$
(85)

Finally, substituting (12) and (13) into (9), and assuming symmetric anomalous diffusion ($\theta = 1/2$) the finite difference approximation of the two-sided Caputo derivative in space becomes:

$$\frac{\partial^{1+\beta}}{\partial x^{1+\beta}} P_o(x_i, t_{n+1}) = \frac{\sigma_{\beta, \Delta x}}{2} \left\{ \sum_{l=1}^{i} \omega_l^{(1+\beta)} (P_{i+2-l}^{n+1} - 2P_{i+1-l}^{n+1} + P_{i-l}^{n+1}) + \sum_{l=1}^{l} \omega_l^{(1+\beta)} (P_{i-2+l,j}^{n+1} - 2P_{i-1+l,j}^{n+1} + P_{i+l,j}^{n+1}) \right\}$$
(86)

Two observations can be made. First, the stencil generated by the symmetric derivative leads to a fully populated $(I_{max} \times I_{max})$ iteration matrix. Second, for $\beta \to 1$, $\omega_1^{(\beta)} = 1$, $\omega_l^{(\beta)} \to 0$ for l > 1 and $\sigma_{\beta,\Delta x} \to 1/\Delta x^2$. Hence the approximation reverts back to the classic second order central difference approximation and its tri-diagonal matrix.

Implicit Finite Difference Scheme: Substituting the finite difference approximations to the time fractional derivative (Eq. 69), the time fractional integral (Eq. 75 for constant rate), and the space fractional derivative (Eq. 86) into the anomalous diffusion equation (Eq. 63), as well as multiplying both sides by the grid block volume $VR = \Delta x \Delta y \Delta z$, the following implicit scheme for the single phase, slightly compressible flow with constant "anomalous-diffusion permeability coefficient," k_{α} , is obtained:

$$T_{x} \begin{cases} \sum_{l=1}^{i} \omega_{l}^{(1+\beta)} (P_{i+2-l}^{n+1} - 2P_{i+1-l}^{n+1} + P_{i-l}^{n+1}) \\ + \sum_{l=1}^{l_{max}-i+1} \omega_{l}^{(1+\beta)} (P_{i-2+l,j}^{n+1} - 2P_{i-1+l,j}^{n+1} + P_{i+l,j}^{n+1}) \end{cases} - VR \frac{\phi c_{t}}{B_{o}} \sigma_{\alpha,\Delta t} P_{o}_{i}^{n+1}$$

$$(87)$$

$$= -\frac{Q_{o_i}}{B_o} \frac{(n\Delta t)^{1-\alpha}}{\Gamma(2-\alpha)} + VR \frac{\emptyset c_t}{B_o} \sigma_{\alpha,\Delta t} \left(-P_{o_i}^n + \sum_{l=2}^n \omega_l^{(\alpha)} (P_{o_i}^{n+2-l} - P_{o_i}^{n+1-l}) \right)$$

where

$$T_{\chi} = 0.006328 \left(\frac{k_{\alpha,\beta_{\chi}}}{B_{\rho}\mu_{\rho}}\right) VR \frac{\sigma_{\beta,\Delta\chi}}{2}$$
(88)

and

$$Q_{oi} = \hat{q}_o \Delta x \Delta y \Delta z \tag{89}$$

2.2.4. Preliminary Results

The presented finite difference scheme has been implemented in MATLAB and a sensitivity analysis has been run on α and β . For the studied example, the initial pressure was uniformly distributed and a constant production rate in form of a point sink was applied at the left end of the spatial domain.

Sensitivity on β : Figure 35 plots pressure drawdown ΔP_{well} vs. time for different values of β with constant $\alpha=1$. Hence the case $\beta=1$ corresponds to normal diffusion. For values of $\beta<1$ the pressure drawdown at the well decreases as β decreases, which confirms the expected superdiffusion as fluid from regions further away from the well contribute to the flow.

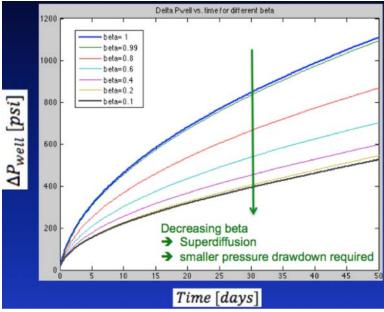


Figure 35 – Effect of β on wellbore pressure drop

The superdiffusion for β < 1 can be observed more clearly in Figure 36, which shows pressure profiles across the bounded reservoir after 50 days for different values of β . In case of normal diffusion the flow is still in transient state (the pressure disturbance reaches only 300 ft. from the well) while for β < 0.8 the pressure disturbance has already reached the boundary at 500 ft.

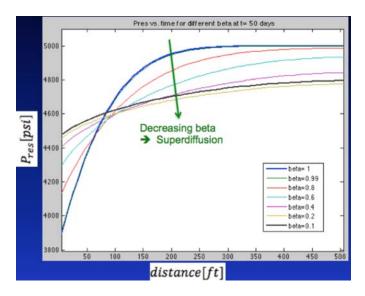


Figure 36 –Effect of β on pressure as a function of distance from the well at 50 days

Sensitivity on α : Figure 37 plots pressure drawdown ΔP_{well} vs. time for different values of α with constant $\beta=1$. Hence the case $\alpha=1$ corresponds to normal diffusion. For values of $\alpha<1$ the pressure drawdown at the well increases as α decreases, which confirms the expected subdiffusion.

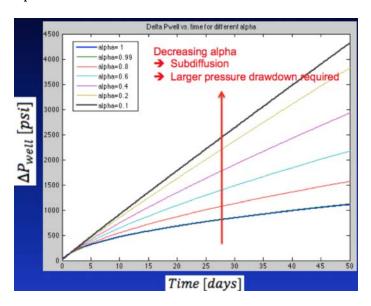


Figure 37 –Effect of α on wellbore pressure drop as a function of time for $\beta=1$

The effect of subdiffusion for $\alpha < 1$ becomes more clear in Fig. 38, which shows pressure profiles across the bounded reservoir after 50 days for different values of α and a fixed value $\beta = 1$ For $\alpha < 1$ the drainage area is smaller compared to the normal diffusion case.

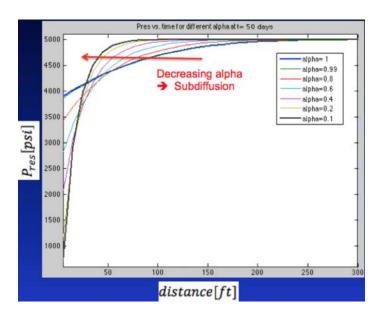


Figure 38 –Effect of α for a fixed value of $\beta=1$ on pressure as a function of distance from the well at 50 days

PROJECT 3: Production from Tight, Fractured Formations in Close Proximity of Source Rocks (Liquid-Rich Reservoirs)

Objectives: Define and model the support of source rocks on production from contiguous fractured formations for the analysis and prediction of production from liquids-rich reservoirs.

Tasks:

- Flow and transport mechanisms from source rock to producing layers (to be considered in Phase 2)
- Production models for source-rock supported liquid-rich reservoirs (to be considered in Phase 2)
- Flow characteristics and analysis of well performance (to be considered in Phase 2)

Deliverables:

- Layered reservoir model (Phase 2)
- Drainage area and well spacing considerations (Phase 2)
- Characterization and flow modeling guidelines (Phase 2)

Project 3 will be considered in Phase 2

PROJECT 4: Simulation of Flow and Transport in Fractured Nano-Porous Reservoirs

Objectives: Progressively incorporate the results of the UREP research projects and new findings into a numerical unconventional-reservoir simulator developed by NITEC.

Tasks:

- Black-oil simulator incorporating bubble-point suppression
- N-porosity simulation model

Deliverables:

- Black-oil and n-porosity simulation of liquid-rich reservoirs (Phase 1 results complete; more work in Phase 2)
- Number of pore systems from capillary pressure curvature (Phase 1 results complete; more work in Phase 2)
- Connectivity mapping of inter-porosity systems (continuing into Phase 2)
- Simulator executable, documentation, and test cases by NITEC (Phase 1 results complete; continuing into Phase 2)

Summary of Project 4 Results:

4.1. NITEC-COZSim-UREP Simulator

4.1.1 Overview – General Description of the Simulator

NITEC-COZSim-UREP is a three-phase, four-component, fully implicit, finite-difference extended black oil reservoir simulator. The simulator uses black oil type input data for fluid description and converts the data to a compositional form internally. The model can be used for variety of cases such as:

- Depletion and water flooding,
- Immiscible, first contact and multi-contact miscible CO₂ injection and cycling,
- · Hydrocarbon gas injection and cycling,
- CO₂ sequestration in aquifers and oil/gas reservoirs.
- Single and dual porosity reservoirs
- Low-permeability unconventional reservoirs

The simulator considers 3 phases (oleic, gaseous and aqueous) and consists of mass balances for four components (water, oil, hydrocarbon gas and CO_2). Components may thermodynamically partition among three phases and both hydrocarbon gas and CO_2 may partition into gaseous and aqueous phases as shown in Table 9.

Table 9 - Phases and Components in NITEC-COZSim-UREP

Component	Component		Phase	
Number		Oleic	Gaseous	Aqueous
1	Water	-	-	W_1
2	Oil	X_2	-	-
3	HC Gas	<i>X</i> 3	У 3	W3
4	CO ₂	<i>X</i> 4	<i>y</i> ₄	W_4

In addition, NITEC-COZSim-UREP can handle hydrocarbon gas and CO₂ solubility in the aqueous phase. While this may not be important in the main oil zone, it may influence the simulation results where the water saturation is high, such as in transition and residual oil zones or reservoirs under water alternating gas (WAG) injection.

Even though the data that is required to run the simulator is in black-oil format, all the information is converted to compositional form internally. Built-in correlations estimate component molecular weights, parachors, fluid properties and mole fractions based on the specific gravity of oil and hydrocarbon gas. This approach reduces the engineering time and the amount of data needed for simulation studies compared with fully compositional simulators.

Built-in CO_2 correlations are used calculate pure CO_2 properties, CO_2 solubility in the aqueous and oleic phases in the presence of hydrocarbon gas, CO_2 swelling of the oleic phase in the presence of hydrocarbon gas and phase viscosities that reflect CO_2 solubility.

Vapor-Liquid Equilibrium (Flash) calculations are performed at the bulk pressure, which is the pressure corresponding to unconfined laboratory conditions. However, the phase properties (e.g. viscosity, density) are calculated at the pressures of each phase. This requires an iterative solution of the phase properties and the capillary pressures until they converge. Confinement impact on phase behavior of black-oil fluids (bubble point pressure suppression) is accounted in the simulator.

Miscibility calculations are based on interfacial tension using black-oil data. Interfacial tension reduction due to partitioning of CO_2 in the oleic and gaseous phases is calculated using parachors; it is also used to simulate transition from immiscible to partially miscible, and finally to fully miscible conditions. Viscous fingering is handled

through a Todd-Longstaff type viscosity model using interfacial tension rather than using a constant mixing parameter. Residual oil saturation can be modeled under fully or partial miscibility conditions. The impact of both full and partial miscibility on gas-oil capillary pressure and relative permeability is accounted with fully implicit formulation.

NITEC-COZSim-UREP treats wells in fully implicit manner and it is able to simulate well and field constraints. Well modeling includes:

- Rate and BHP constrains for production and injection wells
- Wellbore cross-flow
- Well actions (workover and shut-in) based on the well limits
- Field constraints for production, injection and re-cycling

NITEC-COZSim-UREP uses three dimensional corner-point geometry grid with Cartesian coordinates, and it is able to handle faults (limited to vertical in COZView). Required non-neighbor connections are generated automatically. Regions can be defined for initialization, rock and fluid properties.

4.1.2. Mathematical Formulation and Solution Method

The formulation consists of 4 coupled mass balance (continuum) equations for each cell. The molar continuity equation for any component c is:

$$\nabla \left(\rho \vec{v} w_c\right)_a + \nabla \left(\rho \vec{v} x_c\right)_o + \nabla \left(\rho \vec{v} y_c\right)_g - q_c = \frac{\partial \left(\phi z_c \rho_t\right)}{\partial t}$$
(90)

where subscripts a, o and g denote the phases – aqueous, oleic and gaseous phase, respectively, and ρ_t is molar density of a phase. z_c is the overall mole fraction of component c. w, x and y are the mole fractions of the component in the aqueous, oleic and gaseous phases, respectively. The right hand side of the equation represents accumulation terms and left hand side is the total contribution from inter-block flow terms and source or sink. q is the molar rate and \vec{v} is the directional Darcy velocity. It is defined as:

$$v = kk_r \lambda (\nabla P - \gamma \nabla D) \tag{91}$$

The non-linear continuum equation is discretized in time and space by using standard finite-difference calculations. Time indexing of variables are all fully implicit. Four

independent variables, bulk pressure and overall mole fractions of water, hydrocarbon gas and CO_2 , are solved in fully implicit manner. The aqueous phase is treated in the same way as the other phases in terms of the continuity equation.

In order to solve the non-linear continuum equation, all terms are converted into linear form of the primary variables. Time difference formulation of accumulation terms can be expanded as following for grid block *i*:

$$\frac{\partial \left(\phi z_{c} \rho_{t}\right)}{\partial t} = \frac{1}{\Delta t} \left[\left(\phi z_{c} \rho_{t}\right)^{n+1} - \left(\phi z_{c} \rho_{t}\right)^{n} \right]_{t} \tag{92}$$

where subscript n represents the time level and the parameter value at nth time level is known (old time level) whereas n+1 denotes next time step which is unknown. Since all parameters are linearized with the primary variables, the next time step can be approximated with Taylor series expansion as following:

$$\left(\phi z_{c} \rho_{t}\right)_{i}^{n+1} \approx \left(\phi z_{c} \rho_{t}\right)_{i}^{l+1} = \left(\phi z_{c} \rho_{t}\right)_{i}^{l} + \sum_{j=1}^{4} \left[\frac{\partial \left(\phi z_{c} \rho_{t}\right)}{\partial X_{j}}\right]_{i}^{l} \partial X_{j}^{l+1}$$

$$(93)$$

Here ∂X_j denotes the primary variables as ∂P_{bulk} , ∂z_1 , ∂z_3 and ∂z_4 , bulk pressure and overall mole fractions of water, hydrocarbon gas and CO₂ components, respectively. Superscript l is the iteration number. Iteration *I* represents known parameter value and I+1 is unknown as following:

$$\partial X^{l+1} = X^{l+1} - X^l \tag{94}$$

Note that the simulator uses overall mole fractions as primary variables instead of component mole fractions, which reduces the number of independent parameters to be solved and requires a special vapor-liquid equilibrium (flash) algorithm. In addition, NITEC-COZSim-UREP does not use water saturation as a primary variable. Water saturation cannot be a truly independent variable in CO_2 displacement cases because CO_2 solubility impacts water saturation. Simulators that use water saturation as an independent variable may have difficulty addressing the impact of CO_2 solubility variations in the aqueous phase.

Similar to accumulation term, inter-block flow terms are expanded in fully implicit manner and Taylor series expansion is also used. As a result of this linearization procedure, a set of linear equations are solved using a linear solver. NITEC-COZSim-UREP uses HYPRE linear solver(Todd and Longstaff, 1972) from Lawrence Livermore National Laboratory. A simplified demonstration of solution matrix is shown below.

$$\begin{bmatrix} E_1 & F_1 & 0 & G_1 & 0 & 0 & H_1 & 0 & 0 \\ D_2 & E_2 & F_2 & 0 & G_2 & 0 & 0 & H_2 & 0 \\ 0 & D_3 & E_3 & F_3 & 0 & G_3 & 0 & 0 & H_3 \\ C_4 & 0 & D_4 & E_4 & F_4 & 0 & G_4 & 0 & 0 \\ 0 & C_5 & 0 & D_5 & E_5 & F_5 & 0 & G_5 & 0 \\ 0 & 0 & C_6 & 0 & D_6 & E_6 & F_6 & 0 & G_6 \\ B_7 & 0 & 0 & C_7 & 0 & D_7 & E_7 & F_7 & 0 \\ 0 & B_8 & 0 & 0 & C_8 & 0 & D_8 & E_8 & F_8 \\ 0 & 0 & B_9 & 0 & 0 & C_9 & 0 & D_9 & E_9 \end{bmatrix} \begin{bmatrix} \partial X_{1,1,1} \\ \partial X_{2,1,1} \\ \partial X_{3,1,1} \\ \partial X_{3,1,1} \\ \partial X_{3,2,1} \\ \partial X_{3,2,1} \\ \partial X_{2,1,2} \\ \partial X_{3,1,2} \end{bmatrix}$$

Each element in the left hand side of the Jacobian matrix represents a 4x4 coupled matrix, where F and D represent the flow in the X direction; G and G represent the flow in the Y direction; and G and G represents the flow in the G direction. Each G is a 4x1 coupled matrix, representing the residual or result vector. G is a 4x1 primary variable

vector, representing
$$\begin{bmatrix} \partial P_{bulk} & \partial z_1 & \partial z_3 & \partial z_4 \end{bmatrix}^T$$
.

Bulk pressure ($P_{\it bulk}$), which is the pressure corresponding to unconfined laboratory conditions, is one of the solution variables solved from the discretization of the continuum equations. Flash calculations are performed at the bulk pressure, which is obtained from the solution of non-linear conservation equations.

The commonly used simulators evaluate the fluid properties of oil and gas phases at a single pressure, while disregarding the phase pressure difference due to capillary pressure observed in confinement. This impacts the evaluation of fluid properties such as solution-gas-oil ratio (R_s), formation volume factor (B_o), viscosity (μ), etc. NITEC-COZSim-UREP calculates phase properties, such as density and viscosity, at the corresponding pressures of each phase. This procedure requires an iterative solution of the phase properties and the capillary pressures until they converge. Estimated capillary pressure values are used to calculate mole fractions, phase properties and saturations. Then these calculated saturations are used to calculate capillary pressures using the capillary pressure curves. This loop will go on until the solution converges to a tolerance value. A simplified flow diagram of the iterative solution technique is given in Fig. 39 and the general flow chart of the simulator modules is shown in Fig. 40.

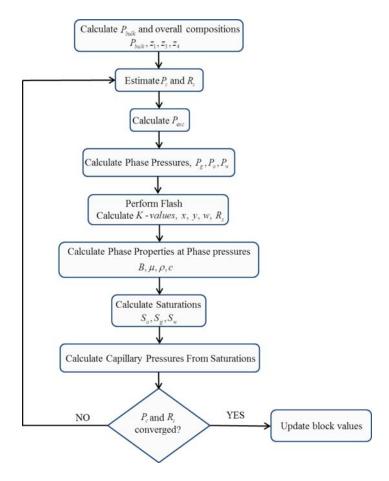


Figure 39 - Iterative Solution Technique of NITEC-COZSim-UREP

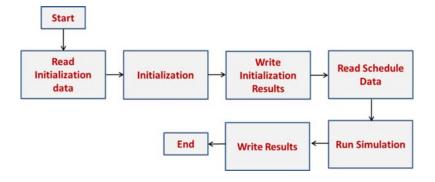


Figure 40 - General Flow Chart of Simulator Modules

Figure 41 shows the general flow diagram of the simulation module. First item in the flow chart includes the iterative procedure given in Fig. 39 to calculate block properties. Convergence criteria include pressure, overall mole fractions and material balance along with the convergence criteria of the linear solver. NITEC-COZSim-UREP calculates

time-step sizes automatically with an algorithm based on the convergence of previous time step. Maximum and minimum time step sizes can be specified by user.

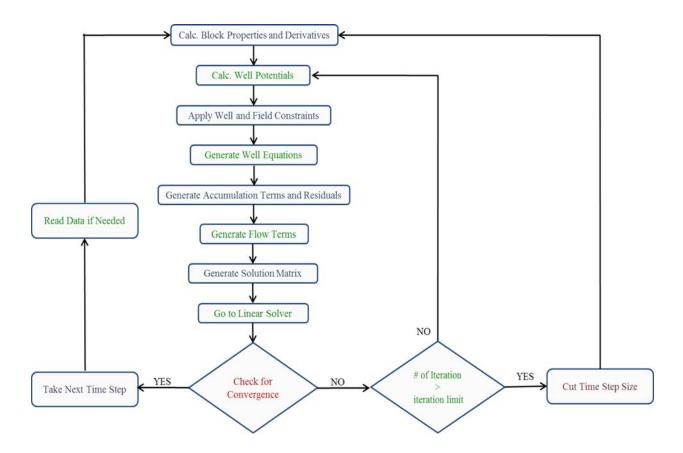


Figure 41 - General Flow Diagram for Simulation Module

4.1.3. Initialization

NITEC-COZSim-UREP uses vertical capillary-gravity equilibrium to calculate initial reservoir pressure, saturation and, composition distributions. Depth of gas-oil and water oil contacts can be defined by user.

Unlike the other widely-used commercial simulators, phase properties are calculated at the pressures of each phase. This method also requires an iterative solution similar to the procedure given in Fig. 39. First, initial saturations are calculated from capillary pressure curves. Using these initial saturations, capillary pressure values, fluid properties, mole fractions and saturations are updated. This iteration continues until reaching a convergence.

Figure 42 shows the hydrodynamic gravity-capillary equilibrium initialization of a 3-phase system. Phase pressures are determined using the respective phase gradients. Excess pressure calculation is also included in initialization module.

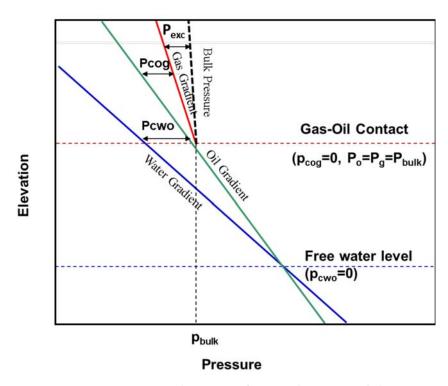


Figure 42 - Initialization of a simulation model

The simulator is able to implement multiple initializations (different initialization times) for bypassing history-matching process. This also allows initializing residual oil zones with imbibition capillary pressure curves. The determination of initial component compositions is discussed below in the PVT and Flash Calculations section.

4.1.4. PVT and Flash Calculations

The fluid data required by NITEC-COZSim-UREP is in black-oil format and it is converted to compositional form internally. This procedure consists of the calculation of overall mole fractions and mole fractions for each component. As an example, calculation of overall mole fraction of oil component from black oil data for initialization:

$$z_2 = \left(\frac{S_o}{B_o \rho_o^{sc}}\right) / \left(\frac{S_a}{B_a \rho_w^{sc}} + \frac{S_o}{B_o \rho_o^{sc}} + \frac{S_g}{B_g \rho_g^{sc}}\right)$$

$$(95)$$

Mole fraction of oil component in oleic phase:

$$x_2 = 1 / \left(1 + R_{sa} \frac{\rho_o^{sc}}{\rho_g^{sc}} \right) \tag{96}$$

NITEC-COZSim-UREP does not use fugacity constraints, equation of state based flash procedure, or table lookup *K*-values. Equilibrium *K*-values used in NITEC-COZSim-UREP are defined as:

$$K_{o,3} = \frac{y_3}{x_3}$$
 $K_{w,3} = \frac{y_3}{w_3}$ $K_{o,4} = \frac{y_4}{x_4}$ $K_{w,4} = \frac{y_4}{w_4}$ (97)

K-values are calculated internally using solution gas-oil ratio, solution gas-water ratio and molar density of the phases. The following is an example calculation of equilibrium *K*-values for the oleic phase with hydrocarbon gas.

$$K_{o,3} = \frac{1 + R_{so,3}^m}{R_{so,3}^m} \tag{98}$$

where

$$R_{so,3}^{m} = R_{so,3} \frac{\rho_o^{sc}}{\rho_g^{sc}} \tag{99}$$

 $R_{so,3}$ is solution hydrocarbon gas – oil ratio; ρ_o^{sc} and ρ_g^{sc} densities of oleic and gaseous phase pressures at standard pressure and temperature conditions, respectively. $R_{so,3}^m$ is molar solution gas – oil ratio. K-values are calculated using the R_s tables calculated with built-in correlations (Todd and Longstaff, 1972) and it is able to model variable saturation pressure cases.

4.1.5. Built-in Correlations

The most important mechanisms of a CO_2 -oil displacement process are the oil viscosity reduction and the oil swelling which are results of CO_2 solubility in oil. Therefore, it is important to calculate CO_2 solubility effects in the simulation model. CO_2 – oil solubility, oil swelling factor and CO_2 -oil mixture viscosity is calculated using genetic algorithm-based correlations (Hassanzadeh et al., 2008). This model is a generalized approach and gives more accurate predictions than conventional correlations which are limited by data ranges and conditions. Genetic algorithm-based correlations are universal and can be used to predict the effect of CO_2 for both dead oil and live oil properties. Table 10 gives the solubility related parameters and input variables that are used to calculate those parameters.

Table 10 - Parameters and Variables related to CO₂ solubility

Parameter	Input Variables
CO ₂ Solubility	Saturation Pressure, Temperature, Oil Gravity, Oil Molecular Weight, CO ₂ Liquefaction Pressure
CO ₂ -Oil Mixture Viscosity	Initial Oil Viscosity, CO ₂ Solubility, Saturation Pressure, Temperature, Oil Specific Gravity
Oil Swelling Factor	Oil Molecular Size, CO ₂ Solubility

Water

hydrocarbon gas solubility (Culberson et al., 1950), water – hydrocarbon gas solubility salinity correction (Culberson et al., 1950), water formation volume factor for saturated conditions (Culberson et al., 1950 & Dodson and Standing, 1944) is calculated with built-in correlations. Density, z factor and viscosity of pure CO_2 are also calculated internally (Hassanzadeh et al., 2008).

COZView/NITEC-COZSim-UREP uses Corey-type two-phase imbibition and drainage relative permeability curves. Modified Stone's second method(Todd and Longstaff, 1972) is used for 3-phase oil permeability model. Modified Stone's second method version in NITEC-COZSim-UREP is defined as:

$$k_{ro} = k_{rocw} \left[\left(\frac{k_{row}}{k_{rocw}} + k_{rw} \right) \left(\frac{k_{rog}}{k_{rocw}} + k_{rg} \right) - k_{rw} - k_{rg} \right]$$
(100)

where k_{rog} is oil relative permeability for an oil, gas and connate water system, k_{row} is oil relative permeability for a system with oil and water only.

4.1.6. Bubble Point Suppression and Excess Pressure Calculations

At the nano-pore scale, capillary forces play an important role on phase behavior that is not considered in conventional PVT studies. Confinement on phase behavior of black-oil fluids manifests itself as bubble point pressure suppression, extension of the undersaturated portion of the formation volume factor curve, and alteration of the equilibrium gas composition. It has been shown that when there is a pressure difference between the liquid and gas phases, the vapor liquid equilibrium shifts and the bubble point is suppressed compared to the bubble point pressure calculated by

assuming a single system pressure (Todd and Longstaff, 1972 & Vazquez and Beggs, 1980). This shift is larger than the phase pressure difference (due to capillary and surface forces) and the additional suppression amount is called excess suppression.

The correlation was developed through analyses of three unconventional oil samples evaluated at different saturation pressures and compositions. Excess suppression ratio correlation¹² is defined as:

$$\frac{P_{excess}}{P_{total}} = -2.1 \times 10^{-7} R_s^2 + 0.0009 R_s - 0.1022$$
 (101)

where P_{excess} is excess suppression and P_{total} is total suppression and it is defined as

$$P_{total} = P_{excess} + P_c \tag{102}$$

The excess suppression ratio correlation is included to NITEC-COZSim-UREP as a builtin correlation. For the flow simulation, the bulk pressure is one of the solution variables obtained from the discretization of the continuum equations (see Mathematical Formulation and Solution). The excess suppression ratio correlation relates the bulk pressure to gas pressure as a function of gas-oil capillary pressure and the R_s at bulk pressure. The capillary pressures are then used to determine the remaining phase pressures. This solution enables us to model the possible impact of confined phase behavior on flow by incorporating gas-oil capillary pressure to fluid property calculations.

For detailed information about the excess pressure and bubble point suppression, please see Refs. Lasater (1958) and Warren and Root (1963).

4.1.7. Miscibility and Viscous Fingering

Miscible flooding may create an unstable frontal advance due to viscous fingering or gravity over-riding because of the unfavorable viscosity and density ratio between the solvent (CO_2) and the oil. Accurate characterization of displacement processes requires describing unstable flood front formed by physical dispersion. Simulators which assume that solvent and oil are completely mixed within a grid block such as compositional simulators, give optimistic displacement results for coarsely gridded models. Using finely gridded models may provide more realistic results; on the other hand, it may be impractical for modeling full-scale miscible flooding projects.

If the CO_2 displaced zone is large with respect to grid size block, oil and solvent can be treated as completely mixed in the grid block. If the CO_2 displaced zone is very small

with respect to size of grid block, oil and solvent can be considered completely segregated as pure components and no mixing occurs. Generally, the actual fluid behavior is somewhere between the two mixing limits, which correspond to partial mixing. Todd and Longstaff (1972) proposed an empirical model to include viscous fingering effects for coarsely gridded models assuming partial mixing of solvent and oil. The Todd and Longstaff model is based on modification of classical black oil type properties such as relative permeabilities, densities and viscosities with a constant user-defined mixing parameter.

NITEC-COZSim-UREP uses a viscous fingering model based on the interfacial tension function rather than using a constant mixing parameter proposed by Todd-Longstaff. Effective viscosities of the oil and solvent system are calculated from their immiscible viscosity values as following:

$$\mu_{oe} = \mu_o^{1 - f(\sigma)} \mu_m^{f(\sigma)} \tag{103}$$

and

$$\mu_{se} = \mu_s^{1-f(\sigma)} \mu_m^{f(\sigma)} \tag{104}$$

where

$$\mu_{m} = \mu_{o} \mu_{s} / \left(\frac{S_{g} \mu_{o}^{1/4} + S_{o} \mu_{s}^{1/4}}{S_{o} + S_{g}} \right)^{4}$$
(105)

where μ_m is viscosity of the mixture and $f(\sigma)$ is the mixing parameter function. $f(\sigma)$ represents a channeling function to impose partial or full mixing within a grid. It is calculated internally. $f(\sigma)$ is a function of pressure, molar densities, parachors and mole fraction of components. A value of $f(\sigma)=1$ corresponds to full mixing of solvent and oil within a grid block and it results a piston like displacement. $f(\sigma)=0$ corresponds to negligible mixing or negligible dispersion similar to immiscible displacement. Partial mixing is represented by values of $0 < f(\sigma) < 1$. In this case, effective viscosity of the solvent will be less than the effective viscosity of oil, hence, solvent will travel faster than oil and create viscous fingers.

NITEC-COZSim-UREP predicts miscibility using interfacial tension based on Macleod-Sugden(Vazquez and Beggs, 1980) correlation between the two phases. The interfacial tension between the oil and gas phases is used to measure how miscible the two fluids are. Miscibility occurs when the interfacial tension between the two phases drops to zero. Relative permeabilities and capillary pressures are interpolated as functions of

interfacial tension between immiscible and miscible values. The Macleod-Sugden correlation is used to calculate interfacial tension as following:

$$\sigma = \left[\sum_{i=1}^{4} P_i \left(\rho_o x_i - \rho_g y_i\right)\right]^4 \tag{106}$$

where x_i and y_i are the liquid and gas mole fractions, ρ_o and ρ_g oleic and gaseous phase molar densities and P_i is the parachors of the i th component. Parachor value for oil component is calculated from:

$$P_2 = 18.824 + 3.0453 MW_C \tag{107}$$

where $MW_{C_{S+}}$ is C5+ oil molecular weight and it is estimated from the API value of oil by using Lasater correlation(Vazquez and Beggs, 1980):

$$MW_{C_{5+}} = \left(\frac{7864.9}{API}\right)^{1/1.0386} \tag{108}$$

Gas parachor value:

$$P_3 = 18.824 + 3.0453 \times MW_{g} \tag{109}$$

where gas molecular weight:

$$MW_g = SG_g \times \rho_{air}^{sc} \times \rho_g^{sc} \tag{110}$$

4.1.8. Dual Porosity Modeling

Dual porosity is defined as discrete matrix blocks in the continuous fracture network formed by intersecting horizontal and vertical fractures (Vazquez and Beggs, 1980). Since matrix blocks are only connected through the fracture system, fluid flows through the fracture network.

Primary variables are solved for only fractures. After fracture continuity equation is solved, matrix equation is solved explicitly. Flow rate from matrix to fracture for any phase β can be defined as:

$$q_{ex,\beta} = T_{ex} \lambda_{\beta} \left(P_{m,\beta} - P_{f,\beta} \right) \tag{111}$$

where λ is the phase mobility and P_m and P_f are the pressures in matrix and fracture, respectively. Matrix-fracture exchange transmissibility for grid block with a bulk volume $\Delta x \Delta y \Delta z$:

$$T_{ex} = 4.50844 \times 10^{-3} \times \Delta x \Delta y \Delta z \left(\frac{k_x}{L_x^2} + \frac{k_y}{L_y^2} + \frac{k_z}{L_z^2} \right)$$
 (112)

where k_x , k_y and k_z are matrix permeabilities, L_x , L_y , and L_z are fracture spacing in the x, y, and z direction respectively. Matrix fracture exchange transmissibility can be specified by user or internally calculated if fracture spacing values are assigned. Analogous to cell-to-cell transmissibility, fracture exchange transmissibility is the main parameter that controls the flow rate

Dual porosity option in NITEC-COZSim-UREP is able to model recovery mechanisms such as gravity imbibition/drainage, molecular diffusion (Todd and Longstaff, 1972), fluid expansion, and viscous displacement.

Notes on dual porosity option:

- Well completions connect only with the fracture system.
- Inter-block transmissibility calculations are determined in the same manner with single-porosity model.
- Molecular Diffusion driven by concentration gradient can be modeled with liquid-liquid, gas-gas and cross-phase diffusion.

4.1.9. N-Porosity Modeling

The N-porosity modeling is in progress. The algorithm to divide the model into n-porosity bins based on capillary pressure has been developed. The capillary pressure, relative permeability curves and permeability values for each bin based on the total average property values are also calculated.

4.1.10. Initial Composition Distribution and Filtration

One of the objectives of NITEC-COZSim-UREP was to incorporate complexities due to nano- pores present in this medium. Compositional variation due to nano-filtration is one of those complexities. Geren et al. (2014) showed that it is possible to have different compositions in different pores in thermodynamic equilibrium due to the filtration of bigger molecules through the small pore throats. Based on Geren et al.'s work the initial compositional distribution of the fluid in different pores with their corresponding equilibrium pressure (filtration pressure) will be included in the simulation model soon.

PROJECT 5: Analysis and Prediction of Well Performance in Unconventional Reservoirs

Objectives: Develop and improve models and interpretation methods for pressureand rate-transient data and long-term production performance to help reservoir management.

Tasks:

- PTA and RTA in unconventional reservoirs (partial results available; continuing into Phase 2)
- Interference models for wells in unconventional reservoirs (partial results available; continuing into Phase 2)
- Decline-curve-analysis methods for unconventional reservoirs (to be started in Phase 2)

Deliverables:

- Improved models of PTA RTA in unconventional reservoirs (partial results being delivered; more work in Phase 2)
- Analysis and interpretation guidelines (partial results being delivered; more work in Phase 2)
- Interference analysis for fractured unconventional reservoirs (partial results being delivered; more work in Phase 2)
- Improved decline-curve analysis techniques (to be considered in Phase 2)

Summary of Project 5 Results:

5.1. A New Superposition-Time for the Analysis of Unconventional Gas-Well-Test Data with Pressure Dependent Viscosity-Compressibility Product

5.1.1. Overview

In order to produce tight, unconventional gas wells economically, thousands of psi pressure drops are required. Under these conditions, the gas compressibility-viscosity product may exhibit variations 3 to 10 times greater than the initial values in the vicinity of the fracture and have a significant impact on the observed rate-time behavior. Consequently, pressure- and rate-transient analysis solutions and procedures in terms of gas pseudopressure, which assume negligible variation of the viscosity-compressibility product, yield lower than expected permeability values.

Because the source of the problem is the strong pressure dependency of the viscosity-compressibility product at low pressures, obtaining more rigorous analytical or semianalytical solutions of the nonlinear gas-flow equation is a key objective of this project. Here, we consider the linear-flow solution for an infinite-conductivity hydraulic

fracture. The conventional solution for this problem by assuming constant viscosity-compressibility product is given by

$$\frac{\Delta m_{wf}(t)}{q(t)} = \frac{2844T\sqrt{\pi\eta_i}}{2x_f kh} \left[\frac{q_1}{q(t)} \sqrt{t} + \sum_{i=1}^n \frac{(q_{i+1} - q_i)}{q(t)} \sqrt{t - t_i} \right]$$
(113)

where

$$\eta_i = \frac{2.637 \times 10^{-4} k}{\phi(\mu c_t)_i} \tag{114}$$

Based on Eq. 113, rate-normalized pseudopressure drop vs. superposition time defined by

$$t_{\text{superposition}} = \frac{q_1}{q(t)} \sqrt{t} + \sum_{i=1}^{n} \frac{\left(q_{i+1} - q_i\right)}{q(t)} \sqrt{t - t_i}$$
(115)

is expected to yield a straight line with slope

$$m = \frac{2844T\sqrt{\pi\eta_i}}{2x_i kh},\tag{116}$$

which can be used to compute $\sqrt{k}x_f$. In this project, a new solution is derived to account for the variation of viscosity-compressibility product by using a perturbation approach. The new solution leads to the definition of a new superposition time. The new solution and the superposition time will be used to develop a new regression analysis procedure.

5.1.2. Solution of the Non-Linear Diffusion Equation

The diffusion equation in terms of pseudopressure is given by:

$$\frac{\partial^2 \Delta m}{\partial y^2} = \left(1 + \omega\right) \frac{1}{\eta_i} \frac{\partial \Delta m}{\partial t} \tag{117}$$

where

$$\omega = \omega(y, t) = \frac{\eta_i - \eta}{\eta} = \frac{(\phi \mu c)_i - (\phi \mu c)}{(\phi \mu c)}$$
(118)

and

$$\eta = \frac{2.637 \times 10^{-4} \, k}{\phi \mu c} \tag{119}$$

The initial and boundary conditions are given by

$$\Delta m(y,t\to 0) = 0 \tag{120}$$

$$\Delta m(y \to \infty, t) = 0 \tag{121}$$

and

$$\frac{\partial \Delta m}{\partial y} \left(y = 0, t \right) = -\frac{2844\pi qT}{2khx_f} \tag{122}$$

Let us express Eq. 117 as a perturbation equation:

$$\frac{\partial^2 \Delta m}{\partial y^2} = \left(1 + \varepsilon \omega\right) \frac{1}{\eta_i} \frac{\partial \Delta m}{\partial t} \tag{123}$$

where

$$\varepsilon = \begin{cases} 0 & \text{Linear} \\ 1 & \text{Non-Linear} \end{cases}$$
 (124)

The solution of Eq. 123 can be assumed in the following form:

$$\Delta m = \Delta m^0 + \sum_{k=1}^{\infty} \varepsilon^k \Delta m^k \tag{125}$$

Substituting Eq. 125 into Eq. 123, we obtain

$$\left(\frac{\partial^{2} \Delta m^{0}}{\partial y^{2}} - \frac{1}{\eta_{i}} \frac{\partial \Delta m^{0}}{\partial t}\right) + \varepsilon \left(\frac{\partial^{2} \Delta m^{1}}{\partial y^{2}} - \frac{1}{\eta_{i}} \frac{\partial \Delta m^{1}}{\partial t} - \frac{\omega^{0}}{\eta_{i}} \frac{\partial \Delta m^{0}}{\partial t}\right) + \varepsilon^{2} \left(\frac{\partial^{2} \Delta m^{2}}{\partial y^{2}} - \frac{1}{\eta_{i}} \frac{\partial \Delta m^{2}}{\partial t} - \frac{\omega^{1}}{\eta_{i}} \frac{\partial \Delta m^{1}}{\partial t}\right) + \dots = 0$$
(126)

Eq. 126 suggests that Δm^0 , Δm^1 , Δm^2 , ..., are the solutions of

$$\frac{\partial^{2} \Delta m^{0}}{\partial y^{2}} - \frac{1}{\eta_{i}} \frac{\partial \Delta m^{0}}{\partial t} = 0$$

$$\frac{\partial^{2} \Delta m^{1}}{\partial y^{2}} - \frac{1}{\eta_{i}} \frac{\partial \Delta m^{1}}{\partial t} - \frac{\omega^{0}}{\eta_{i}} \frac{\partial \Delta m^{0}}{\partial t} = 0$$

$$\frac{\partial^{2} \Delta m^{2}}{\partial y^{2}} - \frac{1}{\eta_{i}} \frac{\partial \Delta m^{2}}{\partial t} - \frac{\omega^{1}}{\eta_{i}} \frac{\partial \Delta m^{1}}{\partial t} = 0$$

$$\vdots$$

$$\frac{\partial^{2} \Delta m^{k}}{\partial y^{2}} - \frac{1}{\eta_{i}} \frac{\partial \Delta m^{k}}{\partial t} - \frac{\omega^{k-1}}{\eta_{i}} \frac{\partial \Delta m^{k-1}}{\partial t} = 0$$
(127)

Consider the 0th order perturbation (the linear problem):

$$\frac{\partial^2 \Delta m^0}{\partial y^2} - \frac{1}{\eta_i} \frac{\partial \Delta m^0}{\partial t} = 0 \tag{128}$$

$$\Delta m^0 \left(y, t \to 0 \right) = 0 \tag{129}$$

$$\Delta m^0 \left(y \to \infty, t \right) = 0 \tag{130}$$

and

$$\left(\frac{\partial \Delta m^0}{\partial y}\right)_{y \in \Gamma} = -\frac{2844\pi q(t)T}{2x_f kh} = -\frac{2844\pi \tilde{q}(t)T}{k} \tag{131}$$

The Green's function solution of the linear problem (Eqs. 128-131) is given by

$$\Delta m^{0}\left(y,t\right) = \frac{2844\pi T}{k} \eta_{i} \int_{0}^{t} \tilde{q}\left(t'\right) S\left(y,t-t'\right) dt' \tag{132}$$

where

$$S = \frac{1}{2\sqrt{\pi\eta_i(t-t')}} \exp\left[-\frac{y^2}{4\eta_i(t-t')}\right]$$
(133)

so that

$$\Delta m^{0}(y,t) = \frac{1422T\sqrt{\pi\eta_{i}}}{k} \int_{0}^{t} \frac{\tilde{q}(t')}{\sqrt{t-t'}} \exp\left[-\frac{y^{2}}{4\eta_{i}(t-t')}\right] dt'$$
(134)

If $\tilde{q} = \text{constant} = q/(2x_f h)$, then

$$\Delta m^{0}(y,t) = \frac{1422qT\sqrt{\pi\eta_{i}}}{2x_{f}kh}\eta_{i}\int_{0}^{t}\frac{1}{\sqrt{(t-t')}}\exp\left[-\frac{y^{2}}{4\eta_{i}(t-t')}\right]dt'$$

$$= \frac{1422qT}{kh}\left[\sqrt{\frac{\pi\eta_{i}t}{x_{f}^{2}}}\exp\left(-\frac{y^{2}}{4\eta_{i}t}\right) - \frac{\pi y}{2x_{f}}\operatorname{erfc}\left(\frac{y}{2\sqrt{\eta_{i}t}}\right)\right]$$
(135)

Let us now consider the 1st order perturbation:

$$\frac{\partial^2 \Delta m^1}{\partial y^2} - \frac{1}{\eta_i} \frac{\partial \Delta m^1}{\partial t} - \frac{\omega^0}{\eta_i} \frac{\partial \Delta m^0}{\partial t} = 0$$
 (136)

$$\Delta m^1(y,t\to 0) = 0 \tag{137}$$

$$\Delta m^1 \left(y \to \infty, t \right) = 0 \tag{138}$$

and

$$\left(\frac{\partial \Delta m^{1}}{\partial y}\right)_{y \in \Gamma} = 0 \tag{139}$$

The Green's function solution of the problem in Eqs. 136-139 is given by

$$\Delta m^{1}(y,t) = -\eta_{i} \int_{0}^{t} \int_{0}^{\infty} \left[G\left(\frac{\partial^{2} \Delta m^{1}}{\partial y'^{2}} - \frac{\omega^{0}}{\eta_{i}} \frac{\partial \Delta m^{0}}{\partial t'}\right) - \Delta m^{1} \frac{\partial^{2} G}{\partial y'^{2}} \right] dy' dt'$$
(140)

Because, from Eq. 128

$$\frac{\partial \Delta m^0}{\partial t} = \eta_i \frac{\partial^2 \Delta m^0}{\partial v^2} \tag{141}$$

we can write Eq. 140 as

$$\Delta m^{1}(y,t) = \eta_{i} \int_{0}^{t} \int_{0}^{\infty} \left[\left(G \frac{\partial^{2} \Delta m^{1}}{\partial y'^{2}} - \Delta m^{1} \frac{\partial^{2} G}{\partial y'^{2}} \right) - G \left(\omega^{0} \frac{\partial^{2} \Delta m^{0}}{\partial y'^{2}} \right) \right] dy' dt'$$
(142)

Using Green's second identity,

$$\int_{D} (\phi \nabla^{2} \psi - \psi \nabla^{2} \phi) dD = \int_{\Gamma} (\phi \vec{\nabla} \psi - \psi \vec{\nabla} \phi) \cdot \vec{n} d\Gamma , \qquad (143)$$

Eq. 142 becomes

$$\Delta m^{1}(y,t) = -\eta_{i} \int_{0}^{t} \left[G \frac{\partial \Delta m^{1}}{\partial y} \Delta m^{1} \frac{\partial G}{\partial y} \right]_{y \in \Gamma} - \int_{0}^{\infty} G \left(\omega^{0} \frac{\partial^{2} \Delta m^{0}}{\partial y'^{2}} \right) dy' \right] dt'$$

$$= \eta_{i} \int_{0}^{t} G \left(\omega^{0} \frac{\partial^{2} \Delta m^{0}}{\partial y'^{2}} \right) dy' dt'$$
(144)

Consider

$$\frac{\partial^{2}}{\partial y^{2}} \left(\omega^{0} \Delta m^{0} \right) = \omega^{0} \frac{\partial^{2} \Delta m^{0}}{\partial y^{2}} + 2 \frac{\partial \omega^{0}}{\partial \Delta m^{0}} \left(\frac{\partial \Delta m^{0}}{\partial y} \right)^{2} + \Delta m^{0} \frac{\partial^{2} \omega^{0}}{\partial y^{2}}$$
(145)

Then, we can write Eq. 144 as follows:

$$\Delta m^{1}(y,t) = \eta_{i} \int_{0}^{t} \int_{0}^{\infty} \left[G \frac{\partial^{2}(\omega^{0} \Delta m^{0})}{\partial y'^{2}} - 2G \frac{\partial \omega^{0}}{\partial \Delta m^{0}} \left(\frac{\partial \Delta m^{0}}{\partial y} \right)^{2} - G \Delta m^{0} \frac{\partial^{2} \omega^{0}}{\partial y'^{2}} \right] dy' dt'$$

$$= \eta_{i} \int_{0}^{t} \int_{0}^{\infty} \left[G \frac{\partial^{2}(\omega^{0} \Delta m^{0})}{\partial y'^{2}} - G \Delta m^{0} \frac{\partial^{2} \omega^{0}}{\partial y'^{2}} \right] dy' dt' - 2\eta_{i} \left[\frac{\partial \omega^{0}}{\partial \Delta m^{0}} \left(\frac{\partial \Delta m^{0}}{\partial y} \right)^{2} \right]_{v,t}$$

$$(146)$$

where we have used

$$\int_{0}^{t} \int_{0}^{\infty} G(y - y', t - t') \frac{\partial \omega^{0}}{\partial \Delta m^{0}} \left(\frac{\partial \Delta m^{0}}{\partial y} \right)^{2} dy' dt' = \left[\frac{\partial \omega^{0}}{\partial \Delta m^{0}} \left(\frac{\partial \Delta m^{0}}{\partial y} \right)^{2} \right]_{y,t}$$
(147)

From Green's second identity (Eq. 143), we have

$$\int_{0}^{\infty} \left[G \frac{\partial^{2} (\omega^{0} \Delta m^{0})}{\partial y'^{2}} - (\omega^{0} \Delta m^{0}) \frac{\partial^{2} G}{\partial y'^{2}} \right] dy' = \left[S \frac{\partial (\omega^{0} \Delta m^{0})}{\partial y} - (\omega^{0} \Delta m^{0}) \frac{\partial G'}{\partial y} \right]_{y \in \Gamma}$$

$$= \left[S \left(\omega^{0} \frac{\partial \Delta m^{0}}{\partial y'} + \Delta m^{0} \frac{\partial \omega^{0}}{\partial y'} \right) \right]_{y \in \Gamma}$$

$$= \left[S \left(\omega^{0} + \frac{\partial \omega^{0}}{\partial \ln \Delta m^{0}} \right) \frac{\partial \Delta m^{0}}{\partial y'} \right]_{y \in \Gamma}$$
(148)

Using Eq. 148, we can write Eq. 146 as follows

$$\Delta m^{1}(y,t) = \eta_{i} \int_{0}^{t} \left\{ \left[S \left(\omega^{0} + \frac{\partial \omega^{0}}{\partial \ln \Delta m^{0}} \right) \frac{\partial \Delta m^{0}}{\partial y'} \right]_{y \in \Gamma} + \int_{0}^{\infty} \left[\left(\omega^{0} \Delta m^{0} \right) \frac{\partial^{2} G}{\partial y'^{2}} - G \Delta m^{0} \frac{\partial^{2} \omega^{0}}{\partial y'^{2}} \right] dy' dt' \right\} - 2 \eta_{i} \left[\frac{\partial \omega^{0}}{\partial \Delta m^{0}} \left(\frac{\partial \Delta m^{0}}{\partial y} \right)^{2} \right]_{y,t}$$

$$(149)$$

Because

$$\left(\frac{\partial \Delta m^0}{\partial y'}\right)_{y' \in \Gamma} = -\frac{2844\pi \tilde{q}(t')T}{k} \tag{150}$$

we can also write

$$\Delta m^{1}(y,t) = -\frac{2844T\pi}{k} \eta_{i} \int_{0}^{t} \left[\tilde{q}(t') \left(\omega^{0} + \frac{\partial \omega^{0}}{\partial \ln \Delta m^{0}} \right) S \right]_{y \in \Gamma}$$

$$+ \eta_{i} \int_{0}^{t} \int_{0}^{\infty} \Delta m^{0} \left(\omega^{0} \frac{\partial^{2} G}{\partial y'^{2}} - G \frac{\partial^{2} \omega^{0}}{\partial y'^{2}} \right) dy' dt' - 2 \eta_{i} \left[\frac{\partial \omega^{0}}{\partial \Delta m^{0}} \left(\frac{\partial \Delta m^{0}}{\partial y} \right)^{2} \right]_{y,t}$$

$$(151)$$

Because

$$\int_{0}^{\infty} \Delta m^{0} \left(\omega^{0} \frac{\partial^{2} G}{\partial y'^{2}} - G \frac{\partial^{2} \omega^{0}}{\partial y'^{2}} \right) dy' = \overline{\Delta m^{0}} \int_{0}^{\infty} \left(\omega^{0} \frac{\partial^{2} G}{\partial y'^{2}} - G \frac{\partial^{2} \omega^{0}}{\partial y'^{2}} \right) dy'$$

$$= \overline{\Delta m^{0}} \left(\omega^{0} \frac{\partial G}{\partial y'} - G \frac{\partial \omega^{0}}{\partial y'} \right)_{y' \in \Gamma}$$

$$= -\overline{\Delta m^{0}} \left(S \frac{\partial \omega^{0}}{\partial y'} \right)_{y' \in \Gamma}$$

$$= -\overline{\Delta m^{0}} \left(S \frac{\partial \omega^{0}}{\partial \Delta m^{0}} \frac{\partial \Delta m^{0}}{\partial y'} \right)_{y' \in \Gamma}$$

$$= \frac{2844T\pi}{k} \tilde{q}(t') \left[\left(\frac{\overline{\Delta m^{0}}}{\Delta m^{0}} \frac{\partial \omega^{0}}{\partial \ln \Delta m^{0}} \right) S \right]_{y' \in \Gamma}$$

Eq. 151 can be written as

$$\Delta m^{1}(y,t) = \frac{2844T\pi}{k} \eta_{i} \int_{0}^{t} \tilde{q}(t') \kappa^{1}(t') S(y,t-t') dt' - 2\eta_{i} \left[\frac{\partial \omega^{0}}{\partial \Delta m^{0}} \left(\frac{\partial \Delta m^{0}}{\partial y} \right)^{2} \right]_{t,t}$$
(153)

where we have defined

$$\kappa^{1}(t') = \kappa^{1}(y = 0, t') = -\left[\omega^{0} + \left(1 - \frac{\overline{\Delta m^{0}}}{\Delta m^{0}}\right) \frac{\partial \omega^{0}}{\partial \ln \Delta m^{0}}\right]$$
(154)

Now consider the 2^{nd} order perturbation:

$$\frac{\partial^2 \Delta m^2}{\partial y^2} - \frac{1}{\eta_i} \frac{\partial \Delta m^2}{\partial t} - \frac{\omega^1}{\eta_i} \frac{\partial \Delta m^1}{\partial t} = 0$$
 (155)

$$\Delta m^2 (y, t \to 0) = 0 \tag{156}$$

$$\Delta m^2 \left(y \to \infty, t \right) = 0 \tag{157}$$

and

$$\left(\frac{\partial \Delta m^2}{\partial y}\right)_{y \in \Gamma} = 0 \tag{158}$$

The Green's function solution of the problem in Eqs. 155-158 is given by

$$\Delta m^{2}(y,t) = -\eta_{i} \int_{0}^{t} \int_{0}^{\infty} \left[G\left(\frac{\partial^{2} \Delta m^{2}}{\partial y'^{2}} - \frac{\omega^{1}}{\eta_{i}} \frac{\partial \Delta m^{1}}{\partial t'}\right) - \Delta m^{2} \frac{\partial^{2} G}{\partial y'^{2}} \right] dy' dt'$$
(159)

Because, from Eq. 136

$$\frac{\partial^2 \Delta m^1}{\partial y^2} - \omega^0 \frac{\partial^2 \Delta m^0}{\partial y^2} = \frac{1}{\eta_s} \frac{\partial \Delta m^1}{\partial t}$$
 (160)

we can write Eq. 159 as

$$\Delta m^{2}(y,t) = -\eta_{i} \int_{0}^{t} \int_{0}^{\infty} \left[\left(G \frac{\partial^{2} \Delta m^{2}}{\partial y'^{2}} - \Delta m^{2} \frac{\partial^{2} G}{\partial y'^{2}} \right) - G \omega^{1} \left(\frac{\partial^{2} \Delta m^{1}}{\partial y'^{2}} - \omega^{0} \frac{\partial^{2} \Delta m^{0}}{\partial y'^{2}} \right) \right] dy' dt'$$
(161)

Using Green's second identity (Eq.143), Eq. 161 becomes

$$\Delta m^{2}(y,t) = -\eta_{i} \int_{0}^{t} \left[\left(G \frac{\partial \Delta m^{2}}{\partial y'} - \Delta m^{2} \frac{\partial G}{\partial y'} \right)_{y' \in \Gamma} - \int_{0}^{\infty} G \omega^{1} \left(\frac{\partial^{2} \Delta m^{1}}{\partial y'^{2}} - \omega^{0} \frac{\partial^{2} \Delta m^{0}}{\partial y'^{2}} \right) dy' \right] dt'$$

$$= \eta_{i} \int_{0}^{t} \int_{0}^{\infty} G \left(\omega^{1} \frac{\partial^{2} \Delta m^{1}}{\partial y'^{2}} - \omega^{1} \omega^{0} \frac{\partial^{2} \Delta m^{0}}{\partial y'^{2}} \right) dy' dt'$$
(162)

Consider

$$\frac{\partial^{2}}{\partial y^{2}} \left(\omega^{1} \Delta m^{1} \right) = \omega^{1} \frac{\partial^{2} \Delta m^{1}}{\partial y^{2}} + 2 \frac{\partial \omega^{1}}{\partial \Delta m^{1}} \left(\frac{\partial \Delta m^{1}}{\partial y} \right)^{2} + \Delta m^{1} \frac{\partial^{2} \omega^{1}}{\partial y^{2}}$$

$$(163)$$

and

$$\frac{\partial^{2}}{\partial y^{2}} \left(\omega^{1} \omega^{0} \Delta m^{0} \right) = \omega^{1} \omega^{0} \frac{\partial^{2} \Delta m^{0}}{\partial y^{2}} + 2 \omega^{1} \frac{\partial \omega^{0}}{\partial \Delta m^{0}} \left(\frac{\partial \Delta m^{0}}{\partial y} \right)^{2} + \Delta m^{0} \frac{\partial^{2} \left(\omega^{1} \omega^{0} \right)}{\partial y^{2}}$$

$$(164)$$

Then, we can write Eq. 162 as follows:

$$\Delta m^{2}(y,t) = \eta_{i} \int_{0}^{t} \int_{0}^{\infty} \left\{ G \frac{\partial^{2}(\omega^{1} \Delta m^{1})}{\partial y'^{2}} - G \Delta m^{1} \frac{\partial^{2} \omega^{1}}{\partial y'^{2}} \right\}$$

$$- \left[G \frac{\partial^{2}(\omega^{1} \omega^{0} \Delta m^{0})}{\partial y'^{2}} - G \Delta m^{0} \frac{\partial^{2}(\omega^{1} \omega^{0})}{\partial y'^{2}} \right] dy' dt'$$

$$-2 \eta_{i} \left\{ \left[\frac{\partial \omega^{1}}{\partial \Delta m^{1}} \left(\frac{\partial \Delta m^{1}}{\partial y} \right)^{2} \right]_{y,t} - \left[\omega^{1} \frac{\partial \omega^{0}}{\partial \Delta m^{0}} \left(\frac{\partial \Delta m^{0}}{\partial y} \right)^{2} \right]_{y,t} \right\}$$

$$(165)$$

where we have used

$$\int_{0}^{t} \int_{0}^{\infty} G(y - y', t - t') \frac{\partial \omega^{1}}{\partial \Delta m^{1}} \left(\frac{\partial \Delta m^{1}}{\partial y'} \right)^{2} dy' dt' = \left[\frac{\partial \omega^{1}}{\partial \Delta m^{1}} \left(\frac{\partial \Delta m^{1}}{\partial y} \right)^{2} \right]_{y,t}$$
(166)

and

$$\int_{0}^{t} \int_{0}^{\infty} G(y - y', t - t') \frac{\partial (\omega^{1} \omega^{0})}{\partial \Delta m^{0}} \left(\frac{\partial \Delta m^{0}}{\partial y'} \right)^{2} dy' dt' = \left[\omega^{1} \frac{\partial \omega^{0}}{\partial \Delta m^{0}} \left(\frac{\partial \Delta m^{0}}{\partial y} \right)^{2} \right]_{y, t}$$
(167)

From Green's second identity (Eq. 143), we have

$$\int_{0}^{\infty} \left[G \frac{\partial^{2} (\omega^{1} \Delta m^{1})}{\partial y'^{2}} - (\omega^{1} \Delta m^{1}) \frac{\partial^{2} G}{\partial y'^{2}} \right] dy' = \left[G \frac{\partial (\omega^{1} \Delta m^{1})}{\partial y'} - (\omega^{1} \Delta m^{1}) \frac{\partial G}{\partial y'} \right]_{y' \in \Gamma}$$

$$= \left[G \left(\omega^{1} + \Delta m^{1} \frac{\partial \omega^{1}}{\partial \Delta m^{1}} \right) \frac{\partial \Delta m'}{\partial y'} - (\omega^{1} \Delta m^{1}) \frac{\partial G}{\partial y'} \right]_{y' \in \Gamma} = 0$$
(168)

and

$$\int_{0}^{\infty} \left[G \frac{\partial^{2} (\omega^{1} \omega^{0} \Delta m^{0})}{\partial y'^{2}} - (\omega^{1} \omega^{0} \Delta m^{0}) \frac{\partial^{2} G}{\partial y'^{2}} \right] dy'$$

$$= \left[G \frac{\partial (\omega^{1} \omega^{0} \Delta m^{0})}{\partial y'} - (\omega^{1} \omega^{0} \Delta m^{0}) \frac{\partial G}{\partial y'} \right]_{y' \in \Gamma}$$

$$= \left[G \left(\omega^{1} \omega^{0} + \Delta m^{0} \frac{\partial \omega^{1} \omega^{0}}{\partial \Delta m^{0}} \right) \frac{\partial \Delta m^{0}}{\partial y'} - (\omega^{1} \omega^{0} \Delta m^{0}) \frac{\partial G}{\partial y'} \right]_{y' \in \Gamma}$$
(169)

that is,

$$G\frac{\partial^2 \left(\omega^1 \Delta m^1\right)}{\partial y'^2} = \omega^1 \Delta m^1 \frac{\partial^2 G}{\partial y'^2} \tag{170}$$

and

$$\int_{0}^{\infty} \left[G \frac{\partial^{2} (\omega^{1} \omega^{0} \Delta m^{0})}{\partial y'^{2}} \right] dy' = \int_{0}^{\infty} (\omega^{1} \omega^{0} \Delta m^{0}) \frac{\partial^{2} G}{\partial y'^{2}} dy' - \frac{2844 T \pi}{k} \tilde{q}(t') \left[\omega^{1} \left(\omega^{0} + \frac{\partial \omega^{0}}{\partial \ln \Delta m^{0}} \right) S \right]_{y' \in \Gamma}$$
(171)

where we have used Eq. 150. Then, Eq. 165 becomes

$$\Delta m^{2}(y,t) = \frac{2844T\pi}{k} \eta_{i} \int_{0}^{t} \tilde{q}(t') \left[\omega^{1} \left(\omega^{0} + \frac{\partial \omega^{0}}{\partial \ln \Delta m^{0}} \right) \right]_{y' \in \Gamma} S(y,t-t') dt'$$

$$+ \eta_{i} \int_{0}^{t} \int_{0}^{\infty} \left\{ \Delta m^{1} \left[\omega^{1} \frac{\partial^{2} G}{\partial y'^{2}} - G \frac{\partial^{2} \omega^{1}}{\partial y'^{2}} \right] \right.$$

$$- \Delta m^{0} \left[\left(\omega^{1} \omega^{0} \right) \frac{\partial^{2} G}{\partial y'^{2}} - G \frac{\partial^{2} \left(\omega^{1} \omega^{0} \right)}{\partial y'^{2}} \right] \right\} dy' dt'$$

$$- 2 \eta_{i} \left\{ \left[\frac{\partial \omega^{1}}{\partial \Delta m^{1}} \left(\frac{\partial \Delta m^{1}}{\partial y} \right)^{2} \right]_{y,t} - \left[\omega^{1} \frac{\partial \omega^{0}}{\partial \Delta m^{0}} \left(\frac{\partial \Delta m^{0}}{\partial y} \right)^{2} \right]_{y,t} \right\}$$

$$(172)$$

Consider

$$\int_{0}^{\infty} \Delta m^{1} \left[\omega^{1} \frac{\partial^{2} G}{\partial y'^{2}} - G \frac{\partial^{2} \omega^{1}}{\partial y'^{2}} \right] dy' = \overline{\Delta m^{1}} \int_{0}^{\infty} \left[\omega^{1} \frac{\partial^{2} G}{\partial y'^{2}} - G \frac{\partial^{2} \omega^{1}}{\partial y'^{2}} \right] dy'$$

$$= \overline{\Delta m^{1}} \left[\omega^{1} \frac{\partial G}{\partial y'} - G \frac{\partial \omega^{1}}{\partial \Delta m^{1}} \frac{\partial \Delta m^{1}}{\partial y'} \right]_{y'=\Gamma} = 0$$
(173)

and

$$\int_{0}^{\infty} \Delta m^{0} \left[\left(\omega^{1} \omega^{0} \right) \frac{\partial^{2} G}{\partial y'^{2}} - G \frac{\partial^{2} \left(\omega^{1} \omega^{0} \right)}{\partial y'^{2}} \right] dy' = \overline{\Delta m^{0}} \int_{0}^{\infty} \left[\left(\omega^{1} \omega^{0} \right) \frac{\partial^{2} G}{\partial y'^{2}} - G \frac{\partial^{2} \left(\omega^{1} \omega^{0} \right)}{\partial y'^{2}} \right] dy'$$

$$= \overline{\Delta m^{0}} \left[\left(\omega^{1} \omega^{0} \right) \frac{\partial G}{\partial y'} - S \omega^{1} \frac{\partial \omega^{0}}{\partial \Delta m^{0}} \frac{\partial \Delta m^{0}}{\partial y'} \right]_{y' \in \Gamma}$$

$$= - \left[S \omega^{1} \frac{\overline{\Delta m^{0}}}{\Delta m^{0}} \frac{\partial \omega^{0}}{\partial \ln \Delta m^{0}} \frac{\partial \Delta m^{0}}{\partial y'} \right]_{y' \in \Gamma}$$

$$= \frac{2844 \tilde{q}(t') T \pi}{k} \left[S \omega^{1} \frac{\overline{\Delta m^{0}}}{\Delta m^{0}} \frac{\partial \omega^{0}}{\partial \ln \Delta m^{0}} \right]_{y' \in \Gamma}$$
(174)

where we have used Eq. 150. Then, we can write Eq. 172 as follows:

$$\Delta m^{2}(y,t) = \frac{2844T\pi}{k} \eta_{i} \int_{0}^{t} \tilde{q}(t') \kappa^{2}(t') S(y,t-t') dt'$$

$$-2\eta_{i} \left\{ \left[\frac{\partial \omega^{1}}{\partial \Delta m^{1}} \left(\frac{\partial \Delta m^{1}}{\partial y} \right)^{2} \right]_{y,t} - \left[\omega^{1} \frac{\partial \omega^{0}}{\partial \Delta m^{0}} \left(\frac{\partial \Delta m^{0}}{\partial y} \right)^{2} \right]_{y,t} \right\}$$

$$(175)$$

where we have defined

$$\kappa^{2}(t') = \kappa^{2}(y = 0, t') = \omega^{1} \left[\omega^{0} + \left(1 - \frac{\overline{\Delta m^{0}}}{\Delta m^{0}} \right) \frac{\partial \omega^{0}}{\partial \ln \Delta m^{0}} \right]_{y=0} = -\omega^{1} \kappa^{1}(t')$$
(176)

If we now consider the k^{th} order perturbation for $k \ge 3$:

$$\frac{\partial^2 \Delta m^k}{\partial y^2} - \frac{1}{\eta_i} \frac{\partial \Delta m^k}{\partial t} - \frac{\omega^{k-1}}{\eta_i} \frac{\partial \Delta m^{k-1}}{\partial t} = 0$$
 (177)

$$\Delta m^k \left(y, t \to 0 \right) = 0 \tag{178}$$

$$\Delta m^k \left(y \to \infty, t \right) = 0 \tag{179}$$

and

$$\left(\frac{\partial \Delta m^k}{\partial y}\right)_{v \in \Gamma} = 0 \tag{180}$$

The Green's function solution of the problem in Eqs. 177-180 is given by

$$\Delta m^{k}(y,t) = -\eta_{i} \int_{0}^{t} \int_{0}^{\infty} \left[G\left(\frac{\partial^{2} \Delta m^{k}}{\partial y'^{2}} - \frac{\omega^{k-1}}{\eta_{i}} \frac{\partial \Delta m^{k-1}}{\partial t'}\right) - \Delta m^{k} \frac{\partial^{2} G}{\partial y'^{2}} \right] dy'dt'$$
(181)

Because,

$$\frac{\partial^2 \Delta m^{k-1}}{\partial y^2} - \omega^{k-2} \frac{\partial^2 \Delta m^{k-2}}{\partial y^2} = \frac{1}{\eta_i} \frac{\partial \Delta m^{k-1}}{\partial t}$$
(182)

we can write Eq. 181 as

$$\Delta m^{k}(y,t) = -\eta_{i} \int_{0}^{t} \int_{0}^{\infty} \left[\left(G \frac{\partial^{2} \Delta m^{k}}{\partial y'^{2}} - \Delta m^{k} \frac{\partial^{2} G}{\partial y'^{2}} \right) - G \omega^{k-1} \left(\frac{\partial^{2} \Delta m^{k-1}}{\partial y'^{2}} - \omega^{k-2} \frac{\partial^{2} \Delta m^{k-2}}{\partial y'^{2}} \right) \right] dy' dt'$$

$$(183)$$

Using Green's second identity (Eq. 143), Eq. 183 becomes

$$\Delta m^{k}(y,t) = -\eta_{i} \int_{0}^{t} \left[\int_{\Gamma} \left(G \frac{\partial \Delta m^{k}}{\partial y'} - \Delta m^{k} \frac{\partial G}{\partial y'} \right) d\Gamma \right] d\Gamma$$

$$- \int_{0}^{\infty} G \omega^{k-1} \left(\frac{\partial^{2} \Delta m^{k-1}}{\partial y'^{2}} - \omega^{k-2} \frac{\partial^{2} \Delta m^{k-2}}{\partial y'^{2}} \right) dy' dt'$$

$$= \eta_{i} \int_{0}^{t} \int_{0}^{\infty} G \left(\omega^{k-1} \frac{\partial^{2} \Delta m^{k-1}}{\partial y'^{2}} - \omega^{k-1} \omega^{k-2} \frac{\partial^{2} \Delta m^{k-2}}{\partial y'^{2}} \right) dy' dt'$$

$$(184)$$

Consider

$$\frac{\partial^{2}}{\partial v^{2}} \left(\omega^{k-1} \Delta m^{k-1} \right) = \omega^{k-1} \frac{\partial^{2} \Delta m^{k-1}}{\partial v^{2}} + 2 \frac{\partial \omega^{k-1}}{\partial v} \frac{\partial \Delta m^{k-1}}{\partial v} + \Delta m^{k-1} \frac{\partial^{2} \omega^{k-1}}{\partial v^{2}}$$

$$(185)$$

and

$$\frac{\partial^{2}}{\partial y^{2}} \left(\boldsymbol{\omega}^{k-1} \boldsymbol{\omega}^{k-2} \Delta m^{k-2} \right) = \boldsymbol{\omega}^{k-1} \boldsymbol{\omega}^{k-2} \frac{\partial^{2} \Delta m^{k-2}}{\partial y^{2}} + 2 \frac{\partial \left(\boldsymbol{\omega}^{k-1} \boldsymbol{\omega}^{k-2} \right)}{\partial y} \frac{\partial \Delta m^{k-2}}{\partial y} + \Delta m^{k-2} \frac{\partial^{2} \left(\boldsymbol{\omega}^{k-1} \boldsymbol{\omega}^{k-2} \right)}{\partial y^{2}} \tag{186}$$

Then, we can write Eq. 184 as follows:

$$\Delta m^{k}(y,t) = \eta_{i} \int_{0}^{t} \int_{0}^{\infty} \left\{ G \frac{\partial^{2}(\omega^{k-1}\Delta m^{k-1})}{\partial y'^{2}} - G\Delta m^{k-1} \frac{\partial^{2}\omega^{k-1}}{\partial y'^{2}} \right\}$$

$$- \left[G \frac{\partial^{2}(\omega^{k-1}\Delta m^{k-1})}{\partial y'^{2}} - G\Delta m^{k-1} \frac{\partial^{2}\omega^{k-1}}{\partial y'^{2}} \right] dy'dt'$$

$$-2\eta_{i} \left\{ \left[\frac{\partial \omega^{k-1}}{\partial \Delta m^{k-1}} \left(\frac{\partial \Delta m^{k-1}}{\partial y} \right)^{2} \right]_{y,t} - \left[\omega^{k-1} \frac{\partial \omega^{k-2}}{\partial \Delta m^{k-2}} \left(\frac{\partial \Delta m^{k-2}}{\partial y} \right)^{2} \right]_{y,t} \right\}$$

$$(187)$$

where we have used

$$\int_{0}^{t} \int_{0}^{\infty} G(y - y', t - t') \frac{\partial \omega^{k-1}}{\partial y'} \frac{\partial \Delta m^{k-1}}{\partial y'} dy' dt' = \left[\frac{\partial \omega^{k-1}}{\partial \Delta m^{k-1}} \left(\frac{\partial \Delta m^{k-1}}{\partial y} \right)^{2} \right]_{y, t}$$
(188)

and

$$\int_{0}^{t} \int_{0}^{\infty} G(y - y', t - t') \frac{\partial (\omega^{k-1} \omega^{k-2})}{\partial y} \frac{\partial \Delta m^{k-2}}{\partial y} dy' dt' = \left[\omega^{k-1} \frac{\partial \omega^{k-2}}{\Delta m^{k-2}} \left(\frac{\partial \Delta m^{k-2}}{\partial y} \right)^{2} \right]_{y,t}$$
(189)

From Green's second identity (Eq. 143), we have

$$\int_{0}^{\infty} \left[G \frac{\partial^{2} (\omega^{k-1} \Delta m^{k-1})}{\partial y'^{2}} - (\omega^{k-1} \Delta m^{k-1}) \frac{\partial^{2} G}{\partial y'^{2}} \right] dy'$$

$$= \int_{\Gamma} \left[G \frac{\partial (\omega^{k-1} \Delta m^{k-1})}{\partial y'} - (\omega^{k-1} \Delta m^{k-1}) \frac{\partial G}{\partial y'} \right] d\Gamma$$

$$= \int_{\Gamma} \left[G \left(\omega^{k-1} \frac{\partial \Delta m^{k-1}}{\partial y} + \Delta m^{k-1} \frac{\partial \omega^{k-1}}{\partial y} \right) \right] d\Gamma$$

$$= \int_{\Gamma} G \Delta m^{k-1} \frac{\partial \omega^{k-1}}{\partial y} d\Gamma = \left(\Delta m^{k-1} \frac{\partial \omega^{k-1}}{\partial y'} S \right)_{y'=0}$$

$$= \left(\Delta m^{k-1} \frac{\partial \omega^{k-1}}{\partial \Delta m^{k-1}} \frac{\partial \Delta m^{k-1}}{\partial y'} S \right)_{y'=0} = 0$$
(190)

and

$$\int_{0}^{\infty} \left[G \frac{\partial^{2} (\omega^{k-1} \omega^{k-2} \Delta m^{k-2})}{\partial y'^{2}} - (\omega^{k-1} \omega^{k-2} \Delta m^{k-2}) \frac{\partial^{2} G}{\partial y'^{2}} \right] dy'$$

$$= \int_{\Gamma} \left[G \frac{\partial (\omega^{k-1} \omega^{k-2} \Delta m^{k-2})}{\partial y'} - (\omega^{k-1} \omega^{k-2} \Delta m^{k-2}) \frac{\partial G}{\partial y'} \right] d\Gamma$$

$$= \int_{\Gamma} \left[G \frac{\partial (\omega^{k-1} \omega^{k-2} \Delta m^{k-2})}{\partial y'} \right] d\Gamma = \frac{\partial (\omega^{k-1} \omega^{k-2} \Delta m^{k-2})}{\partial y'} S$$

$$= \left[\left(\omega^{k-1} \omega^{k-2} \frac{\partial \Delta m^{k-2}}{\partial y'} + \Delta m^{k-2} \frac{\partial \omega^{k-1} \omega^{k-2}}{\partial y'} \right) S \right]_{y=0}$$

$$= \left[\left(\omega^{k-1} (\omega^{k-2} + \Delta m^{k-2} \frac{\partial \omega^{k-2}}{\partial \Delta m^{k-2}}) \frac{\partial \Delta m^{k-2}}{\partial y'} \right) S \right]_{y=0}$$

$$= 0$$

Using Eqs. 189 and 190, we can write Eq. 187 as follows

$$\Delta m^{k}(y,t) = -2\eta_{i} \left\{ \left[\frac{\partial \omega^{k-1}}{\partial \Delta m^{k-1}} \left(\frac{\partial \Delta m^{k-1}}{\partial y} \right)^{2} \right]_{y,t} - \left[\omega^{k-1} \frac{\partial \omega^{k-2}}{\partial \Delta m^{k-2}} \left(\frac{\partial \Delta m^{k-2}}{\partial y} \right)^{2} \right]_{y,t} \right\}$$
(192)

We can now summarize the solution of Eq. 127 as follows:

$$\Delta m^{0}\left(y,t\right) = \frac{2844T\pi}{k} \eta_{i} \int_{0}^{t} \tilde{q}\left(t'\right) S\left(y,t-t'\right) dt' \tag{193}$$

$$\Delta m^{1}(y,t) = \frac{2844T\pi}{k} \eta_{i} \int_{0}^{t} \tilde{q}(t') \kappa^{1}(t') S(y,t-t') dt' - 2\eta_{i} \left[\frac{\partial \omega^{1}}{\partial \Delta m^{1}} \left(\frac{\partial \Delta m^{1}}{\partial y} \right)^{2} \right]_{y,t}$$
(194)

$$\Delta m^{2}(y,t) = \frac{2844T\pi}{k} \eta_{i} \int_{0}^{t} \tilde{q}(t') \kappa^{2}(t') S(y,t-t') dt'$$

$$-2\eta_{i} \left\{ \left[\frac{\partial \omega^{1}}{\partial \Delta m^{1}} \left(\frac{\partial \Delta m^{1}}{\partial y} \right)^{2} \right]_{y,t} - \left[\omega^{1} \frac{\partial \omega^{0}}{\partial \Delta m^{0}} \left(\frac{\partial \Delta m^{0}}{\partial y} \right)^{2} \right]_{y,t} \right\}$$
(195)

:

$$\Delta m^{k}(y,t) = -2\eta_{i} \left\{ \left[\frac{\partial \omega^{k-1}}{\partial \Delta m^{k-1}} \left(\frac{\partial \Delta m^{k-1}}{\partial y} \right)^{2} \right]_{y,t} - \left[\omega^{k-1} \frac{\partial \omega^{k-2}}{\partial \Delta m^{k-2}} \left(\frac{\partial \Delta m^{k-2}}{\partial y} \right)^{2} \right]_{y,t} \right\} \quad k \ge 3$$
(196)

where

$$S = S(y, t - t') = \frac{1}{2\sqrt{\pi \eta_i(t - t')}} \exp\left[-\frac{y^2}{4\eta_i(t - t')}\right]$$
 (197)

Therefore, using Eq. 125, the solution of Eq. 123 is given by

$$\Delta m(y,t) = \Delta m^{0} + \Delta m^{1} + \Delta m^{2} + \sum_{k=3}^{\infty} \Delta m^{k}$$

$$= \frac{2844T\pi}{k} \eta_{i} \int_{0}^{t} \tilde{q}(t') \left[1 + \kappa(t') \right] S(y,t-t') dt' - 2\eta_{i} \left[\frac{\partial \omega^{1}}{\partial \Delta m^{1}} \left(\frac{\partial \Delta m^{1}}{\partial y} \right)^{2} \right]_{y,t}$$

$$-2\eta_{i} \sum_{k=2}^{\infty} \left\{ \left[\frac{\partial \omega^{k-1}}{\partial \Delta m^{k-1}} \left(\frac{\partial \Delta m^{k-1}}{\partial y} \right)^{2} \right]_{y,t} - \left[\omega^{k-1} \frac{\partial \omega^{k-2}}{\partial \Delta m^{k-2}} \left(\frac{\partial \Delta m^{k-2}}{\partial y} \right)^{2} \right]_{y,t} \right\}$$

$$(198)$$

where

$$\kappa(t) = \kappa^{1}(t) + \kappa^{2}(t) = (1 - \omega^{1})_{y=0} \kappa^{1}(t)$$

$$= \left\{ (\omega^{1} - 1) \left[\omega^{0} + \left(1 - \frac{\overline{\Delta m^{0}}}{\Delta m^{0}} \right) \frac{\partial \omega^{0}}{\partial \ln \Delta m^{0}} \right] \right\}_{y=0}$$
(199)

Consider the solution (Eq. 198) on the fracture plane (y = 0):

$$\Delta m(0,t) = \frac{2844T\pi}{k} \eta_{i} \int_{0}^{t} \tilde{q}(t') \Big[1 + \kappa(t') \Big] S(0,t-t') dt'
+2\eta_{i} \Big[\frac{\omega^{1}}{\Delta m^{0}} \frac{\partial \omega^{0}}{\partial \ln \Delta m^{0}} \Big(\frac{\partial \Delta m^{0}}{\partial y} \Big)^{2} \Big]_{0,t}
= \frac{2844T\sqrt{\pi \eta_{i}}}{2k} \int_{0}^{t} \tilde{q}(t') \Big[1 + \kappa(t') \Big] \frac{dt'}{\sqrt{(t-t')}}
+2\eta_{i} \Big(\frac{2844T\pi}{k} \Big)^{2} \Big(\frac{\omega^{1}}{\Delta m^{0}} \frac{\partial \omega^{0}}{\partial \ln \Delta m^{0}} \Big)_{0,t} \Big[\tilde{q}(t) \Big]^{2}$$
(200)

Let us consider the sequence of time $0 = t_0 < t_1 < t_2 \cdots < t_n < t_{n+1} = t$ and write Eq. 200 as

$$\Delta m(0,t) = \frac{2844T\sqrt{\pi\eta_{i}}}{2k} \sum_{i=1}^{n} \int_{t_{i}}^{t_{i+1}} \tilde{q}(t') \left[1 + \kappa(t')\right] \frac{dt'}{\sqrt{(t-t')}}$$

$$+2\eta_{i} \left(\frac{2844T\pi}{k}\right)^{2} \left(\frac{\omega^{1}}{\Delta m^{0}} \frac{\partial \omega^{0}}{\partial \ln \Delta m^{0}}\right)_{0,t} \left[\tilde{q}(t)\right]^{2}$$

$$(201)$$

For $t_i < t' < t_{i+1}$, if we approximate

$$\tilde{q}(t') \Big[1 + \kappa(t') \Big] \approx \tilde{q}(t_{i+1}) \Big[1 + \kappa(t_{i+1}) \Big] \equiv \tilde{q}_{i+1} \Big(1 + \kappa_{i+1} \Big) \equiv \frac{q_{i+1}}{2\kappa_i h} \Big(1 + \kappa_{i+1} \Big)$$
(202)

where q(t) is the flow rate from the entire surface of the fracture, Eq. 201 becomes

$$\Delta m(0,t) = \frac{2844T\sqrt{\pi\eta_{i}}}{2x_{f}kh} \sum_{i=1}^{n} q_{i+1} \left(1 + \kappa_{i+1}\right) \int_{t_{i}}^{t_{i+1}} \frac{dt'}{\sqrt{(t-t')}} + \frac{\eta_{i}}{2} \left(\frac{2844T\pi}{x_{f}kh}\right)^{2} \left(\frac{\omega^{1}}{\Delta m^{0}} \frac{\partial \omega^{0}}{\partial \ln \Delta m^{0}}\right)_{0,t} \left[q(t)\right]^{2} = \frac{2844T\sqrt{\pi\eta_{i}}}{2x_{f}kh} \sum_{i=1}^{n} q_{i+1} \left(1 + \kappa_{i+1}\right) \left(\sqrt{t-t_{i}} - \sqrt{t-t_{i+1}}\right) + \frac{\eta_{i}}{2} \left(\frac{2844T\pi}{x_{f}kh}\right)^{2} \left(\frac{\omega^{1}}{\Delta m^{0}} \frac{\partial \omega^{0}}{\partial \ln \Delta m^{0}}\right)_{0,t} \left[q(t)\right]^{2}$$

$$(203)$$

Expanding

$$\Delta m(0,t) = \frac{2844T\sqrt{\pi\eta_{i}}}{2x_{f}kh} \left[q_{1}(1+\kappa_{1})\left(\sqrt{t-t_{0}} - \sqrt{t-t_{1}}\right) + q_{2}(1+\kappa_{2})\left(\sqrt{t-t_{1}} - \sqrt{t-t_{2}}\right) + q_{3}(1+\kappa_{3})\left(\sqrt{t-t_{2}} - \sqrt{t-t_{3}}\right) \right]$$

$$\vdots$$

$$+ q_{n}(1+\kappa_{n})\left(\sqrt{t-t_{n-1}} - \sqrt{t-t_{n}}\right) + q_{n+1}(1+\kappa_{n+1})\left(\sqrt{t-t_{n}} - \sqrt{t-t_{n+1}}\right) + q_{n+1}\left(1+\kappa_{n+1}\right)\left(\sqrt{t-t_{n}} - \sqrt{t-t_{n+1}}\right) + q_{n+1}\left(\frac{2844T\pi}{x_{f}kh}\right)^{2} \left(\frac{\omega^{1}}{\Delta m^{0}} \frac{\partial \omega^{0}}{\partial \ln \Delta m^{0}}\right) \left[q(t)\right]^{2}$$

Because $t_0 = 0$ and $t_{n+1} = t$, we can rearrange Eq. 204 as follows:

$$\Delta m(0,t) = \frac{2844T\sqrt{\pi\eta_{i}}}{2x_{f}kh} \left\{ q_{1}(1+\kappa_{1})\sqrt{t} + \sum_{i=1}^{n} \left[q_{i+1}(1+\kappa_{i+1}) - q_{i}(1+\kappa_{i}) \right] \sqrt{t-t_{i}} \right\} + \frac{\eta_{i}}{2} \left(\frac{2844T\pi}{x_{f}kh} \right)^{2} \left(\frac{\omega^{1}}{\Delta m^{0}} \frac{\partial \omega^{0}}{\partial \ln \Delta m^{0}} \right)_{0,t} \left[q(t) \right]^{2}$$
(205)

Dividing by $q(t) = q(t_{n+1}) = q_{n+1}$

$$\frac{\Delta m(0,t)}{q(t)} = \frac{2844T\sqrt{\pi\eta_{i}}}{2x_{f}kh} \left\{ \frac{q_{1}}{q(t)} (1+\kappa_{1})\sqrt{t} + \sum_{i=1}^{n} \left[q_{i+1} (1+\kappa_{i+1}) - q_{i} (1+\kappa_{i}) \right] \frac{\sqrt{t-t_{i}}}{q(t)} \right\} + \frac{\eta_{i}}{2} \left(\frac{2844T\pi}{x_{f}kh} \right)^{2} \left(\frac{\omega^{1}}{\Delta m^{0}} \frac{\partial \omega^{0}}{\partial \ln \Delta m^{0}} \right)_{0,t} q(t)$$
(206)

The solution given in Eq. 206 leads to the following definition of the new superposition time, which takes into account the effect of viscosity-compressibility variation with pressure:

$$t_{\text{superposition-new}} = \frac{q_1}{q(t)} (1 + \kappa_1) \sqrt{t} + \sum_{i=1}^{n} \left[q_{i+1} (1 + \kappa_{i+1}) - q_i (1 + \kappa_i) \right] \frac{\sqrt{t - t_i}}{q(t)}$$
(207)

5.1.3. Computational Procedure

To numerically evaluate the solution in Eq. 206, we need to evaluate ω_0 and ω_1 . This requires that we compute Δm^0 and Δm^1 , convert pseudo-pressures to pressures, and evaluate ω_0 and ω_1 at these pressures. Let us first consider Δm^0 given in Eq. 193. Following the lines used in the derivation of Eq. 205, we can write

$$\Delta m^{0}(0,t) = \frac{2844T\sqrt{\pi\eta_{i}}}{2x_{f}kh} \left[q_{1}\sqrt{t} + \sum_{i=1}^{n} (q_{i+1} - q_{i})\sqrt{t - t_{i}} \right]$$
(208)

Similarly, we can write Δm^1 in Eq. 194 as follows:

$$\Delta m^{1}(0,t) = \frac{2844T\sqrt{\pi\eta_{i}}}{2x_{f}kh} \left[q_{1}\kappa_{1}^{1}\sqrt{t} + \sum_{i=1}^{n} \left(q_{i+1}\kappa_{i+1}^{1} - q_{i}\kappa_{i}^{1}\right)\sqrt{t - t_{i}} \right]$$
(209)

where

$$\kappa_{i}^{1} = \kappa^{1}(t_{i}) = -\left[\omega_{i}^{0} + \left(1 - \frac{\overline{\Delta m^{0}}}{\Delta m^{0}}\right)_{i}\left(\frac{\partial \omega^{0}}{\partial \ln \Delta m^{0}}\right)_{i}\right]$$

$$= -\left[\left(\omega^{0}\right)_{\Delta m^{0}(t_{i})} + \left(1 - \frac{\overline{\Delta m^{0}}(t_{i})}{\Delta m^{0}(t_{i})}\right)\left(\frac{\partial \omega^{0}}{\partial \ln \Delta m^{0}}\right)_{t_{i}}\right]$$
(210)

For an infinite reservoir, we can assume $\overline{\Delta m^0}(t) = \overline{\Delta m^0}(t=0) = 0$ and write Eq. 210 as follows:

$$\kappa_{i}^{1} = \kappa^{1}(t_{i}) = -\left[\omega_{i}^{0} + \left(\frac{\partial \omega^{0}}{\partial \ln \Delta m^{0}}\right)_{i}\right] = -\left[\left(\omega^{0}\right)_{\Delta m^{0}(t_{i})} + \left(\frac{\partial \omega^{0}}{\partial \ln \Delta m^{0}}\right)_{t_{i}}\right]$$
(211)

The step-by-step computational procedure is the following:

- 1. Divide the range of the pressure, $14.7 \, psi \le p \le p_i$, into K points (K = 100 is usually sufficient) and generate tables of p_k vs. m_k and p_k vs. Δm_k for k = 1, 2, ... K.
- 2. Compute $\Delta m^{0}(t_{i})$ for i = 1, 2, ..., n+1 from Eq. 208.
- 3. Convert $\Delta m^0(t_i)$ to $p^0(t_i)$ using the p_k vs. Δm_k table (use interpolation when the $\Delta m^0(t_i)$ value falls between Δm_k and Δm_{k+1}).
- 4. Compute ω_i^0 at $p^0(t_i)$ for i=1,2,...n+1 by using the correlations for the gas viscosity and compressibility.
- 5. Make a table of ω_i^0 vs. $\Delta m^0(t_i)$ and evaluate $(\partial \omega^0/\partial \ln \Delta m^0)_{t_i} = [\Delta m^0(\partial \omega^0/\partial \Delta m^0)]_{t_i}$ for i = 1, 2, ..., n+1
- 6. Using the computed values of ω_i^0 and $\left(\partial \omega^0/\partial \ln \Delta m^0\right)_{t_i}$, evaluate κ_i^1 from Eq. 211 for i=1,2,...n+1
- 7. Using κ_i^1 , compute $\Delta m^1(t_i)$ for i = 1, 2, ..., n+1 from Eq. 209.
- 8. Follow steps 3 and 4 to generate a table of ω_i^1 vs. $\Delta m^1(t_i)$.
- 9. Compute κ_i from Eq. 83 by assuming $\overline{\Delta m^0}(t) = \overline{\Delta m^0}(t=0) = 0$ as follows:

$$\kappa_{i} = \kappa \left(t_{i} \right) = \left(\omega_{i}^{1} - 1 \right) \left[\omega_{i}^{0} + \left(\frac{\partial \omega^{0}}{\partial \ln \Delta m^{0}} \right)_{i} \right] = \left(1 - \omega_{i}^{1} \right) \kappa_{i}^{1}$$
(212)

where κ_i^1 are the values computed in Step 6.

10. Using κ_i , compute $\Delta m^0(0,t)$ or $\Delta m^0(0,t)/q(t)$ from Eq. 205 or 206, respectively.

5.1.4. Analysis of Data by Regression

The new superposition-time solution can be used to analyze tight-gas well data by a regression procedure. We have tested the viability of regression analysis by using the data shown in Table 11. Figure 43 shows the rate-normalized pseudopressure drop vs. the new and the conventional superposition times.

Table 11 - Reservoir rock and fluid properties

<u> </u>	
Formation height, h (ft)	37.15
Fracture half length, x_f (ft)	100
Reservoir permeability, k (mD)	3.584 x 10 ⁻⁴
Reservoir porosity, ϕ	0.08
Reservoir length, L_e (ft)	1000
Specific gravity, SG (lb/ft³)	0.57
Initial reservoir pressure, p_i (psia)	9597
Initial reservoir temperature, T_i (F)	258

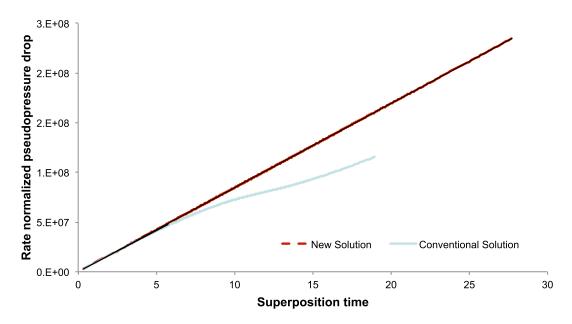


Figure 43 - Rate-normalized pseudopressure drop vs. the new and conventional superposition times

As shown in Fig. 43, the new superposition time plot yields a straight line while the conventional superposition time plot deviates from the straight line trend when time (and pressure drop) increases. To develop a regression analysis procedure, we have tested the sensitivity of the new solution to the variation of $\sqrt{k}x_f$ product as shown in Figure 44.

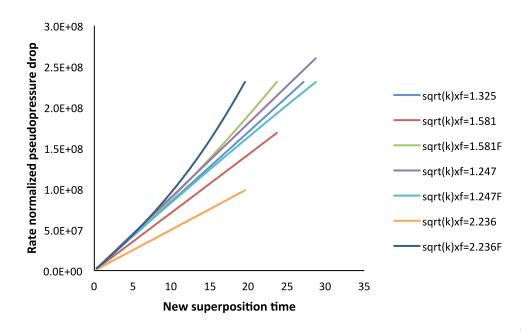


Figure 44 – Regression analysis on $\sqrt{k}x_c$ product using new solution

5.2. An Approximate Solution for Fractured Horizontal Wells in Composite Reservoirs

5.2.1. Overview

The assumption of a stimulated reservoir volume (SRV) around fractured horizontal wells leads to relatively simple transient flow models, such as the trilinear flow model (Brown, 2009), which assume that the flow beyond SRV is negligible (and predominantly linear). However much these models are useful to infer general flow characteristics of fractured horizontal wells in unconventional reservoirs, they are strictly valid when there is high contrast between the conductivities of the inner and outer reservoir sections. When the conductivity contrast is not as high and/or when there are fractures extending beyond the SRV (and potentially connecting to the SRV of the neighboring wells), these idealized models should not be used. However, generating rigorous analytical solutions for multiple-fractured horizontal wells in composite reservoirs is not an easy task and usually leads to numerically inefficient formulations.

This project aims at generating a robust and sufficiently accurate approximate analytical solution to be used in the study and the analysis of pressure-transient responses of fractured horizontal wells in composite reservoirs. The solution is intended for further extension to the study of interference effects between wells, particularly in the existence of cross-well natural fractures.

5.2.2. Description of the model and the solution procedure

The system considered in this project is shown in Fig. 44. There are two zones of different petrophysical properties. For the purposes of our investigation, the inner zone represents the SRV, which has natural fractures, and the outer zone may be homogeneous or naturally fractured. Natural fractures are accounted for by the dual-porosity idealization.

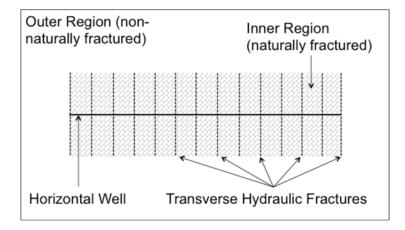


Figure 44 – Fractured horizontal well in a composite reservoir

The superposition approach used to obtain the approximate solution for a fractured horizontal well in a composite reservoir is illustrated in Fig. 45. Three solutions are used in this procedure:

- Solution I Fractured horizontal well in an infinite-acting reservoir with the properties of the virgin (unstimulated) reservoir
- Solution II Fractured horizontal well in a bounded reservoir with the size of the SRV but the properties of the virgin reservoir (no natural fractures)
- Solution III Fractured horizontal well in a bounded reservoir with the size and the petrophysical properties of the SRV.

To create composite-reservoir solution, Solution II is subtracted from and Solution III is added to Solution I. This procedure is based on the assumption that the flux distribution at the boundary of the inner reservoir is independent of the contrast between the petrophysical properties of the virgin and the stimulated reservoirs. The consequences of this assumption will have to be investigated to determine the conditions of the applicability of the solution.

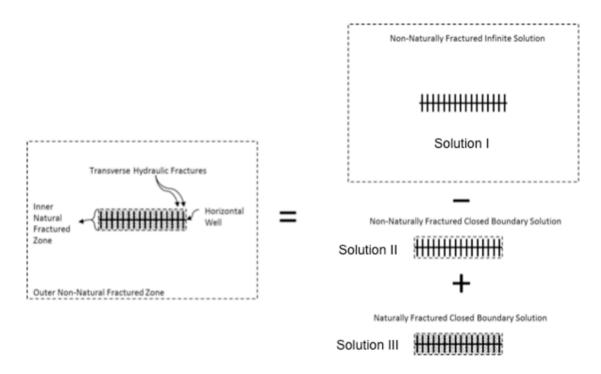


Figure 45 – Superposition of fractured horizontal well solutions to generate the composite-reservoir solution

We use the fractured horizontal well solution developed by Chen and Raghavan (1997) for Solutions I, II, and III. Chen and Raghavan derived the hydraulically fractured horizontal by solution by applying the superposition principle to the finite-conductivity fracture solution of Cinco-Ley and Meng (1988). The solution is derived analytically but the computation of the solution requires discretization of finite-conductivity hydraulic fractures. Therefore, the results are considered as semi-analytical. Furthermore, to avoid discretization in time, the solution is derived in the Laplace transform domain and the results are numerically inverted into time domain by using Stehfest (1970) algorithm. The details of the solution and the computational procedure will be given in Greenwood (2015). We note here that, especially the computation of the bounded system solution (Solutions II and III) requires high accuracy to prevent the drift of the numerical results.

Figure shows a comparison of the composite-system solution (superposition model) with the low-permeability, infinite homogeneous reservoir (virgin reservoir) and the high-permeability (twice the permeability of the virgin reservoir), SRV (bounded reservoir) solutions. As expected, the superposition solution tracks the results of the high-permeability SRV model at early times and then deviates from the SRV solution to follow the low-permeability, infinite-reservoir model.

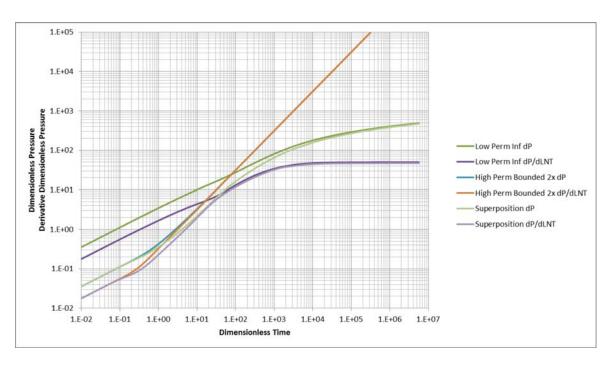


Figure 46 – Comparison of the results of the composite-reservoir (superposition) solution with those of the low-permeability infinite and high-permeability SRV models.

In Figs. 47 and 48, the composite-reservoir model is verified against a commercial numerical simulator (CMG) to find the limitations of the superposition approach used to construct the solution. For Case 1 shown in Fig. 47, the dimensions of the stimulated zone are $2x_f$ by $1x_f$. In this case, the superposition solution tracks the numerical model results perfectly for all 4 cases. On the other hand, for Case 2 shown in Fig. 48, where the size of the stimulated zone is $4x_f$ by $4x_f$, the superposition solution over-predicts pressure drop after the effect of the SRV boundary are felt. These results indicate that the accuracy of the superposition solution is dependent on the size of the stimulated zone, which affects the flux distribution at the boundary (for large stimulated zones, the flux profiles at the boundaries of the fractured and un-fractured SRV models, Solutions II and III, differ significantly). However in real-world examples of multiply fractured horizontal wells, the stimulated zone is much smaller and the superposition model predicts pressure and derivative responses within satisfactory range of the numerical simulator.

This research will continue into Phase 2 with two important objectives. First, the possibility of shifting the time to match the flux profiles of fractured and un-fractured SRV cases will be considered. Second, An additional well and cross-well, stand-alone fractures will be imposed on the solution to study the interference effects.

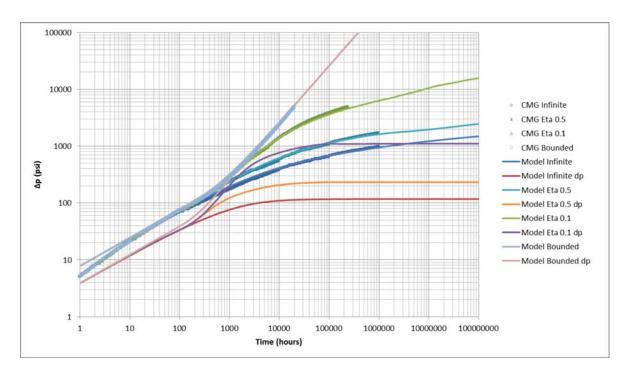


Figure 47: Case 1 in which the stimulated zone is $2x_f$ by $1x_f$. The numerical model tracks the model perfectly for all 4 cases.

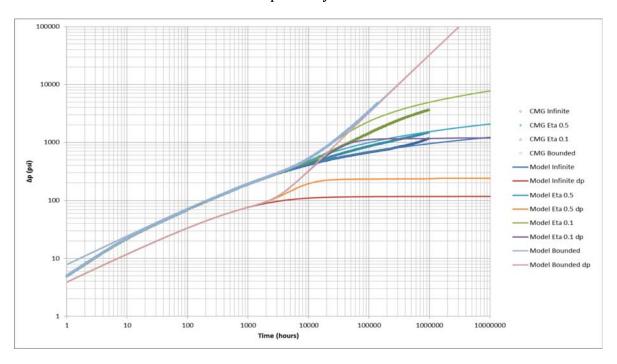


Figure 48: Case 2 in which the stimulated zone is $4x_f$ by $4x_f$. The numerical model does not match the research model after the boundary is reached. The research model overpredicts the differential pressure.

Nomenclature

Attraction parameter for cubic EOS, (m³)²/bar a Repulsion parameter for cubic EOS, m³ b *Hydraulic fracture conductivity, dimensionless* C_{FD} Reservoir conductivity, dimensionless C_{RD} Cardinal function C_k Gas compressibility, psi-1 C_{g} Rock compressibility, psi-1 C_r *Total compressibility*, psi⁻¹, bar⁻¹ c_t D : Fractal dimension d Distance between two adjacent hydraulic fractures, ft $D_{i,k}$: Chebyshev differentiation matrix Self-diffusion coefficient D_{s} : Effective self-diffusion coefficient of hindered component D_s^* d_s : Spectral coefficient d_f : Mass fractal coefficient : Fugacity, psi f G: Green function h : Reservoir thickness, ft : Fracture height, ft h_f $\vec{J_i}$: Flux of species i per unit area of flow channels : Molar diffusive flux of hindered component i : K-value Kk : Permeability, md : Permeability of the inner reservoir, md k_{I} : Natural fracture permeability, md k_f k_F : Hydraulic fracture permeability, md Permeability of the outer reservoir, md k_0 : Matrix permeability, md k_m Relative permeability of phase n k_{rn} Phenomenological coefficient of anomalous diffusion, md-day^{1- α} k_{α} Anomalous permeability, mD. $day^{1-\alpha} ft^{\beta-1}$ $\bar{\bar{k}}_{\alpha,\beta}$ Phenomenological coefficients relating ith flow to jth force L_{ij} Real gas pseudopressure, psia²/cp m(p): Pressure, bar (in Section 1.1, 1.2), pascal (in Section 1.3), psi (in Sections 1.4, 1.5) Bulk pressure, bar p_{bulk} Capillary pressure, bar p_c Bulk critical pressure, psi P_{cb} : Pore critical pressure, psi P_{cp}

: Excess suppression, bar

Excess pressure, bar

: Filtration pressure, psi

: Parachors of ith component

 p_e

 p_{exc}

 p_F

 p_i

:

 p_{min} : Minimum bottomhole pressure, psia p_{max} : Maximum bottomhole pressure, psia

 p_r : Reduced pressure

 p_{wf} : Bottomhole pressure, psia

q : Volumetric rate, stb/day (in Sections 1.5, 2.1), scf/day

q_{sf} : Sandface rate, scf/day

R: Universal gas constant (8.3144621 joule/mol°K)

R_s : Solution gas-oil ratio, scf/STB

r_b: Bubble radius, m
r_p: Pore radius, nm
r_w: Wellbore radius, ft

S : Saturation

S_{orm} : Residual oil saturation to miscible flooding

s : Laplace parameter

T : Temperature, °K(in Section 1.2), °R

 T_{cb} : Bulk critical temperature, °F T_{cp} : Pore critical temperature, °F

 T_r : Reduced temperature

t : Time, hrs, day

V : Molar volume, m³/mol
 w_F : Hydraulic fracture width, ft

 w_i : Mole fraction of i^{th} component in aqueous phase

x : Liquid mole fraction

x_e : Reservoir size, x-direction, ft
 x_F : Hydraulic fracture half-length, ft

 x_i : Mole fraction of i^{th} component in oleic phase $\overrightarrow{X_i}$: Conjugated driving force for flux of species i

y : Gas mole fraction

y_e Reservoir size, y-direction, ft

 y_i : Mole fraction of i^{th} component in gaseous phase

Z : z-factor

 z_i : Overall mole fraction of i^{th} component

Greek Symbols

 α : Order of fractional derivative of time $\alpha_{0,F}$: Parameter defined in the model

eta : Order of fractional derivative of space

 $eta_{0,F}$: Parameter defined in the model

 Δ : Difference operator

 δ_{ii} : Binary interaction parameter

 Φ : Dissipation function

φ : Porosity

 Γ : Gamma function

 γ : Lennard-Jones size parameter, nm

 γ_g : Specific gas gravity η : Diffusivity, ft^2/hr

 λ : Permeability viscosity ratio λ_{α} : Phenomenological coefficient

μ : Viscosity, cp

 μ_i : Chemical potential, joule

 π : Pi constant

 Π_s : Surface pressure, bar ρ : Molar density, gr-mol/cc ρ_g : Gas density, lbm/ft³

 σ : Interfacial tension

 au_a : Dimensionless apparent tortuosity factor

 $\omega_{\!f}$: Membrane efficiency

 ω_i : Acentric factor

References

- Acuna, J. A., Ershaghi, I., and Yortsos, Y. C., 1995. Practical Application of Fractal Pressure-transient Analysis in Naturally Fractured Reservoirs, *SPE Formation Evaluation* 10 (3): 173-179, doi: 10.2118/24705-PA.
- Albinali, A., 2014. Analytical Modeling of Fractured Nano-porous Reservoirs. A Dissertation Proposal for Doctor of Philosophy in Petroleum Engineering, Colorado School of Mines, Petroleum Engineering Department.
- Barenblatt, G.I., Zheltov, I.P., and Kochina, I.N., 1960. Basic Concepts in the Theory of Seepage of Homogeneous Liquids in Fissured Rocks. *J. Appl. Math. Mech.* **24** (5): 1286-1303.
- Beier, R. A., 1994. Pressure Transient Model for a Vertically Fractured Well in a Fractal Reservoir. *SPE Formation Evaluation* **9** (2): 122-128. SPE 20582-PA.
- Brown, M., 2009. Analytical Trilinear Pressure Transient Model for Multiply Fractured Horizontal Wells in Tight Unconventional Reservoirs. Master's Thesis. Colorado School of Mines. Golden, CO.
- Brown, M., Ozkan, E., Raghavan, R., and Kazemi, H., 2011. Practical Solutions for Pressure Transient Responses of Fractured Horizontal Wells in Unconventional Reservoirs. *SPEREE* **14** (6): 663-676.
- Brusilovsky, A. I., 1992. Mathematical Simulation of Phase Behavior of Natural Multicomponent systems at High Pressures with an Equation of State. *SPE Reservoir Engineering*, **7** (1): 117-122.
- Camacho-Velázquez, R., Fuentes-Cruz, G., Vasquez-Cruz, M., 2008. Decline-Curve Analysis of Fractured Reservoirs with Fractal Geometry. *SPE Reservoir Evaluation & Engineering*, **11** (3): 606-619.
- Caputo, M., 1967. Linear Models of Dissipation Whose Q is Almost Frequency Independent-II. *Geophys. J. Int.* **13** (5): 529-539.
- Chen, C., Raghavan, R., 1997. A Multiply-Fractured Horizontal Well in a Rectengular Drainage Region. *SPEJ* **2** (4): 455-465. SPE 37072-PA.
- Chang, J. and Yortsos, Y., 1990. Pressure Transient Analysis of Fractal Reservoirs. *SPE Formation Evaluation* **5** (1). SPE 18170-PA.
- Cinco-Ley, H., Meng, H.Z., 1988. Pressure Transient Analysis of Wells with Finite Conductivity Vertical Fractures in Double Porosity Reservoirs. Paper SPE 18172 presented at SPE Annual Technical Conference and Exhibition, 2-5 October, Houston, TX, USA.
- Clay Membrane Barriers, Retrieved September 2013, from http://claymembranebarriers.org/backgroundFrameset.html

- Cossio, M., Moridis, G.J., Blasingame, T.A., 2013. A Semi-Analytic Solution for Flow in Finite-Conductivity Vertical Fractures Using Fractal Theory. *SPE Journal*, **18** (1):83-96.
- Culberson, O.L., McKetta, Jr, J.J., 1950. Phase Equilibria in Hydrocarbon-Water Systems II-The Solubility of Ethane in Water at Pressures to 10,000 psi. *Journal of Petroleum Technology*, **2**(11), 319-322.
- Dodson, C.R., Standing, M.B., 1944. Drilling and Production Practice. API, 1944.
- Firincioglu, T., Ozkan, E., and Ozgen, C., 2012. Thermodynamics of Multiphase Flow in Unconventional Liquids-Rich Reservoirs. Paper SPE 159869 presented at the SPE Annual Technical Conference and Exhibition, 8-10 October, San Antonio, Texas, USA.
- Firincioglu, T., Ozgen, C., Ozkan, E., 2013. An Excess-Bubble-Point-Suppression Correlation for Black Oil Simulation of Nano-Porous Unconventional Oil Reservoirs. Paper SPE 166459 presented at the SPE Annual Technical Conference and Exhibition, 30 September-2 October 2013, New Orleans, Louisiana, USA.
- Firincioglu, T., 2013. Bubble Point Suppression in Unconventional Liquids Rich Reservoirs and Its Impact on Oil Production. PhD Dissertation. Colorado School of Mines, Petroleum Engineering Department, Golden, Colorado, USA.
- Flamenco-Lopez, F. and Camacho-Velazquez, R., 2003. Determination of Fractal Parameters of Fracture Networks Using Pressure Transient Data. *SPE Reservoir Evaluation & Engineering* **6** (1). SPE 82607-PA.
- Fomin, S., Chugunov, V. and Hashida, T., 2011. Mathematical modeling of Anomalous Diffusion in Porous Media, *Fractional Differential Calculus*, **1**, 1-28.
- Fuentes-Cruz, G., Camacho-Velázquez, R. and Vásquez-cruz, M., 2010. Unified Approach for Falloff and Buildup Tests Analysis Following a Short Injection / Production Time. SPE 133539-MS presented at the SPE Western Regional Meeting, 27-29 May, Anaheim, California, USA.
- Geren, F., Firincioglu, T., Karacaer, C., Ozkan, E., 2014. Modeling Flow in Nanoporous, Membrane Reservoirs and Interpretation of Coupled Fluxes. Paper SPE 170976 presented at the SPE Annual Technical Conference and Exhibition, 27-29 October, Amsterdam, The Netherlands.
- Geren, F., 2014. Modeling Flow in Nanoporous, Membrane Reservoirs and Interpretation of Coupled Fluxes. MSc Thesis. Colorado School of Mines, Petroleum Engineering Department, Golden, Colorado, USA.
- Giona, M., Roman, H.E., 1992. Fractional Diffusion Equation for Transport Phenomena in Random Media. *Physica A*, **185** (1-4): 87-97.

- Greenwood, J., 2015. An Analytical Investigation of Boundaries in Naturally Fractured Unconventional Reservoirs. MSc Thesis. Colorado School of Mines, Petroleum Engineering Department, Golden, Colorado, USA.
- Hassanzadeh, H., Pooladi-Darvish, M., Elsharkawy, A.M., Keith, D.W., Leonenko, Y., 2008. Predicting PVT Data for CO₂-Brine Mixtures for Black-Oil Simulation of CO₂ Geological Storage. *International Journal of Greenhouse Gas Control*, **2**(1), 65-77.
- Hewett, T. A., 1986. Fractal Distributions of Reservoir Heterogeneity and Their Influence on Fluid Transport. Paper SPE 15386 presented at the SPE Annual Technical Conference and Exhibition, 5 8 October, New Orleans, Louisiana, USA.
- Kazemi, H., 1969. Pressure Transient Analysis of Naturally Fractured Reservoir with Uniform Fracture Distribution. *SPE J.* **9** (4):451-462. SPE-2156-PA.
- Lasater, J. A., 1958. Bubble point pressure correlation. *Journal of Petroleum Technology*, **10**(5), 65-67.
- Liu, F., Anh V., Turner, I., 2004. Numerical solution of the space fractional Fokker-Planck equation. *Journal of Computational and Applied Mathematics*, 166, 209-219.
- Metzler, R. Glockle, W.G., Nonnenmacher, T.F., 1994. Fractional Model Equation for Anomalous Diffusion. *Physica A*, **211** (1994): 13-24.
- Murio, D.A., 2008. Implicit finite difference approximation for time fractional diffusion equations. *Computers and Mathematics with Applications*, 56, 1138-1145.
- Nelson, P.H., 2009. Pore-throat Sizes in Sandstones, Tight Sandstones, and Shales. *The American Association of Petroleum Geologists*, V. 93, No.3 pp. 329-340.
- O'Shaughnessy, B. and Procaccia, I., 1985. Diffusion on Fractal, *Phys. Rev. A* **32** (5): 3073-3083.
- O'Shaughnessy, B. and Procaccia, I., 1985. Analytical Solutions for diffusion on Fractal Objects. *Physical Review Letters*, **54**(5): 455-458.
- Ozcan, O., Sarak, H., Ozkan, E., Raghavan, R., 2014. A Trilinear Flow Model for a Fractured Horizontal Well in a Fractal Unconventional Reservoir. Paper SPE 170971 presented at the SPE Annual Technical Conference and Exhibition, 27-29 October, Amsterdam, The Netherlands.
- Ozcan, O., 2014. Fractional Diffusion in Naturally Fractured Unconventional Reservoirs. MSc Thesis. Colorado School of Mines, Petroleum Engineering Department, Golden, Colorado, USA.
- Ozkan, E., Brown, M., Raghavan, R., and Kazemi, H. 2011. Comparison of Fractured-Horizontal-Well Performance in Tight Sand and Shale Reservoirs. *SPEREE* **14** (2): 248-259.

- Ozkan, E., Brown, M., Raghavan, R. and Kazemi, H. 2009. Comparison of Fractured Horizontal-Well Performance in Conventional and Unconventional Reservoirs. Paper SPE 121290 presented at the SPE Western Regional Meeting, 24 26 March, San Jose, California, USA.
- Ozkan, E. 2011. On Non-Darcy Flow in Porous Media: Modeling Gas Slippage in Nanopores. SIAM Mathematical & Computational Issues in the Geosciences Meeting, 21-24 March, Long Beach, California, USA.
- Ozkan, E. 2013. A Discourse on Unconventional Reservoir Engineering The State of the Art after a Decade. Technical Report, Unconventional Reservoir Engineering Project Consortium Meeting at Colorado School of Mines, 8 11 November, Golden, Colorado, USA.
- Peng, D.Y., Robinson, D.B., 1976. A New Two-Constant Equation of State. *Industrial and Engineering Chemical Fundamentals*, **15** (1): 59-64.
- Raghavan, R., 2011. Fractional derivatives: Application to transient flow, *Journal of Petroleum Science and Engineering*, 80, 7-13.
- Raghavan, R. and Chen, C., 2013a. Fractional diffusion in rocks produced by horizontal wells with multiple, transverse hydraulic fractures of finite conductivity, *Journal of Petroleum Science and Engineering*, 109, 133-143.
- Raghavan, R. and Chen, C., 2013b. Fractured-Well Performance under Anomalous Diffusion, *SPE Res Eval & Eng*, **16** (3), 237-245.
- Reid, R.C., Prausnitz, J.M., Polling, B.E., 1987. *The Properties of Gases and Liquids*. New York, USA, McGraw-Hill.
- Schneider, W. R. and Wyss, W. 1989. Fractional diffusion and wave equations. *J. Math. Phys.* **30** (1): 134 144.
- Shapiro, A.A., and Stenby, E.H., 2001. Thermodynamics of the Multicomponent Vapor-Liquid Equilibrium under Capillary Pressure Difference. *Fluid Phase Equilibria*, **17** (32): 178.
- Stehfest, H., 1970. Algorithm 368: Numerical inversion of Laplace transforms [D5], Communications of the ACM, **13** (1) 47 49.
- Stone, H.L., 1973. Estimation of Three-Phase Relative Permeability and Residual Oil Data. *Journal of Canadian Petroleum Technology*, **2** (4), 53-61.
- Todd, M.R., Longstaff, W.J., 1972. The Development, Testing, and Application of a Numerical Simulator for Predicting Miscible Flood Performance. *Journal of Petroleum Technology*, **24**(7), 874-882.

- Udell Kent S., 1982. The Thermodynamics of Evaporation and Condensation in Porous Media. Paper SPE 10779 presented at the SPE California Regional Meeting, March 24-26, San Francisco, California, USA.
- Vazquez, M., Beggs, H. D., 1980. Correlations for Fluid Physical Property Prediction. *Journal of Petroleum Technology*, **32**(6), 968-970.
- Wang, L., Parsa, E., Gao, Y., Ok, J. T., Neeves K., Yin X., Ozkan E., 2014. Experimental Study and Modeling of the Effect of Nanoconfinement on Hydrocarbon Phase Behavior in Unconventional Reservoirs. Paper SPE 169581 presented at SPE Western North American and Rocky Mountain Joint Meeting, 17-18 April, Denver, Colorado, USA.
- Wang, L., Neeves, K., Yin, X., Ozkan, E., 2014. Experimental Study and Modeling of the Effect of Pore Size Distribution on Hydrocarbon Phase Behavior in Nanopores. Paper SPE 170894 presented at the SPE Annual Technical Conference and Exhibition, 27-29 October, Amsterdam, The Netherlands.
- Wang, L., Gao, Y., Neeves, K., Ozkan, E., Yin, X., 2014. Experimental Study and Modeling of the Effect of Pore Size Distribution on Hydrocarbon Phase Behavior in Nanopores. Paper SPE 170894 presented at the SPE Annual Technical Conference and Exhibition, 27-29 October, Amsterdam, The Netherlands.
- Warren, J.E., Root, P.J., 1963. The Behavior of Naturally Fractured Reservoirs. *SPEJ*, **3**(3), 245-255. SPE 426-PA.
- Weinaug, C.F., Katz, D.L., 1943. Surface Tension of Methane-Propane Mixtures, *Industrial* and Engineering Chemistry, **239** (46): 35.
- Yeung, A.T., Mitchell, J.K., 1993. Coupled Fluid, Electrical and Chemical Flows in Soil. *Geotechnique*, 43, 1, 121-134.
- Zarragoicoechea, G. J., Kuz, V. A., 2004. Critical Shift of a Confined Fluid in a Nanopore, *Fluid Phase Equilibria*, **7** (9): 220.